DESIGN AND APPLICATION OF TERAHERTZ METAMATERIAL ABSORBER

Thesis Submitted for the Award of the Degree of

DOCTOR OF PHILOSOPHY

in

ELECTRONICS AND COMMUNICATION ENGINEERING

By

LAXMINARAYANA DEEKONDA
Registration Number: 41900683

Supervised By

Dr. Sanjay Kumar Sahu (23393)
Electronics and Communication Engineering
(Professor)
Lovely Professional University

Co-Supervised by

Dr. Asit Kumar Panda
Electronics and Communication Engineering
(Associate Professor)
National Institute of Science and Technology

LOVELY PROFESSIONAL UNIVERSITY, PUNJAB
2024

DECLARATION

I, hereby declared that the presented work in the thesis entitled **"Design and Applications of Terahertz Metamaterial Absorber"** in fulfilment of degree of **Doctor of Philosophy (Ph. D.)** is outcome of research work carried out by me under the supervision of Dr. Sanjay Kumar Sahu, working as Professor, in the School of Electronics & Elctrical Engineering of Lovely Professional University, Punjab, India. In keeping with general practice of reporting scientific observations, due acknowledgements have been made whenever work described here has been based on findings of other investigator. This work has not been submitted in part or full to any other University or Institute for the award of any degree.

(Signature of Scholar)

Laxminarayana Deekonda

41900683

School of Electronics & Electrical Engineering

Lovely Professional University,

Punjab, India

CERTIFICATE

This is to certify that the work reported in the Ph. D. thesis entitled "Design and Applications of Terahertz Metamaterial Absorber" submitted in fulfillment of the requirement for the award of degree of Doctor of Philosophy (Ph.D.) in the School of Electronics & Communication Engineering, is a research work carried out by Laxminarayana Deekonda, 41900683, is bonafide record of his/her original work carried out under my supervision and that no part of thesis has been submitted for any other degree, diploma or equivalent course.

Supervisor Signature
Dr. Sanjay Kumar Sahu
Professor
School of Electronics & Electrical Engineering
Lovely Professional University
Punjab, India

Co-Supervisor Signature
Dr. Asit Kumar Panda
Associate Professor
NIST
National Institute of Science & Technology
Ganjam, Odisha, India

ACKNOWLEDGEMENTS

First of all, I am grateful to The Almighty God for His shower of blessings throughout my research work to complete the research successfully.

I am deeply grateful to my supervisor, **Prof. Sanjay Kumar Sahu** and co-supervisor, **Dr. Asit Kumar Panda** for their meaningful assistance, continuous support, and guidance throughout this journey.

My heartiest and sincere gratitude to **Dr. Sheleja Khera**, Head, Department of Electronics and Communication Engineering, Lovely professional University, Punjab, for providing me all possible facilities for carrying out the research work in the department.

Most important, I would like to express my appreciation to my **Parents, Wife, Sisters** and other members of the **Family** for their unconditional love, support, and constant encouragement.

Laxminarayana Deekonda

Abstract

Metamaterials are materials produced artificially and have properties that do not exist in naturally occurring compounds. The fundamental components of these materials are arranged in preset patterns at sizes lower than the wavelength of the phenomenon they interact with. Therefore, they can creatively manipulate sound, electromagnetic, and other types of waves. It has some distinctive qualities, including a negative refractive index, the Doppler effect, cloaking, sensing, imaging, perfect absorber, etc. Blackbody MMs, referred to as perfect-absorption (PA) MMs or MM-based perfect absorbers (MM-PAs), have rapidly evolved in plasmonic sensors, bolometers, wireless power transfer, and perfect light absorbers. These are notable for their capacity to increase the efficiency of absorbing solar energy. Despite dielectric and ohmic losses and the resonance between the inductive and capacitive components, energy can be trapped in the circuit and subsequently released. The dielectric's absorption significantly outweighs the conductor's Ohmic loss. Consequently, a significant portion of the dielectric loss has been produced by magnetic resonance, which results in antiparallel currents.

MM absorbers were initially proposed by Landy et al. and had the advantage of being smaller and thinner in dimension than the conventional absorbers. Landy et al. have proposed multiband, broadband, polarization-insensitive, and controllable band-optimized MM

absorbers for various applications, including thermal imaging, solar cells, sensing, etc. MM absorber was experimentally and theoretically confirmed in the GHz range. Due to some complexity, fabrication issues, more significant size, and thermal stability for design methods used for limited biosensor applications operating at THz frequency. MM absorber operating in THz is applicable, especially for biosensing applications, where it has several advantages like material differentiation, non-ionizing radiation, penetration and imaging, security screening, gas sensing, cultural heritage conservation, communication and data transfer, quality control and manufacturing, and scientific research.

Graphene material has received much attention in many scientific and engineering sectors, including metamaterials because it is adaptable and distinctive. Its specific qualities make it an appealing option for incorporation into metamaterial absorbers. Some of these are: **i)Broadband absorption:** Broadband absorption is possible thanks to the wide frequency tuning range of graphene's conductivity. Graphene-based metamaterial absorbers are suited for applications that demand broad spectral coverage because this is essential for attaining effective absorption over a range of frequencies. **ii) Tunability:** By changing external factors like chemical doping, electrical bias, or optical light, one can modify the conductivity of graphene. The metamaterial absorber's absorption qualities may be accurately controlled because of this tunability, making it adaptable to various operating circumstances. **iii) Thin and lightweight:** A single layer of carbon atoms organized in a hexagonal lattice makes up the two-dimensional substance known as graphene. It is appro-

priate for situations where weight and space restrictions are critical because of how thin and light it is. **iv) Integration with other materials:** Graphene can be combined with other substances, such as metals or dielectrics, to form hybrid structures with improved electromagnetic properties. **v) High Carrier Mobility:** The ability of charge carriers (such as electrons or holes) to flow through a material is known as carrier mobility, and graphene possesses an extraordinarily high carrier mobility. This characteristic may aid in effectively transferring charges inside the absorber structure. **vi) Compatibility with Flexible and Transparent Substrates:** Graphene is appropriate for applications that need conformal and transparent absorbers because it can be deposited onto flexible and transparent substrates. Graphene is costlier and can be used especially for single-layer graphene and fabrication complexity for graphene controllable and environmental stability maintained constantly by surrounding areas.

Chapter 2 reviews existing works that have already been reported on metamaterial absorbers operating at THz frequencies. Several metamaterial structures have been designed to date, but it has some design limitations, such as complexity, resonance overlapping, better Q-factor, high FoM, sound sensitivity, and better bandwidth. Hence, designing a broadband metamaterial with graphene works as a metamaterial absorber.

The third chapter presents a broadband terahertz (THz) metamaterial absorber. In this, the unit cell structure of this absorber consists of three layers. The top layer of the structure contains a circular graphene ring. At the center frequency of 2.0 THz, this circular

graphene ring has a fractional bandwidth of 67% and absorptivity of more than 90%. The proposed absorber is polarization insensitive because of its fourfold symmetrical structure. The graphene parameter is optimized to get maximum bandwidth. This metamaterial offers TE and TM polarization insensitivity up to a 600 incident angle of electromagnetic wave.

The fourth chapter includes two different metamaterial structures for various application bands. In design1, the metamaterial structure comprises three layers, with the top and bottom being Gold and separated by a dielectric material in between. The structure provides 100% at a lower frequency of 0.846 THz and 98.6% at a higher frequency of 2.12 THz. The Complementary Split Ring Resonators (CSRR) parameter is optimized for dual resonance frequency. The proposed CSRR shows a tuning range from 2.12 - 2.16THz. The proposed structure provides a quality factor of 19.2 at a lower-band frequency and 19.56 at an upper-band frequency. In design 2, a triband metamaterial was also implemented using a graphene-based metamaterial absorber for sensing applications. The implemented metamaterial structure offers the maximum absorption efficiency of 100%, 96%, and 70% at three different operating bands. The simulated performance shows that the presented design offered better outcomes than the earlier one.

The fifth chapter implements a multimode terahertz absorber using an ultrathin silicon ring with varying multimodal resonance. The rectangular silicon ring provides three resonances to create electromagnetic dipoles. The altering of these resonances is explicitly controlled with the help of a circular graphene ring. The graphene ring is used in

the center for tenability and perfect absorption. An equivalent circuit model is also presented and verified for the proposed structure. The design is intended to measure the glucose percentage in water. In addition, this can be used as a biosensor for detecting malaria parasite percentage in water. A few critical parameters, like sensitivity and quality factors, are considered to evaluate the performance of the said design. The sensitivity with analyte thickness is found to be 0.445 THz TU^{-1}, 0.4255 THz TU^{-1}, and 0.4305 THz TU^{-1}. The corresponding quality factor is noted for the lower, middle, and upper bands as 235, 653, and 264, respectively. Further, the sensitivity and quality factors were measured by changing the refractive index. The new estimated values are 0.480 THz RIU^{-1}, 0.403 THz RIU^{-1}, and 0.562 THz RIU^{-1}, and corresponding quality factors are 203, 555, and 261 for lower, middle, and upper bands, respectively. The design is also expected to flourish as a polarization-insensitive absorber.

In chapter 6, it generates Multi-band resonance for biosensing applications.A silicon hexagonal ring to provide a pentaband of resonance and their properties is introduced using a hexagonal graphene ring in the center. The absorber performance parameter is verified using an equivalent circuit model. The proposed design has a resonance at 4.78 THz, 5.1 THz, 5.4 THz, 5.76 THz, and 5.88 THz and improves the absorptivity level by more than 0.97 for all five bands.Another important feature of the proposed absorber is polarization insensitive.

Keywords: Metamaterial absorber, FoM, Sensitivity, Q-factor, Bandwidth, Ultrathin, Graphene, SRR, CSRR, Tuning.

Contents

List of Figures

List of Tables

List of Acronyms

2DEG	Two dimensional gas
aDSR	Asymmetric double split ring resonator
Au	Gold material
CSRR	Complementary split ring Resonators
CVD	Chemical vapor deposition
CW	Cut-wire
DNA	Deoxyribonucleic acid
DNG	Double negative material
DPS	Double positive material
DSRR	Double split ring resonator
EM	Electromagnetic waves
EMA	Effective medium approximations
EMF	Electromotive force
ENG	Epsilon negative material
FEM	Finite Element method
FWHM	width Half maximum
FoM	Figure of Merit
eSRR	electric Split Ring Resonator
FSS	Frequency selective surface
GaAs	Gallium arsenide
GHz	Gigahertz

IR	Infrared rays
ITO	Indium tin oxide
LB& UB	Lower band and Upper band
LHM	Left handed material
MA	Metamaterial absorber
MDM	Metal-dielectric metal
MDM	Metal-microstructure array dielectric-metal
MHA	Metal hole arrays
MM	Metamaterial
MMD	Multilayered metamaterial devices
MMPA	Metamaterial Perfect absorber
MNG	Mu negative material
MPA	Metamaterial Perfect absorber
NIM	Negative index material
NMPM	Negative magnetic permeability
OLED	Organic light-emitting diodes
PA	Perfect absorber
PEC	Perfect electric conductor
Q-factor	Quality factor
RIU	Refractive index unit
SDM	Split Disk Metamaterials
Si	silicon
SiC	Silicon carbide
SiO2	silicon dioxide
SPP	Surface Plasmon polaritons
SRR	Split Ring Resonator
ss-DNA	single-standed DNA

TCH	Tetracycline hydrochloride
TE	Transverse Electric field
THz	Terahertz
TLM	Transmission line method
TM	Transverse Magnetic field
TW	Thin wire

1

Introduction

Contents

Metamaterials, which are engineered substances, find extensive utility across various fields, including optical filters, medical equipment, aerospace technology, sensor technology, and infrastructure monitoring. This field combines knowledge from disciplines including engineering, electromagnetic theory, solid-state physics, optics, microwave engineering, optoelectronics, and materials science. Metamaterials can be traced back to the work of Dr. Jagadish Chandra Bose of India pioneered early structures with chiral properties that laid the groundwork for metamaterial research.

Metamaterials possess properties such as the ability to exhibit a refractive index. It means that electromagnetic signals can propagate in a manner through these materials. A significant milestone in this field was achieved by Victor Veselago in 1967 when he demonstrated that materials with indices allow for the transmission of light. These materials behave when electromagnetic waves interact with elements more petite than their wavelength. These elements are known as metamaterials. It must be extensively lesser than the wavelength to accurately exhibit properties similar to those of a homogenous material quantified by an effective refractive index. Electromagnetic metamaterials can be categorized into four types based on their properties. The first type is characterized by wave propagation with positive electric and magnetic fields. The second type is called negative, with an electric and positive magnetic field. The third type is negative, with both the electric and magnetic fields being negative resulting in a region with a refractive index. Lastly, there is another type called negative: the magnetic and electric fields are negative. This classification emphasizes how metamaterials can exhibit behaviour when interacting with waves.

A negative-index material, or negative-index metamaterial (NIM), exhibits a negative refractive index within a specific frequency range for electromagnetic waves. The electric field (permittivity) and the magnetic field (permeability) exhibit negative values in these materials. Negative index metamaterials are also

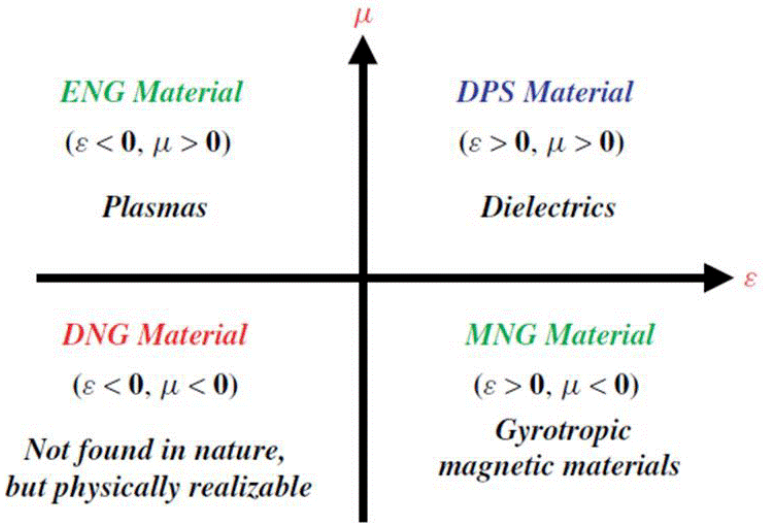

Figure 1.1: Types of metamaterial

referred to as "left-handed media," "backward-wave media," and media with a "negative refractive index". The concept of a negative refractive index is sometimes termed a "double negative metamaterial."

Let us consider a scenario where a material possesses absolute permittivity and permeability. The relationship between the refractive index (n), permeability (μ_r), and permittivity (ϵ_r) is given by the equation $= \pm\sqrt{\epsilon_r \mu_r}$. Transparent materials (glass, water, etc.) belong to non-metamaterials and they have positive (ϵ_r) and (μ_r). Some artificial materials have (ϵ_r) (μ_r) < 0. When the product is (ϵ_r) (μ_r) positive, then n is real. Under such conditions, taking the negative root of the square for n is required. If both (ϵ_r) and (μ_r) are positive, then it is called forward direction, and if both are negative, then it is called backward direction. As the refractive index becomes imaginary, the electromagnetic wave cannot propagate in the opposite sign of (ϵ_r) (μ_r). Examples of such materials, opaque to electromagnetic radiation, include plasmonic materials like metals (gold, silver).

Today, In the current era, we inhabit an information-driven world where the exchange of information between individuals is essential. Technological advance-

ments cater to human needs by offering practical applications. Metamaterials play a significant role in achieving these practical applications by leveraging various technologies. The concept of metamaterials (MM) traces back to observations by Dr. J.C. Bose in 2001, later formalized by Walser [1–4]. Walser's definition aligns with the one provided by the Defense Advanced Research Projects Agency (DARPA) in the USA, defining metamaterial as artificial materials with properties not found in nature, often exhibiting negative characteristics. The term "meta" originates from Greek, meaning "beyond" or "after," while "material" is rooted in Latin, signifying substance. In the past, engineered materials known as MMs showcased unconventional electromagnetic traits, such as negative refractive index [5], reverse Doppler effects [6], superlens capabilities [7], and electromagnetic wave cloaking [8]. These MMs have made remarkable strides in research. As nanotechnology evolved, MMs exhibited intriguing effects across a wide spectrum of electromagnetic waves and found application in microwave and photonic devices through sophisticated methodologies [9–12].

Metamaterials function as efficient absorbers [13], enhancing the efficiency of solar energy capture [14] and being applied in various domains like plasmonic sensing [15], bolometry [16], wireless power transfer [17], and the development of perfect light absorbers. MM absorbers demonstrate substantial loss [18–20], achieving resonance between the inductive and capacitive components of the circuit. This allows for energy storage and dissipation through Ohmic and dielectric losses. Notably, dielectric absorption significantly surpasses Ohmic loss in conductors. Consequently, magnetic resonance inducing antiparallel currents results in considerable dielectric loss [21].

Landy et al. introduced the concept of MM absorbers, which has revolutionized the field, offering a distinct advantage due to their compact and slender design compared to traditional counterparts [22–24]. Subsequent research has showcased the versatility of MM absorbers across applications, including thermal

imaging [24, 25], solar cells [26], and sensors [15]. Optimization pursuits have spanned a wide spectrum, from achieving multiband functionality [27–32] to accommodating broader frequency bands [18,33], polarization insensitivity [31–35], and controlled frequency responses.

However, pursuing ideal absorption conditions remains a delicate challenge, particularly when integrating multiband MMPAs with high efficiency. This challenge is underscored by the need to manage varying bandwidths tailored for specific applications, focusing on absorption peaks that become pivotal as frequencies transition from microwave to infrared ranges.

Metamaterials are harnessed as powerful tools for crafting optical components. MM's allure lies in its adaptability–its customizable size and shape allow for tailored designs catering to specific applications while also enabling the incorporation of optical attributes rarely found in traditional materials, such as heightened high-frequency magnetic responses.

Materials with negative refractive index, with negative values for both permittivity and permeability, have long captivated academic curiosity. Although this concept was explored in the 1960s, practical realization emerged in the early 21^{st} century. With rapid developments and computational advancements, metamaterials have become swifter, more reliable, and cost-effective tools for engineering devices endowed with extraordinary electromagnetic characteristics. Terahertz frequencies possess wavelengths shorter than microwaves, enabling the construction of more compact metamaterial structures. This compactness is essential for achieving desired electromagnetic properties at subwavelength scales. The range between microwaves and infrared light, termed terahertz frequencies, offers unexplored potential for imaging, sensing, and communication applications. Utilizing terahertz frequencies in metamaterials grants researchers access to this underexplored domain. Terahertz frequencies exert distinct effects on materials compared to microwaves, revealing unusual and unique responses in materials that are typ-

ically transparent or inert at microwave frequencies. Metamaterials operating at terahertz frequencies provide a novel and intriguing means to experiment and control electromagnetic traits of materials. These metamaterials offer finer control over electromagnetic fields compared to their microwave counterparts. The shorter wavelengths of terahertz waves enable the manipulation of subwavelength properties, resulting in enhanced resolution and precision for imaging and sensing applications. It is important to note that the choice of frequency depends on the specific application and desired electromagnetic characteristics. While microwave frequencies remain prevalent in many metamaterial applications, terahertz frequencies offer distinct advantages, particularly in antenna design and radar systems.

Terahertz waves, spanning from 0.1 to 10 THz, find applications across various industries, including medical imaging, broadband communications, radar, astronomy and nondestructive testing [36]. Compared to higher frequencies such as the visible or infrared areas, terahertz frequencies notably show less loss. Metals often act as ideal conductors, while low-loss dielectric materials lead to minimal attenuation of metamaterial resonance. This expands the optical constant values achievable with metamaterials, broadening design possibilities for optical systems and making terahertz frequencies a preferred choice for many applications. Metamaterials are widely employed in diverse research fields, particularly in antennas, where they serve as perfect absorbers. MM absorption is modulated based on EM wave resonance frequency. Manipulating MM polarization alters absorption levels through embedded diode lids [37]. Adjustable dual-band perfect absorbers have been developed by manipulating coupling component distances, leveraging exceptional optical transmission and Fabry-Pérot cavity resonance [38]. Metamaterial-designed micromachined actuators exhibit effective absorption at dual-band terahertz frequencies. The prospect of controllable absorbers holds promise for widespread applications in tunable filters, detectors,

and optical switches, capitalizing on their advantages [15, 16].

1.1 Theoretical Backgrounds

The classification of electromagnetic wave absorbers can generally be divided into two primary categories: resonant and broadband. Broadband absorbers can be further classified into two subcategories: low-density absorbers and geometric transition absorbers. Two-dimensional arrays of periodic featuring cones, lossy foam pyramids, or wedges are employed in creating geometric transition absorbers. These structures find applications in environments like anechoic rooms, where their purpose is to reduce wall reflections. On the other hand, low-density absorbers employ materials with poor or low-quality characteristics to achieve absorption.

It is important to note that these categorization schemes were formulated before integrating metamaterials into the realm of perfect absorbers (PA). Currently, non-resonant approaches are commonly employed to achieve broadband absorption. However, it is worth mentioning that resonant absorbers have the potential to achieve complete absorption within a narrow bandwidth, offering distinct advantages in specific applications.

1.2 Basic Design of Metamaterial perfect absorber

The concept of electromagnetic wave absorption began with the Frequency Selective Surface (FSS), initially introduced by American Engineer W. Salisbury in 1952, also known as the Salisbury Screen [39]. The Salisbury screen principle functions akin to an anti-reflection coating. It comprises of three types: i) a slim reflecting panel, ii) a less-loss dielectric base having a width equal to one-fourth of the incoming electromagnetic wave's wavelength, then iii) a seamless metallic

superficial. Due to precise 180° phase difference resulting from the reflection of waves off the narrow reflective shade and the seamless metal superficial caused by the quarter-wave-length chunkiness of the substrate, destructive interference occurs, leading to no reflection. This is the principle behind anti-reflection coatings. However, the Salisbury screen possesses two significant limitations: chunkiness and band of absorption. Due to limited absorption bandwidth, the dielectric layer's quarter-wavelength thickness only achieves complete destructive interference, making it unsuitable for practical applications.

Metamaterial Perfect Absorbers (MMPAs) typically consists of triple films: i) a film with sporadically ordered patterns of metallic, ii) a dielectric film, and iii) a seamless metalfilm. This structure is reminiscent of the Salisbury screen but with improvements. The metallic pattern layer replaces the original reflective layer, and the dielectric layer's thickness can be ample slighter than the wavelength, exclusively in the GHz range. Achieving total absorption entails no transmission or reflection. The third layer impedes incident waves, causing them to reflect.

The dielectric layer's core function is to offer a space for incoming electromagnetic waves to be absorbed. While preoccupation can happen in the metallic area, the dielectric layer plays a more critical role due to its higher absorption efficiency and lower losses. Generally, the dielectric layer offers ample space for incident EM waves, and a high refractive index material can reduce its thickness. The relationship for the incoming EM wavepath can be represented as nd, where n and d indicate the refractive index and the travel extent. In contrast to the requirements for anti-reflection coatings and Salisbury screens, a thick material is not always necessary as long as specific conditions are met. Dielectric substances typically have a small imaginary part of the dielectric constant, which suffices for absorbing EM waves. In MMPAs, the imaginary part of the dielectric constant plays a vital part in absorption, with the dielectric layer's characteristics influencing the design outcome. In some scenarios, the MMPA functions

like a Fabry-Perot Cavity or a Salisbury screen, producing dual-band absorption when space is provided in the resonance cavity. All incident EM waves initially strike the top layer and should be transmitted. This layer shares similarities with the Salisbury screen, but the structure involves metallic patterns rather than simple screens. The pattern is designed for specific frequency regimes to ensure transmission, distinct from the destructive interference principle of the Salisbury screen.

Incorporating the Drude mode, one can estimate both the actual and unreal components of the dielectric constant, denoted as ε_1 and ε_2, which is given as

$$\varepsilon_1(\omega) = \varepsilon_{\text{inf}} - \frac{\omega_p^2\tau^2}{1+\omega_p^2\tau^2} \tag{1.1}$$

and

$$\varepsilon_1(\omega) = \omega\tau\frac{\omega_p^2\tau^2}{1+\omega_p^2\tau^2} \tag{1.2}$$

When considering the parameters τ, ω, ω_∞, and ω_p, which respectively represent the relaxation time, angular frequency of the incoming EM wave, the Drudeparameter and the plasma frequency, the approximation of Equation 1.2 is achieved when $\omega\tau \approx 1$."

$$\varepsilon_1(\omega) = \varepsilon_{\text{inf}} - \frac{\omega_p^2}{1+\omega_p^2} \tag{1.3}$$

The Drude parameter is often denoted as (∞), with ε_1 in this region satisfying the condition where $\omega\tau << 1$. It can be expressed as a function of either ω^{-2} or λ^2. When plotted as ε_1 versus λ^2 or ε_1 versus ω^{-2}, it forms a continuous line, and ε_∞ serves as the intercept at $\omega^{-2} = 0$ or $\lambda^2 = 0$. Notably, ε_∞ typically differs from unity, as it represents the real part of the dielectric constant measured at $\omega = \infty$," reflecting the polarization of core electrons. Metals generally exhibit a plasma frequency, often exceeding 5eV, leading to a negative absolute value of ε_1 in the infrared (IR) and visible spectral regions. To create metamaterials

(MMs) that function effectively in the GHz, THz, IR, and even visible regimes, it's crucial to reduce the "effective" plasma frequency. This reduction helps achieve the desired characteristics required for these specific frequency ranges, as plasma perturbations associated with the original plasma frequency can achieve these properties. This is because the plasma frequency is determined by the equation:

$$\omega_p = \sqrt{\frac{4\pi n e^2}{m^*}} \tag{1.4}$$

Here e denotes fundamental charge of an electron, the charge density is n and m^* is the mass that is effectively measured, metallic units "diluted," making it necessary. The term "diluted" implies a reduction in charge density within metamaterials (MMs), which in turn facilitates the plasmonic resonance to occur within the desired frequency range. Metamaterial design content array of patterned unit cells. The "effective" charge thickness can be suitably modified by selectively removing a portion of the metallic layer, thereby enabling the plasmonic resonance within the desired occurrence range.

In active mode, both the second and first layers are engaged. The Salisbury screen conveys the reproduced wave from a continuous metallic superficial, reflecting the incident EM wave back into the originating space. These two EM waves occasionally undergo destructive interference, leading to zero reflection. In contrast, while the first layer in the Salisbury screen assumes a passive part, the primary coating of MMPA gives an additional dynamic and active part. In the first layer, no reflection occurs because it should match the impendence of the first layer to free space impendence or atmosphere. There should be no difference between free space impendence and the first layer for impendence purposes. Complete impendence matching for incident waves assumes that the two mediums, the atmosphere and the first layer, are visually identical. Generally, materials are rigid to match free space impendence. Only MM's dimensions are

carefully adjusted, and properties can follow them. This type of impendence matches particular resonance or plasmonic couplings only. Therefore, despite being macroscopically inhomogeneous, MMs must be preserved as similar materials. Consequently, the utilization of the effective-medium approximation (EMA) becomes compulsory.

Another interesting aspect to consider is the potential misunderstanding of the imaginary part of the dielectric function in certain situations. Most people think a strong absorption must follow from the imaginary part's huge magnitude. This one statement is a rough approximation, while the other is more conservative. There are two distinct approaches to defining the optical constants of a medium, one involving the complex refractive index $n \equiv n + ik$, and the complex dielectric function $\tilde{\varepsilon} \equiv \varepsilon_1 + i\varepsilon_2$, wherever n denotes refractive index and k denotes extinction coefficient). The preoccupation, proper attenuation, and imaginary part to dielectric function of the incident EM wave were not determined directly rather to extinction coefficient factor is $e^{\frac{kr}{\delta}}$, wherever δ denotes skin depth. The relation among the complex refractive index and complex dielectric function, $\tilde{\varepsilon} = \tilde{n}^2 = (n + ik)^2$, holds. Consequently, the two subsequent associations can be easily derived.

$$\varepsilon_1 = Re[\tilde{\varepsilon}] = Re[(n + ik)^2] = n^2 - k^2 \tag{1.5}$$

and

$$\varepsilon_2 = \mathrm{Im}\,[\varepsilon] = \mathrm{Im}\left[(n + ik)^2\right] = 2nk \tag{1.6}$$

According to Equations 1.2 and 1.2, $-\varepsilon_1 << 1$ and $\varepsilon_2 >> 1$ when $\omega << \omega_p$. It implies that $n << 1, k << 1$, and, extra prominently, $n << k$ even for optical choice of occurrence. The incident EM waves exhibit significant attenuation, evident from the pronounced the absolute value for extinction coefficient factor within the optical frequency choice. However, strong attenuation does not always

equate to robust absorption; rather, it signifies a reduction in the skin depth corresponding to an increase in the extinction coefficient. Consequently, the incident EM wave's penetration into the metal is limited, with most absorption occurring near the extremely thin surface layer of metals. This means that in metals, when the metallic layer's thickness surpasses the skin depth significantly, absorption becomes negligible, and transmission is absent. In such scenarios, the majority of incoming EM waves within the region of Drude experience reflection, as maximum metals operate around plasma frequencies well beyond the range of visible light, they predominantly reflect visible light, explaining their characteristic shiny and smooth surfaces. The considerable value of the imaginary component of the dielectric function primarily leads to strong reflection rather than solid absorption. This underscores the importance of the patterned metallic layer. Although the imaginary component is usually smaller than the real part, its pronounced magnitude proves pivotal for perfect absorption, mainly when the primary absorption mechanism is dielectric. Sometimes, the central absorption mechanism can be Ohmic. In this scenario, while the substantial imaginary component is crucial for reducing the Q-factor, it is not necessarily vital for achieving perfect absorption. Reducing the Q-factor expands the absorption peak's bandwidth, which is crucial for achieving the broadband response of Metamaterial Perfect Absorbers (MMPAs).

1.3 Split Ring Resonator

A Metamaterial typical structure which is artificially generated is called the split-ring resonator (SRR). The primary objective is to induce the desired magnetic susceptibility, effectively creating a magnetic response within various metamaterials, extending up to 200 terahertz. These materials display a strong magnetic interaction with an applied electromagnetic field, a characteristic that is

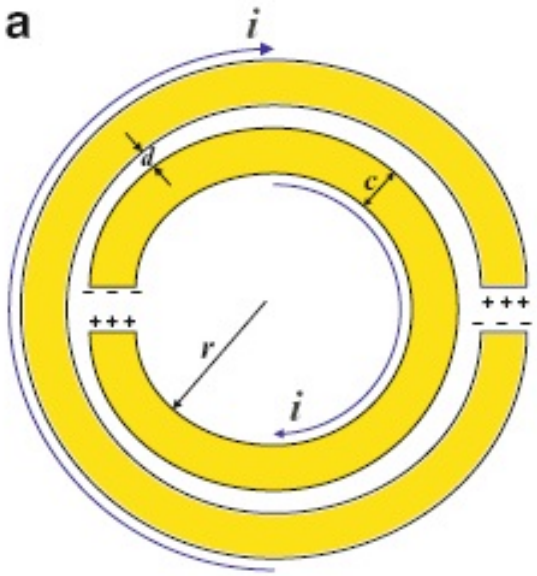

Figure 1.2: Split Ring Resonator

typically absent in traditional materials. For instance, when arranged in a periodic array, split ring resonators can emulate effects reminiscent of negative permeability. A solitary SRR unit consists of two enclosed loops with splits at opposing ends, separated by a small gap. These loops are usually crafted from non-magnetic metals such as copper, and the gaps between them can be either square or concentric. When a magnetic flux permeates through these metal rings, it engenders circulating currents that, contingent on the SRR's resonant properties, either reinforce or counteract the incident magnetic field. This engenders a dipolar field pattern. The narrow inter-ring gaps yield notably high capacitance values, leading to a reduction in the resonant frequency. Consequently, the structure's dimensions are relatively diminutive in comparison to the resonant wavelength, resulting in minimal radiative losses and exceptionally high-quality factors [40–42].

SRRs are structured with two concentric metallic rings etched into a dielectric substrate, each featuring slits on opposite sides. SRRs are notable for their

capacity to minimize electrical effects when exposed to oscillating electromagnetic fields. Their significance lies in their ability to facilitate the creation of materials exhibiting a left-handed and negative refractive index. This negative effective permeability is primarily achieved through the presence and characteristics of SRRs. When subjected to a time-varying magnetic field, an array of these electrically small SRRs effectively operates as a medium with negative effective permeability, albeit within a limited range centered around the SRR resonance frequency. Furthermore, SRRs have been successfully incorporated into planar transmission lines to craft metamaterial transmission systems. [43–45]. A microstructure termed as split ring resonator was described in the 1999 publication by Pendry et al. titled as "Magnetism from Conductors and Enhanced Nonlinear Phenomena" [46]. The suggestion put forth that utilizing a split ring resonator design crafted from non-magnetic materials could enhance magnetic characteristics not commonly found in natural materials.. In the straightforward microstructure design, it is demonstrated that the effective permeability may be expressed as follows, In an arrangement of conductive cylinders subjected to an externally applied magnetic field H_0 oriented parallel to the cylinders.

$$\mu_{\text{eff}} = 1 - \frac{\pi r^2}{a^2}\left(1 + i\frac{2\sigma}{\omega r \mu_0}\right)^{-1} \tag{1.7}$$

Here, σ represents the surface resistance of the cylinder per unit area, while a denotes the spacing between the cylinders. Additionally, ω stands for the angular frequency μ_0 and r are permeability and radius. Additionally, we observe that gaps create a capacitance in a double-cylinder design identical to the one in the illustration above. The microstructure of the capacitor and inductor generates a resonance that enhances the magnetic action. The novel effective permeability exhibits a response [47] that is well-known in plasmonic materials.

$$\mu_{\text{eff}} = 1 - \frac{\frac{\pi r^2}{a^2}}{1 + \frac{2\sigma i}{\omega r \mu_0} - \frac{3dc_0^2}{\pi^2 \omega^2 r^3}} \tag{1.8}$$

Where d for spacing concentric conducting sheets. A replacement for the double concentric cylinders in the final design consists of a pair of flat concentric c-shaped sheets on both sides of a unit cell. These unit cells are then stacked one on top of the other with a separation of length l.Below is an illustration of the effective permeability's end outcome.

$$\mu_{\text{eff}} = 1 - \frac{\frac{\pi r^2}{a^2}}{1 + \frac{2l\sigma_1 i}{\omega r \mu_0} - \frac{3lc_0^2}{\pi^2 \omega^2 r^3 \ln\left(\frac{2c}{d}\right)}} \tag{1.9}$$

1.4 Complementary Split Ring Resonator

Complementary Split Ring Resonators (CSRRs), a specialized form of metamaterial structure connected to the more famous Split Ring Resonator (SRR). CSRRs can display distinctive behavior in response to electromagnetic waves and are created to complement the electromagnetic characteristics of SRRs. The word "complementary" in CSRR refers to the electromagnetic response that CSRRs are made to exhibit, which is either the opposite of or complementary to that of SRRs. In other words, CSRRs are made to exhibit a positive magnetic response at the same frequencies, but SRRs typically exhibit a negative magnetic response (negative permeability). CSRRs are built using a different geometry than SRRs. CSRRs feature a complementary construction that comprises a solid ring or structure in place of the gap in the SRR, whereas SRRs are made up of one or more concentric rings with a gap or split. Due to this alteration, CSRRs can display complementary electromagnetic characteristics. Similar to SRRs, CSRRs are engineered to behave resonantly at particular frequencies. The resonant frequency depends on the shape and dimensions of the CSRR. CSRRs show a significant electromagnetic response when subjected to electromagnetic waves at or near the resonant frequency. There are numerous applications for CSRRs and related complementary structures in electromagnetic and microwave fields. Their com-

plementary behavior can produce metamaterials with particular characteristics, such as creating negative refraction, subwavelength imaging, and cloaking effects at particular frequencies. CSRRs and SRRs are frequently employed as fundamental components in Frequency Selective Surfaces (FSS). FSSs are surfaces that permit some frequencies of electromagnetic wave transmission or reflection while blocking others. Due to their complementary behavior, CSRR-based FSSs may have unique characteristics. CSRRs can be employed as sensors to identify changes in the electromagnetic environment similarly to SRRs, particularly at frequencies where they show resonant behavior.

1.5 Motivation

The goal of engineering materials with unusual and non-conventional properties not present in naturally occurring substances is the driving force behind the development and research of metamaterials. Because of its ability to alter , sound waves, electromagnetic waves and other forms of waves in ways that were previously considered to be impossible, metamaterials have concerned the courtesy of scholars and scientists from a variety of professions. The following are some significant causes for exploring metamaterials. Researchers can now design and make materials with characteristics that do not occur in nature through metamaterials. For instance, carefully built metamaterial structures can create materials with negative refraction, superlensing, and cloaking effects. Metamaterials give us a way to control and reuse electromagnetic radiation. Applications for this can be found in optics, telecommunications, radar technology, and imaging techniques.

Metamaterials offer novel chances to create sophisticated lenses, imaging devices, and sensors that function beyond the bounds of traditional materials. In order to potentially enable the development of stealth technology, the concept of a cloak in which metamaterials may bend light around objects has piqued at-

tention in various domains, including military and defense. Metamaterials can absorb and control energy from various sources, such as thermal emissions and solar radiation. Improved energy harvesting technologies may benefit from this. The exploration of fundamental physical processes using metamaterials pushes the limits of our knowledge of wave-matter interactions and electromagnetic behavior. Metamaterials are helpful in various fields, including materials research, healthcare, aerospace, and telecommunications. Nanophotonics and nanoelectronics have advanced because of metamaterials' ability to investigate and manipulate waves at sizes smaller than the wavelength itself. Metamaterials can improve the performance of antennas, sensors, and detectors by increasing their sensitivity, directionality, and selectivity. The difficulty of developing and understanding the behavior of these synthetic materials has prompted scientific inquiry.

This Ph.D. research work aims to design a metamaterial absorber with improved bandwidth and also to design a dual-band metamaterial absorber at THz for improving Q-factor and FoM and multi-band absorption generated using MM and triple band peaks are generated using MM absorber at THz for sensing application.

1.6 Problem Statements

With the strength of the motivations stated in section 1.5, the authors came up with some absolute problems associated with designing and developing Metamaterial absorbers at THz applications as part of this doctoral research. The dominant problems that have been attempted to solve are stated as follows:

(i) **Problem statement 1:** To design and develop a THz metamaterial absorber with enhanced efficiency above 65%.

(ii) **Problem statement 2:** To design and develop a THz metamaterial absorber with an improved Q-factor and FoM.

(iii) **Problem statement 3:** To design and develop THz Multi-band metamaterial for sensing applications.

(iv) **Problem statement 4:** To design and develop THz triple-band metamaterial for biosensing applications.

1.7 Thesis Organization

The thesis consists a total of six chapters and the contents of each chapter is as follows:

The first chapter discussed the difference between natural material and metamaterial, and it mentioned the history of MM, its properties and application, and how it can act as an absorber. Split ring Resonator, Complimentary method and motivation, problem statement, thesis organization.

The second chapter discusses metamaterial absorbers using different techniques and studies previous techniques about SRR and CSRR technique, dual-band absorbers, multi-band technique, sensing method, some structures used with wideband material, narrow band, ultra-wideband so based on these papers summarized and to achieve objects so finally concluded report in the existing literature survey.

The third chapter discussed bandwidth efficiency using graphene material for better tuning, conductivity, stability, and flexibility. The unit cell structure contains a circular graphene ring on the top layer, the middle layer is SiO2, and the bottom layer is gold. This circular graphene ring metamaterial provides a bandwidth of 67% and is polarization insensitive for TE and TM waves, both EM waves with an incident angle of up to 60^0.

The fourth chapter discussed a dual-band and Multi-band resonance for good absorption peaks, better Q-factor, and FoM values gained compared to previous literature. A dual-band operation was achieved by designing metamaterial

based on Rectangular Complementary Split Ring Resonators (CSRR). The utilization of gold metal in the CSRR design results in effective absorption. The structure, with two distinct band frequencies at 0.845 THz and 2.12 THz, was created using CST Microwave Studio. For Multi-band resonance designed with three different layers, one layer uses Au material for the bottom, the middle with silicon dioxide, and the top uses CSRR(Complimentary Split Ring Resonator). The outer side ring is used with Au material, and the inner side is used with Graphene material.

The fifth chapter discussed a triple-band absorber for tunable THz for biosensing, and it achieves good sensitivity and better Q-factor and FoM values, so we designed a rectangular ring structure used for resonance and on rotation it will provide triple resonance. Further, a circular graphene ring is used for tunning absorption peaks and providing good sensitivity. The performance of the proposed structure is verified for analyte thickness, refractive index, malaria disease, and glucose level in the water.

The sixth chapter describes how a hexagonal arrangement with a graphene ring produced five band peaks that can be utilised to construct biosensor applications using an ultra-thin multiband absorber. A ground plane consisting of gold is located at the base of the construction and serves as an effective reflector. The substrate is made of SiO_2, a dielectric material with good temperature stability and strong dielectric strength. A hexagonal ring that produces multi-band resonance and a graphene ring in the centre allow for better tuning.

2

Survey of Existing Methods

Contents

2.1 Introduction

Metamaterials are synthetic substances that do not occur naturally in the environment, designed in a periodic structure with sizes smaller than the incident electromagnetic waves. The behavior of incident waves is influenced by two factors: the material's permittivity (ε) and permeability (μ). Generally, these materials exhibit unique characteristics, with both ε and μ being negative in artificial materials, whereas natural materials have positive values. Metamaterials possess numerous extraordinary properties, including the inverse Doppler effect, negative refractive index, superlensing, electromagnetic wave cloaking, and applications in microwave and photonic devices. One remarkable effect is the perfect absorber metamaterial, also called as MM-Perfect absorber, originally conceptualized by Landy and colleagues, is a category of metamaterial with diverse applications spanning fields like thermal imaging, solar cell technology, sensors, and optimization, including multi-band and broadband applications.

Metamaterial perception was initially introduced by exploring magnetism, as discussed in reference [47]. This discussion highlighted the challenge of realizing the influential permeability phenomenon of non-conducting magnetic materials using naturally occurring materials.

2.2 History of Metamaterials

The field of metamaterials experienced a groundbreaking development in 1968 when V.G. Veselago introduced the theoretical potential to craft materials characterized by negative permittivity and negative permeability [48]. This concept laid the foundation for the development of metamaterials.

In 1999, John Pendry further advanced the field by introducing the idea of left-handed metamaterials, which deviated from the established principles governing right-handed metamaterials [49]. He presented a concept for a Thin-wire (TW)

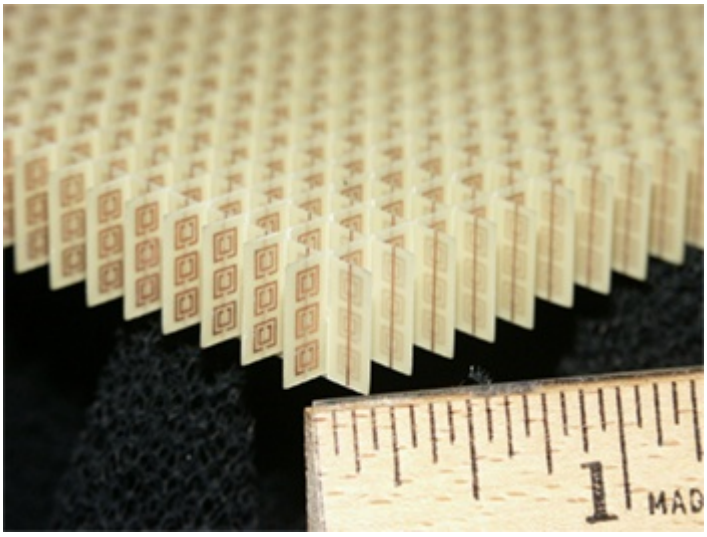

Figure 2.1: Metamaterial structure [49].

structure that could be arranged periodically and exhibit a negative value of effective permittivity [49]. Experimental demonstrations in the microwave regime demonstrated that the structure possessed a plasma frequency lower than that of the incoming wave. This discovery opened up new possibilities for controlling electromagnetic waves using metamaterials. This structure can effectively exhibit low plasma frequency results in negative permittivity at microwave frequencies, and it achieves negative permeability by utilizing Split Ring Resonators (SRR) [50] Fig. 2.1. Smiths groundbreaking work led to the suggesting left-handed metamaterials capable of demonstrating negative values for both permittivity and permeability in microwave experiments, showcasing their unique and uncommon properties [51].

In a pioneering experiment, Shelby et al. demonstrated negative refraction by utilizing metamaterials consisting of repetitive unit cells composed of split ring resonators (SRR) and copper strips [52, 53]. This marked the first time observation of negative refraction with metamaterials.

Later, Wu et al. introduced three structures: symmetrical ring, Omega, and S structures for SRRs [54]. These developments expanded the possibilities for

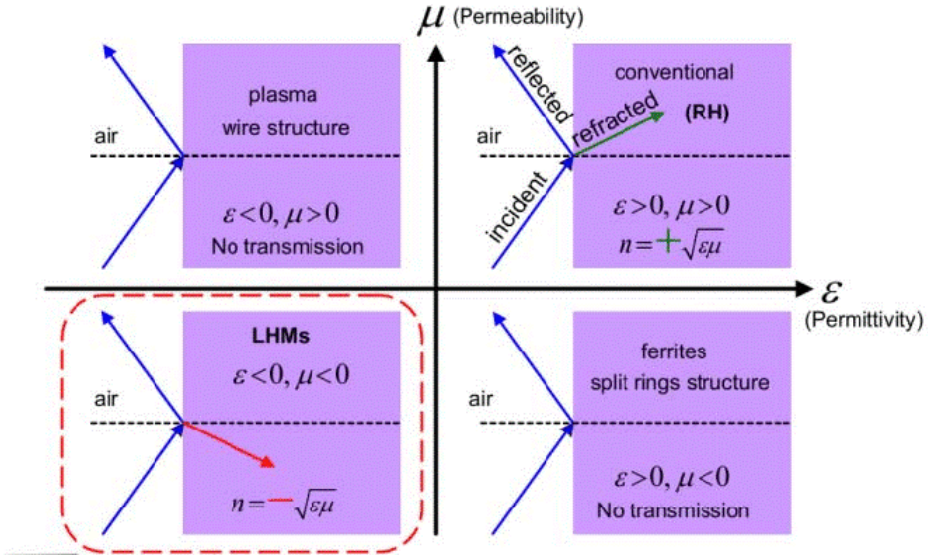

Figure 2.2: Classification of Metamaterial [49].

manipulating electromagnetic waves using metamaterials.

Numerous researchers have worked on the history of metamaterials across various fields, highlighting their many advantages and supporting a wide range of applications.

The properties of electromagnetic materials depend on two key parameters: permittivity ε and permeability μ. These parameters can be classified into four groups based on their values and characteristics Fig. 2.2.

i. Double Positive Material (DPS): In this category, permittivity ε and permeability μ have positive values greater than zero. This type of material is commonly found in the dielectric region.

ii. ENG (Epsilon Negative Material): This group's permittivity is negative (less than zero), while the permeability remains positive (greater than zero), making it an epsilon-negative material. Materials in this group exhibit a plasma frequency.

iii. DNG (Double Negative Material): In this category, permittivity and per-

meability have negative values (less than zero), leading to the term "double negative material". Such materials are artificially designed and not naturally occurring.

iv. MNG (Mu Negative Material): In this group, only the permeability is negative (less than zero), while the permittivity remains positive (greater than zero). Gyrotropic materials are common in this region.

2.3 Metamaterial Perfect Absorber

Metamaterials, engineered with artificial materials, possess remarkable properties like negative refractive index [55], inverse Doppler effect [56], superlensing [57], and electromagnetic wave cloaking [58]. They have shown significant achievements in photonic research [59–62] and have found diverse applications in nanotechnology, covering a wide range of electromagnetic waves. Advanced technology has enabled their development in microwave and photonic devices [63], tailoring their effective parameters for specific applications [64].

A particularly fascinating phenomenon of metamaterials is their ability to act as perfect absorbers, known as Metamaterial Perfect Absorption (MMPA). An artificial substance created to absorb electromagnetic radiation at particular frequencies is called a metamaterial absorber. There are limits to the extent that conventional absorbers, like those composed of carbon or ferrite, can absorb particular wavelengths. On the other hand, metamaterial absorbers are made of deliberately structured composites which exhibit special qualities that are unavailable from natural materials. This characteristic enhances the efficiency of solar energy absorption [65] and finds applications in plasmonic sensors [66], bolometers [67], wireless power transfer [68], and perfect light absorption [69–71]. The absorption is achieved through resonance formed by inductive and capacitive circuits, dissipating losses through ohmic and dielectric losses.

The primary reason metamaterials are used in stealth technology is that their special electromagnetic properties allow for the engineering of methods to manipulate electromagnetic waves that are not achievable with normally occurring materials. Because of these characteristics, metamaterials are especially well-suited for lowering an object's radar cross-section (RCS), which is a crucial component of stealth technology [72, 73]. The following explains the use of metamaterials in stealth applications.

(i) **Tailored Electromagnetic Response:** In comparison to natural materials, metamaterials can be designed to exhibit particular electromagnetic properties, such as negative permeability and permittivity. The behaviour of electromagnetic waves can be effectively manipulated and controlled by metamaterials due to these characteristics.

(ii) **RCS Reduction:** An object's radar cross-section can be reduced by using metamaterials, which can be made to scatter, absorb, or reroute incoming radar waves. The amount of radar radiation that is reflected back to the radar receiver can be reduced, allowing engineers to improve the stealth qualities of stealth aircraft or other platforms by adding metamaterials into their structure or surface coatings.

(iii) **Broad band absorbtion:** A wide range of frequencies of electromagnetic radiation can be absorbed using metamaterial absorbers. In stealth applications, when it's critical to reduce the object's detectability over many radar bands, this property is useful.

(iv) **Thin and light weight:** Although metamaterials may be designed to be thin and light, they can be included in stealth platform structural elements or surface coatings without appreciably increasing their weight or aerodynamic drag.

(v) **Flexibility in Design:** The electromagnetic properties of metamaterials can be customized by engineers to meet the specific requirements of a stealth application, according to their design versatility. With consideration for aspects like functioning frequency, platform design, and ambient conditions, this flexibility allows for the improvement of stealth performance.

Landy et al. were the first to put forward the idea of metamaterial absorbers [22,27], and they offer the advantage is its compact size and slim profile in comparison to conventional absorbers. As a result, they have been employed in various applications, such as thermal imaging [24, 29], solar cells [26], sensors [27], multiband applications [28–30, 32, 32], broadband applications [37, 69], polarization-insensitive setups [32, 34, 35, 37], and controllable band setups [38, 40, 74]. The versatility and efficiency of metamaterial absorbers make them promising candidates for numerous practical applications.

Here, Metamaterials can be categorized into non-planar metamaterials and planar metamaterials. Non-planar structures are designed for applications in the gigahertz and terahertz ranges, but planar metamaterials are widely used in terahertz applications due to their periodic arrangement and lower thickness level.

Non-planar metamaterials are characterized by complex structures and are combined with lumped elements. They are designed for specific applications in the gigahertz and Terahertz ranges [75].

On the other hand, planar metamaterials are designed with a periodic pattern of materials arranged on a plane. These structures have lower thickness levels and find applications in various fields due to their versatility. They often have unit cell structures and are preferred by many designers. Planar metamaterials also support a wide range of broadband applications.

Many structures have been developed within planar metamaterials, utilizing

periodically patterned materials on the top layer to interact with incident electromagnetic waves and reflect them from the bottom layer. These methods are particularly applicable to the terahertz range and are also suitable for broadband applications.

Researchers believe left-handed planar substrates could be fabricated for microstrip applications [76]. For example, coplanar waveguides can be used in a left-handed medium with metallic wires to achieve low-loss insertion and create high-selectivity band-pass filters [77].

Another innovative technique involves designing coplanar waveguide stop band filters coupled with split ring resonators. Each ring in the structure produces a different resonance level, with the rings placed on the backside substrate and future structures placed on top [78].

Additionally, backward wave propagation-based coplanar waveguide band-pass filters have been proposed. These filters are constructed using slender metallic wires and split ring resonators positioned on the metal layers. By adjusting the configuration of the top and bottom rings, the device can manifest either two pass bands or a single pass band with adjustable bandwidth [79].

2.3.1 Split Ring Resonator (SRR)

A simple structure called the Split Ring Resonator (SRR) has been developed to understand better the concept of metamaterials, which is particularly useful for application-oriented research. The basic SRR structure is depicted in Fig. 2.3(a), where a ring crafted from a conductive material like copper or aluminum is embedded in a dielectric material. The SRR is one of the fundamental structures commonly used in the metamaterial concept.

The operation of the Split Ring Resonator operates on the principles of Faraday's law of electromagnetic induction, where a changing magnetic field penetrates and traverses the loop, as shown in Fig. 2.3(b), This process generates

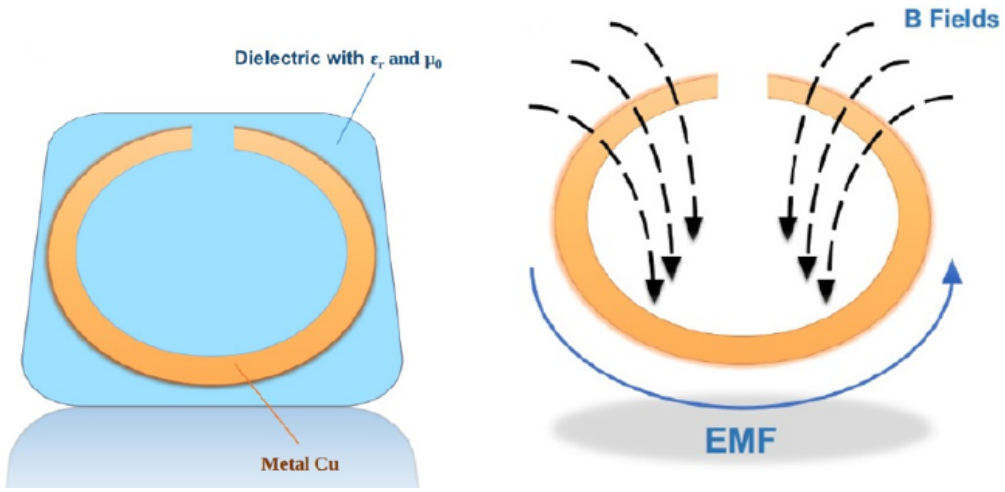

(a) (b)

Figure 2.3: (a) In this instance, we have an embedded split ring resonator (SRR) composed of copper metal. In figure (b), you can observe a magnetic field intersecting the loop, consequently producing an electromotive force (EMF) that initiates a current flow within the loop.

an electromotive force (EMF) within the loop. This phenomenon is crucial in understanding the behavior and functionality of the Split Ring Resonator and its role in metamaterial research and applications.

$$\oint_C \vec{E} \cdot d\vec{l} = -\frac{\partial \Phi}{\partial t} = -\int_S \frac{\partial \vec{B}}{\partial t} \cdot \hat{n}\, da \tag{2.1}$$

$$\vec{\nabla} \times \vec{E} = -\frac{\partial \vec{B}}{\partial x} \tag{2.2}$$

Here $\vec{E}$ the production for the electric field is characterized within a closed path C encircling the loop and $\frac{\partial \Phi}{\partial t}$ Is the changing magnetic flux passes through the central area of the loop, leading to the generation of an electromotive force (EMF) that drives current within the loop. This current, in turn, produces a magnetic field, which, according to Ampere's law, opposes the initial magnetic field direction, as illustrated in Fig. 2.4(a).

$$\oint_C \vec{B} \cdot d\vec{l} = \mu_0 I = \mu_0 \int_S \vec{J} \cdot \hat{n}\, da \tag{2.3}$$

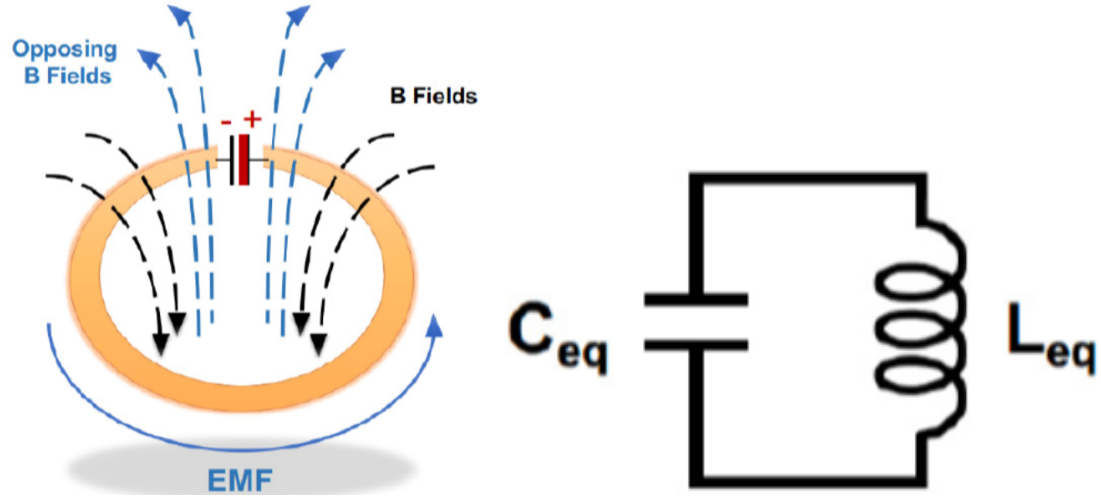

(a) (b)

Figure 2.4: (a) The split ring resonator generates a counteracting magnetic field as depicted. (b) The inductance is a component within the equivalent circuit of a split-ring resonator (L) increase due to the inductive properties of the ring, and the capacitance increase based on the rings gap. The net effective capacitance is C_eq, and the combined or total inductance is condensed as a single entity L_eq.

$$\vec{\nabla} \times \vec{B} = \mu_0 \vec{J} \tag{2.4}$$

The ring has an inducing effect. However, the ring also exhibits a capacitive effect, attributed to the presence of a gap within it. The split in the ring also functions as a parallel-plate capacitor. The SRR equivalent circuit with both inductive and capacitive effects is represented in Fig. 2.4(b). The equivalent LC circuit is associated with the natural frequency given by

$$f = \frac{1}{2\pi\sqrt{L_{\text{eq}}C_{\text{eq}}}} \tag{2.5}$$

It is demonstrated that a group of split-ring resonators (SRRs) demonstrate a negative μ_{eff} at frequencies in proximity to their magnetic resonance frequency ω_m.

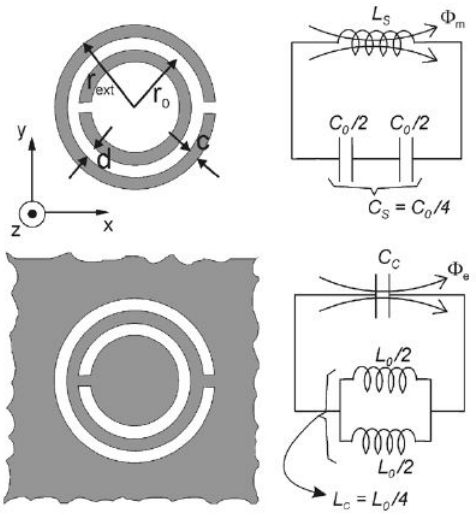

Figure 2.5: Compementary Split Ring Resonator

2.3.2 Complementary Split Ring Resonator (CSRR)

The CSRR represents a distinct structure predominantly employed in the creation of single-negative and double- negative metamaterials (LHM) tailored for particular frequency ranges. Double Negative Mediums exhibit negative permittivity and permeability, showing reversed Doppler effect, inverted Cherenkov radiation, and support for evanescent waves when either permittivity or permeability takes on a negative value. [80, 81].

The CSRR mainly produces a resonant mode, with its resonant frequency determined by its primary structure (Fig. 2.5). This resonant phenomenon arises from the interaction of metallic strips with electromagnetic fields, resulting from both capacitive and inductive effects. Researchers have designed novel structures based on CSRRs for sensing applications, particularly for single negative permeability within the millimeter-wave frequency range [82]. Experimental and computational studies have focused on single- and double-negative refractive indexed metamaterial structures. A dual-band metamaterial composed of nonconcentric, differently sized delta loop resonators has been proposed, demonstrating nega-

tive refractive index regions in single and double-negative regions [82]. Other studies have examined the effective medium ratio and the negative properties of multi-band negative indexed metamaterials based on SRRs and measured radar absorption efficiency in the frequency range of $3 - 18$ GHz [83].

The CSRR structure has been developed and proposed for various microwave applications, including C-band ($4 - 8$ GHz), X-band ($8 - 12$ GHz), Ku-band ($12 - 18$ GHz), and Ka-band ($27 - 40$ GHz), which find utility in satellite applications. These frequency bands are used in weather monitoring, long-distance communication, and various broadband coverage areas. The compactness and effectiveness of the proposed CSRR have been analyzed, with an effective medium ratio of 8.0 [84]. CSRRs have also been designed in different shapes and arrays to manipulate effective permittivity, permeability, and refractive index [85].

Furthermore, SRRs etched on the upper substrate side, close to the conductor strip, have demonstrated similar effects in microstrip technology [86]. Periodic etching of the conductor strip can create series gaps and construct broadband negative media in microstrip technology. Dual-band behaviour in SRRs can be achieved by implementing effective negative permittivity using shunt inductance and metallic vias to the ground [60]. Some researchers have shown how a narrow stopband can be produced by periodically creating the inverse pattern of SRRs by etching into the ground plane beneath the conductor strip in a microstrip line [87].

Babinet's principle has been applied in [9]for implementing metasurface and metamaterial structures, using metallic wires and plates to achieve negative ε_s. This demonstrates the diverse approaches and potential applications of CSRRs and related metamaterial concepts in electromagnetic research and device design.

2.4 Metamaterials in the THz Regime

Metamaterials are also designed and operated in the Terahertz (THz) electromagnetic spectrum. However, in the THz range, metamaterials face challenges due to weak electric permittivity and magnetic permeability, making it difficult to control radiation effectively.

Research in the Terahertz frequency range has advanced significantly, with various metamaterial structures being employed, such as include slender wires, Swiss Rolls, SRRs, electric SRRs, pairs of rods, and fishnet structures. At lower frequencies, thin wires and SRRs are frequently employed to enhance electromagnetic characteristics. However, at higher frequencies, traditional metallic elements encounter issues with power dissipation and fabrication complexity, leading to advanced structures derived from wires and SRRs to maintain desired qualities. Metamaterials have found applications in optical nanostructures, communication, microscopy, defense, and various research fields, contributing to exploring the Terahertz spectrum alongside optics.

The Terahertz range spans from 0.1 to 10 THz and presents unique challenges due to its accessibility limitations, leading to it being called the "terahertz gap". However, technological advancements have enabled tabletop instruments to produce, detect, and manipulate terahertz signals. Time-domain spectroscopy and femtosecond laser sources are commonly used techniques in this range. Terahertz radiation is nonionizing, making it suitable for human exposure applications, such as security screening and medical diagnosis. It exhibits distinctive absorption patterns in various materials based on their molecular rotational and vibrational modes, which help identify substances. Numerous nonpolar, dry, and nonmetallic materials, including fabrics, wood, cardboard, and plastics, exhibit transparency to terahertz radiation. Metamaterials play a crucial role in terahertz research, as natural materials typically lack robust magnetic and electric field reactions within

the 1-3 THz range. The terahertz gap represents an area in the region where the electromagnetic reactions of most natural materials diminish. Metamaterials can bridge this gap and offer a powerful tool for forthcoming terahertz research and advancement due to their adaptable characteristics.

Overall, metamaterials hold great potential for designing structures in the terahertz frequency range and overcoming challenges using artificial materials. This unveils fresh opportunities for exploration, testing, regulation, sensing, and generation applications within the Terahertz spectrum.

2.5 Metamaterial Perfect Absorber

In conventional electromagnetic absorbers, reflections and π phase shift radiation occur from the ground plane. A dielectric layer that is one-quarter the wavelength in thickness is added to achieve perfect absorption, providing an extra propagation phase of π. This leads to a total phase shift of around 2π radians, where the multireflection process results in constructive interference for phase-matching conditions and destructive interference for direct reflection. Engheta introduced the concept of adding a thin dielectric layer above the ground plane, increasing the impedance level from low to high and reducing the thickness of the absorber [88].

The first Metamaterial Perfect Absorber (MPA) was operated in the microwave frequency range by Landy et al. [22]. The unit cell structure (Fig. 2.6) consisted of an electric split-ring resonator (eSRR) and a cut- wire (CW) with a thin dielectric spacer in between.

Reflectance $R(\omega)$ and Transmittance $T(\omega)$ of the structure were both simulated and experimentally measured, and the absorption $A(\omega)$ was given by $A(\omega) = 1-R(\omega)-T(\omega)$. It was demonstrated that $R(\omega)$ and $T(\omega)$ could approach zero at approximately 11.5 GHz, achieving near-unity absorption. The simulation

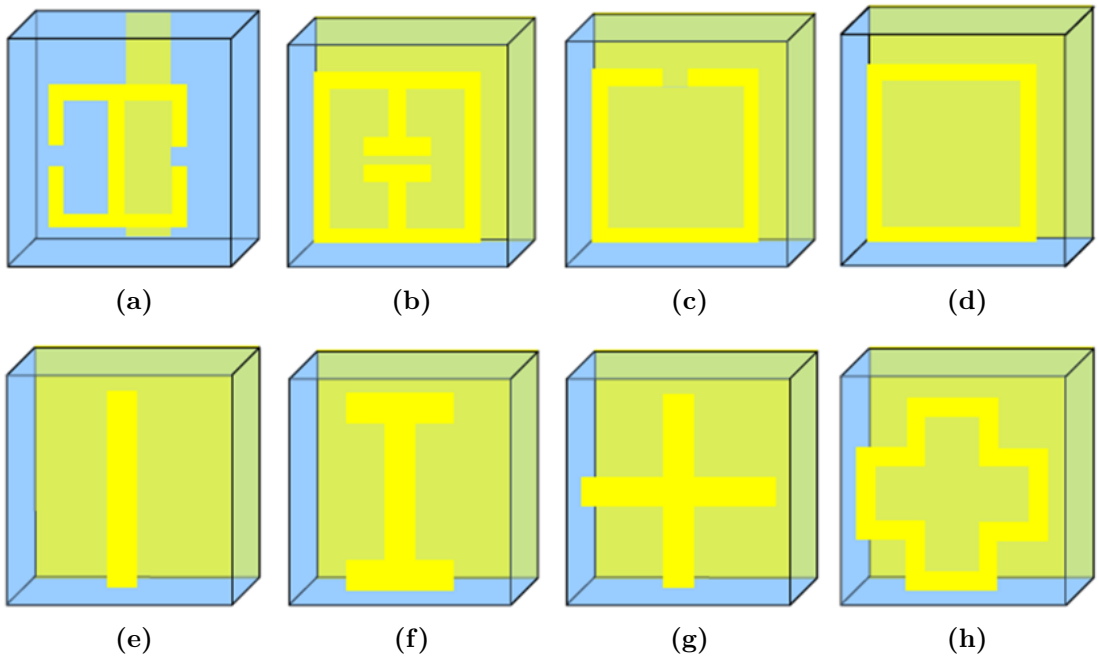

Figure 2.6: Unit cell of metamaterial.

showed an absorption $A(\omega)$ of 96%, and the experimental value was measured at 88%. However, it was observed that the absorption rapidly decreased as the incident angles increased. The total range of incident angles with $A(\omega) > 0.5$ was found to be 16^0, indicating that the metamaterial absorber exhibits polarization dependence..

This groundbreaking research on Metamaterial Perfect Absorbers opened up possibilities for achieving nearly complete absorption of electromagnetic waves at specific frequencies, making them promising candidates for various applications including radar, imaging, and communication systems.

Various structures can be designed with metamaterial narrowband absorbers, including Split Ring Resonators (SRR), Cut-wires (CW), and Frequency Selective Surfaces (FSS). Fig. 2.6 (a-c, e, f) demonstrate structures with polarization dependence, while 2.6 (d, g, h) show structures with polarization independence, enabling wide-angle operation.

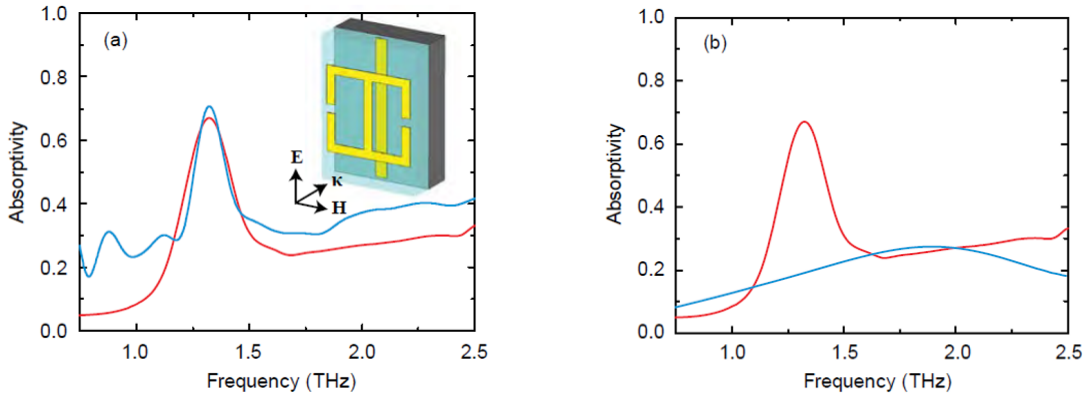

(a) **(b)**

Figure 2.7: (a) Experimentally blue line indicated and simulated line indicated in red colour for THz metamaterial absorber, (b) absorptivity for the structure when the incident electric field aligns either parallel or perpendicular to the curved wire [68, 89]

.

Fig.2.7(a) depicts the experimental and simulated absorptivity for the THz metamaterial absorber. The experiment achieved 70% absorption, while the simulation indicated 68% absorption. The structure contains a polyimide spacer with a thickness of $6\mu m$, equivalent to 1/40 of the free-space wavelength. The polarization dependency of absorption in the structure is attributed to the two-fold rotation symmetry. To achieve polarization-independent THz metamaterial ideal absorbers, structures with four-fold rotation symmetry, as seen in Fig. 2.7(b) is preferred [32, 90–93]. In certain cases, the CW array [68, 89] can be replaced by metal in the ground plane [94, 95], designed with Metamaterial Perfect Absorbers (MPAs), or similar circuit analog absorbers [96], with thinner spacing provided to them.

Fig. 2.8 illustrates the numerically simulated absorptivity for TE and TM polarizations under different incidence angles. For TM polarization, absorptivity is maintained from 0^o to 80^0. However, for TE polarization, absorptivity decreases rapidly above 40^0 angle.

Using a continuous ground plane simplifies the fabrication of samples and pre-

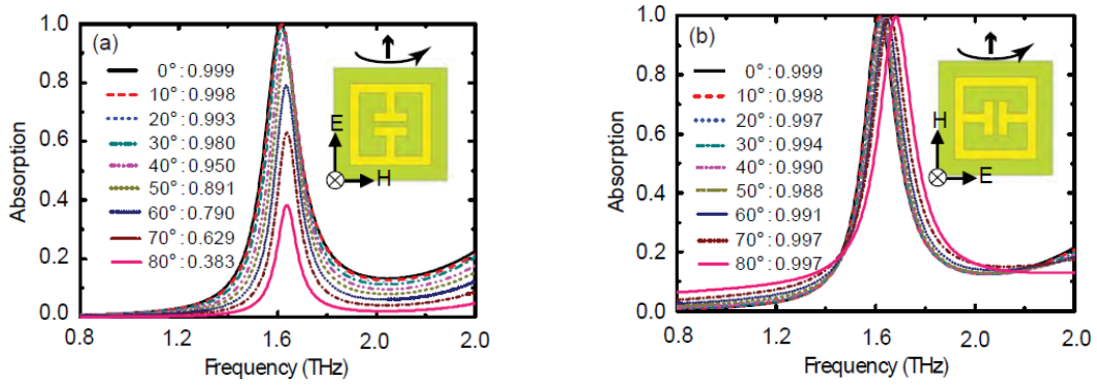

(a) **(b)**

Figure 2.8: Numerically simulated absorptivity under different incidence angles for (a) TE (b) TM.

vents incident electromagnetic waves from passing through, allowing for reflection measurements only. This simplifies the experimental setup as $T(\omega) = 0$ implies $A(\omega) = 1 - R(\omega)$.

The development of THz Metamaterial Perfect Absorbers has shown promising results, and further advancements in designing structures with specific symmetries can lead to enhanced performance and broader applications in THz wave manipulation and control.

2.6 Terahertz MM Types

Terahertz Metamaterial perfect absorbers can be classified into three types

i. Broadband

ii. Narrowband

iii. Ultranarrow band

2.6.1 Broadband Absorber

Metamaterials find application in various fields, including solar energy harvesting [64, 97, 98], biological sensing [15, 99, 100], thermophotovoltaics [101, 102],

photodetection, imaging devices [24,103,104], and absorption filtering [105]. Generally, MMPA is divided into two types: broadband and narrow band. MMPA generating single-band [22, 106–108], dual-band [32, 109, 110], and triple-band [111], and achieved more absorption peaks [112, 113] and broadband absorbers used in military applications and also civilian, They are employed in diverse areas, including photovoltaics, bolometry, photodetection, and stealth technology. However, achieving broadband absorption in the THz region remains a complex challenge. Additionally, there are still concerns regarding the limited bandwidth of localized surface plasmons generated on metallic surfaces at the nanoscale, despite their role as perfect absorbers. [114]. In GHz or lower frequency, the resonant Q- factor $Q = \frac{1}{R}\sqrt{\frac{L}{C}}$, is a significant value because of the lower resistance value [115]. Achieving perfect absorption in absorber designs becomes intricate and demanding when aiming for broadband absorption. In contrast, obtaining perfect absorption with a straightforward design is relatively straightforward at a single wavelength.

2.6.2 Narrowband Absorber

Metamaterial is made of artificial materials. The basic concept of the metamaterial to design sub-wavelength unit cells, also known as Meta-atoms or Meta-molecules, is that they have electric and magnetic responses based on electromagnetic fields. It used many applications but has some losses to overcome this loss optimizing structure geometrics. It can used in many applications, including energy harvesting [116], scattering reduction [117], and thermal sensing [118], and also place a high value on absorption. By carefully engineering the electric and magnetic resonances [22, 24, 119–123], it is possible to create metamaterials with virtually uniform absorption by exploiting the full usefulness of loss. The initial metamaterial-based perfect absorber that was discovered is characterized by a limited bandwidth and sensitivity to polarization, primarily because of its reso-

nant behavior. This restricts its practical utility in real-world applications [22].

2.6.3 Ultra-Narrowband Absorber

Metamaterial absorbers for achieving near-perfect electromagnetic absorbers are highly valuable across a wide range of applications, particularly in the field of sensing [124, 125], solar energy [126–128], Thermal emission selectively tuned to specific wavelengths [126], and radiative cooling [127]. Numerous types of Metamaterial absorbers have been discovered across multiple electromagnetic wavebands. Typically, the majority of these absorbers incorporate a structure consisting of a metal-dielectric-metal (MDM) structure; it is a moderate absorption and restricts some high- performance applications [24,26,89,95,113,128–130,130–136]. For achieving good performance, the ultra-broadband or ultra- narrow band is used today. Based on ultra-narrow band achieving in sensing or wavelength-selective thermal emission and reducing losses.

2.7 Research Gap

Despite significant advancements in Metamaterial Perfect Absorbers, there are still research gaps and challenges in different types of absorbers:

2.7.1 Broadband Absorber

Broadband absorbers are crucial for various applications, including science, antennas, modulators, filters, phase shifters, and cloaking. However, challenges remain in achieving wideband absorption and reducing multipath reflections, which lead to complete destructive interference of electromagnetic waves. The use of vanadium dioxide to increase bandwidth is limited by its layered nature. Some proposed designs achieve limited bandwidth, such as a double-ring metamaterial construction with graphene, SiO2, and gold. Research is needed to develop more efficient and practical broadband absorbers with improved performance and

reduced reflections.

2.7.2 Narrowband Absorber

Narrowband absorbers find applications in energy harvesting, scattering reduction, thermal sensing, and ultrathin sensors/bio-sensors. However, designing metamaterial-based narrowband sensors poses challenges, such as achieving a high Q-factor, polarization insensitivity, and independence from incident angles. Some dual- band absorber designs using multiple resonators show potential, but there is room for further improvement in performance and versatility. Developing narrowband absorbers with better sensitivity and more comprehensive incident angle range is an important research goal.

2.7.3 Ultra-Narrowband Absorber

Ultra-narrowband Metamaterial Perfect Absorbers are essential for sensing, solar energy, wavelength-selective thermal emission, and radiative cooling applications. Achieving ultra-narrow bandwidth with high absorption requires careful optimization of design and thickness levels. Some research has demonstrated promising results with large Q-values and Figures of Merit (FOMs). However, more investigation is required to comprehend the impact of thickness on performance and to develop practical ultra-narrowband absorbers with wide-angle operation. Overall, the research gap in Metamaterial Perfect Absorbers lies in achieving improved efficiency, bandwidth, and versatility while overcoming polarization sensitivity and incident angle limitations. Developing robust and efficient absorbers will significantly enhance the performance and applicability of metamaterial-based absorbers in various applications across different frequency ranges, including Terahertz.

2.8 Objective of Thesis

The thesis aims to address the identified research gaps and contribute to the field of THz Metamaterial Absorbers. The specific objectives are as follows:

i. Design and development of THz Metamaterial absorber for different configurations such as SRR, CSRR, OSRR.

ii. Characterization of THz Metamaterial absorber for multi-band application.

iii. Utilization of developed THz Metamaterial absorber for its possible application in sensing and imaging.

iv. The performance evaluation of simulated results with state-of-the-art techniques.

By accomplishing these objectives, the research aims to contribute to the advancement of THz Metamaterial Absorbers, providing insights into their design, characterization, and potential applications in various fields, particularly sensing and imaging. The research findings are expected to enhance the understanding and utilization of Metamaterial absorbers operating within the terahertz (THz) frequency range.

3

A Graphene-Based Broadband Metamaterial Absorber

Contents

3.1 Introduction

Metamaterials, created using artificial materials, have demonstrated remarkable potential across various applications. However, while these materials operate within the THz frequency range, untapped possibilities and specific applications demand attention. The capability of metamaterials can be enhanced by incorporating intricately designed resonant unit cell structures. These modified metamaterials exhibit features like absorbing frequency tuning, polarization modulation, and the ability to switch between reflection and absorption [38, 137, 138]. Achieving these functionalities often involves the integration of diodes or varactor components into the unit cells of microwave-frequency metamaterials. Notably, THz metamaterials have seen the incorporation of integrated Schottky diodes on n-type GaAs substrates, resulting in explosive THz transmission modulation [65]. To further extend the scope of designed tunability, such as frequency tuning and polarization modulation, novel approaches are required to blend suitable materials into metamaterial constructs effectively.

3.2 Graphene: A Versatile 2D Atomic Crystal

Graphene, the pioneering two-dimensional atomic crystal structure, holds remarkable significance. Possessing a multitude of material parameters, Graphene exhibits exceptional mechanical attributes, including stiffness, strength, and elasticity. Moreover, it boasts remarkable electrical and thermal conductivity, among other qualities. This unique combination implies that Graphene can replace existing materials in various applications. Beyond this, Graphene's exceptional properties could pave the way for various innovative technologies thanks to its all-encompassing capabilities.

The synergy of transparency, conductivity, and elasticity makes Graphene particularly promising for flexible electronics. Furthermore, its amalgamation

of transparency, impermeability, and conductivity renders it advantageous for applications like transparent protective coatings and barrier films. However, the pivotal question arises: Does Graphene's adaptability and distinctiveness justify the substantial investments and prolonged efforts often required to transition to a new technology.

3.3 Graphene Properties: Unveiling Remarkable Attributes

Graphene, often called the "miracle material," boasts many extraordinary properties, setting it apart as a remarkable substance. These attributes have been meticulously measured and experimentally observed, yielding intriguing results. Notable characteristics include an electron mobility of $2.5 \times 10^5\,\mathrm{cm^2\,V^{-1}\,S^{-1}}$ [139] at room temperature, Young's modulus with 1TPa, and intrinsic concentration upto130 GPa [140, 141]. Graphene exhibits impressive thermal conductivity exceeding $3000 W m K^{-1}$ [142], and optical absorption of approximately $\pi\alpha \approx 2.3\%$. Moreover, it showcases unparalleled impermeability to gases [143] and can accommodate high densities of electric current [144]. Additionally, Graphene can be chemically functionalized [145–147], expanding its versatility.

Although Graphene possesses extraordinary attributes, it is essential to note that these qualities are often realized in high-quality samples [148], typically deposited on substrates like hexagonal boron nitride [149]. Although advancements are rapidly being made in this direction, achieving consistent features in Graphene produced through alternative methods is still challenging. The goal is for mass-produced Graphene to exhibit the exceptional performance demonstrated by the best research lab samples, making it even more appealing for industrial applications.

As the pioneer of 2D atomic crystals, Graphene has counterparts such as

boron nitride and molybdenum disulfide [150], forming a diverse family of 2D crystals and heterostructures [151, 152]. This diversity enhances the prospects of Graphene's commercial viability as it becomes part of a broad and varied category.

The trajectory of Graphene applications is inevitably tied to its development with tailored properties for specific uses, a continuous process expected to span the next several decades. Various shapes and dimensions are designed based on Graphene, utilizing distinct quality methods. Depending on the resultant Graphene quality, applications fall into three categories: (1) Graphene and its derivative, reduced Graphene oxide flakes, offer versatility in applications, including composites, conductive paints, and more. (2) Planar Graphene, known for moderate performance, suits both active and non-active devices. (3) Planar Graphene excels in high-performance electronics.The selection of Graphene type hinges on factors such as material quality and substrate, driving the production methodology. The selection of Graphene type hinges on factors such as material quality and substrate, driving the production methodology.

In production, the liquid-phase exfoliation process involves exposing materials to a solvent that increases the total surface area of graphite crystallites [153,154]. This method yields individual Graphene platelets through sonication, with extended treatment leading to a significant proportion of monolayer flakes suspended, further concentrated through centrifugation. An analogous approach involves the exfoliation of graphite oxide, achieved by oxidizing graphite pellets followed by ultrasonically exfoliating them in an aqueous solution [155]. This suspension can then be converted into a thin film on various surfaces, partially reverting to the parent Graphene state in situ. Another variation employs a thermal shock technique, which simultaneously exfoliates and reduces aqueous-based graphite oxide, offering industrial significance [156]. Additionally, suspensions of Graphene nanoribbons can be generated via techniques like unzipping single-

wall carbon nanotubes [157, 158], allowing precise control over Graphene platelet distribution.

Graphene finds utility in myriad applications, spanning fields such as paints, inks for supercapacitors, heat dissipation, barrier coatings, electromagnetic shielding, electronics, and intelligent windows [159]. With prototypes already showcasing conductive ink applications, we anticipate an array of flake-based products entering the market in the coming years.

3.3.1 Chemical Vapor Deposition: Paving the Path for Large-Scale Graphene Production

The advent of chemical vapor deposition (CVD) has arisen by way of a promising technique for fabricating expansive and uniform polycrystalline Graphene sheets, heralding many potential applications [160]. Notably, Graphene production spanning square meters has already been achieved, even though the customary process entails transferring from a copper substrate onto a dielectric surface or other target substrates [161]. Encouragingly, these films have been successfully applied to 200-mm Si wafers, forming the foundation for cutting-edge device demonstrations. Transport characteristics comparable to exfoliated Graphene have been observed in these films when placed on SiO_2 and hexagonal boron nitride substrates. Despite imperfections, grain boundaries, and thicker layers, these films exhibit suitability for deployment in transparent conductive coatings, including applications like touch screens.

Although the CVD technique holds great promise, it currently bears elevated costs due to energy consumption and the necessity to eliminate the underlying metal layer. Nonetheless, as the transfer process is refined, the potential for this approach to be both disruptive and cost-effective becomes increasingly tangible. A series of challenges, however, need to be surmounted before widespread adoption of the Graphene CVD technique becomes feasible. Key objectives include the

generation of Graphene on minute metal sheets (tens of nanometers thick), accompanied by meticulous control over domain size (grain), ripples, doping levels, and layer count. The ability to regulate the quantity of Graphene coatings and their crystallographic orientation is pivotal, as it opens avenues for applications that would conventionally require double, triple, or even thicker Graphene layers. In parallel, optimization and enhancement of the transfer method are vital to retrieve the sacrificial metal and minimize potential harm to Graphene. A potential transformative stride lies in achieving Graphene growth directly on surfaces, eliminating the intricate and costly transfer step. Graphene's conformal growth on metal surfaces has already displayed noteworthy outcomes: enhancing the recital of copper inter-connects in integrated circuit, courtesy of its exceptional thermal and electrical conductivity and formidable barrier properties. Furthermore, Graphene forms a seamless layer on intricate metal surfaces, rendering it an effective barrier to gases and a corrosion-resistant coating. Revolutionary advancements would entail the ability to instigate Graphene growing on diverse surfaces or/and at lower heats, harnessing techniques like plasma-improved CVD. Such feats would circumvent complex transfer steps and facilitate tighter integration of this two-dimensional crystal with complementary components, such as Si or GaAs. Pursuing these objectives stands to redefine the landscape of Graphene's industrial applications.

3.3.2 Synthesis on Silicon Carbide (SiC): Paving the Path Toward High-Quality Graphene

Silicon carbide (SiC) is a familiar material renowned for its application in high-power electronics. An intriguing avenue has emerged through the sublimation of Si atoms, leading to the creation of graphitic layers on either the silicon or carbon facets of a SiC slice. This process bequeaths a graphitized surface [162]. Initially, a turbostratic stack encompassing multiple randomly ori-

ented polycrystalline layers [163] was cultivated on the carbon-terminated facet of SiC. This paradigm has evolved, enabling control over the number of Graphene layers grown [164]. Remarkably, this variant of Graphene can exhibit exceptional quality, with crystallite dimensions extending to hundreds of micrometers [165].

Nonetheless, this method harbors limitations, notably the elevated cost of SiC slices and the requirement for high heats (exceeding 1000^0C), which do not align with prevailing silicon electronics technology. An avenue to exploit Graphene growth on SiC involves generating thin SiC layers on silicon, although this strategy necessitates further exploration. While the utilization of Graphene on SiC holds promise, it may be confined to specialized applications due to the demanding conditions of high-temperature growth, costly substrates, and diminutive wafer diameters.

As current technology based on III-V materials approaches its threshold at approximately 1 THz, the emergence of high-frequency transistors founded on SiC-grown Graphene [166] appears plausible within the next decade. Even the existing 20-mm domain size attained in Graphene synthesized on SiC prove appropriate aimed at such applications, particularly in the realm of short-gate transistors that are prevalent today. A distinctive advantage of Graphene grown on SiC is enhanced resistance accuracy at elevated temperatures compared to GaAs heterostructures, presenting another compelling yet niche application [167].

In the trajectory forward, the challenges on the horizon include addressing issues like terrace removal, the growth of subsequent layers at terrace edges (which significantly contribute to carrier scattering), augmentation of crystallite sizes, and management of unintentional substrate and buffer layer doping. These concerns and the formidable temperature requisites for growth are focal points demanding resolution in the ensuing decade.

Advancements in Graphene materials present exciting avenues for research. A noteworthy technique entails the production of high-quality Graphene nanorib-

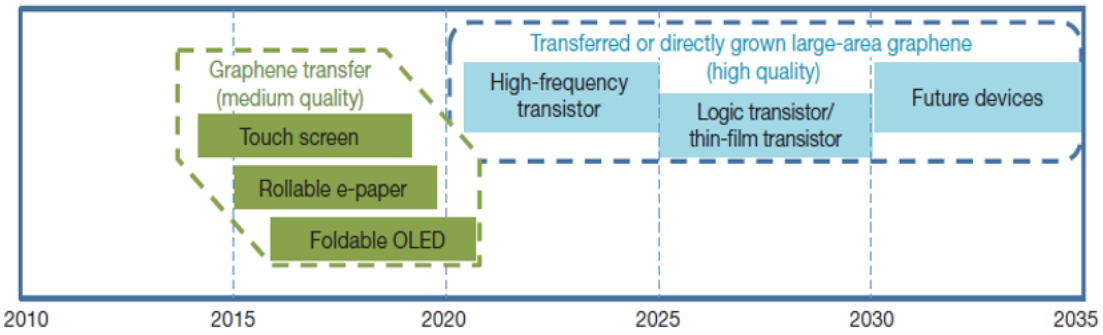

Figure 3.1: Graphene based display and electronic devices. Green color rindicates for application and blue color indicate electronic application [171].

bons and intricate structures (such as T-and Y-shaped influences) [168] through a chemistry-centric bottom-up method, known as the "surface-assisted linkage of molecular monomer precursors to form linear polyphenylenes" [168], followed by cyclodehydrogenation. Molecular beam epitaxy has demonstrated the capacity to yield chemically pure Graphene [169]. However, its relatively higher cost vis-à-vis CVD techniques makes it an improbable candidate for large-scale deployment. Laser ablation also emerges as a potentially intriguing technique for layer growth on surface materials [170].

3.3.3 Graphene Electronics

The deployment of Graphene as a planar channel substantial for high-performance integrated logic circuits within the coming decade remains uncertain, primarily due to its inherent lack of a bandgap. Despite this, Graphene has emerged as a versatile material, finding its niche in various applications, as delineated in the comprehensive table, with corresponding methods elucidated [171]. It is shown in the figure for Graphene-based samples can be established (Fig. 3.1). Notably, layers of transparent-conductive remain a prime exemplar of Graphene's utility, integrating extensively in electronic devices like organic light-emitting diodes (OLEDs), e-papers , and display with touch screen. The requisites of squat piece resistance, coupled through much transmittance (often around 90%), dictate the

Table 3.1: Graphene properties with different methods

Methodology	Extent of Crystallite (μm)	Simple extent (mm)	Charge carrier mobility(at ambient heat) ($cm^2V^{-1}s^{-1}$)	Applications
Mechancial exfoliation	> 1000	> 1	$> 2 \times 10^5$ and > 10^6 (at low temperature)	Research
Chemical exfoliation through Graphene oxide	$\sim$ 100	Infinite as a coating of overlapping flakes	1(for a layer of overlapping shavings)	Coatings, paint/ink, composites, transparent conductive layers, energy storage, bio-applications
Chemical exfoliation through Graphene oxide	$\leq$ 0.1	Countless as a coating of overlapping flakes	100 (for a coating overlying flakes)	Coatings, paint/ink, composites, transparent conductive layers, energy storage, bio-applications
CVD	1000	$\sim$ 1000	10000	Photonics, nanoelectronics, transparent conductive layers, bioapplications, devices
SiC	50	100	10000	Huge-frequency transistors then additional electronics device

success of these coatings in their designated roles. Herein, Graphene, exhibiting exceptional electrical and optical attributes, attains sheet resistance values as low as 30Ωper square area of 2D in extremely nobbled configurations. Furthermore, its transmittance prowess is evident, with a remarkable 97.7% per layer. While indium tin oxide (ITO) boasts commendable characteristics, Graphene's steady advancements, while enhancing year by year, are underpinned by factors of enhanced affordability and heightened security, placing it ahead of ITO in the realm of flexible electronics and chemical durability.

The requirements of electrical properties are different from one application to one application. Depending on the manufacturing process, Graphene can create several classes of transparent conductive coatings. Thus, electrodes require

more resistance (50-300Ω per square), and transmittance achieved of 90% (CVD method is more expensive).

Since Graphene has a much higher endurance than any currently available alternative, Graphene electrodes in touch panels have a distinct advantage. Generally, Graphene treated 10times better than ITO, connotation Graphene can conveniently and positively remain functional on that device.

Rollable e-paper remains self-same attractive electronic creation, necessitates a range for a curve 5-10mm, easily achievable by a Graphene electrode. Furthermore, color e-papers benefit from Graphene's consistent absorption throughout the visible spectrum. However, there is still a problem with a resistance at the interface among the metal line and Graphene electrode within the drive circuitry.

OLED is one of the good technologies, and it is a non Graphene material product. It has sheet resistance below 30Ω per square; the other parameters are work function electrode surface roughness used for perfect performance. The Graphene function helps improve performance to avoid electrical shorts and leakage currents. Graphene has already been introduced in OLED test cells. OLED device introduced in 2016 after resolving issues (like conformal deposition of Graphene on three-dimensional structure and contact resistance between Graphene and the source/drain).

In the low-cost sector totally set up for mass production. Liquid phase exfoliation produces such Graphene coating without using vacuum technology. The resistance of the Graphene maintained always high value so it can use many applications like window, solar cells and touch screen applications. Graphene always flexible and strength high, supporting many applications.

3.3.4 High-Frequency Transistors

Graphene is also used in high-frequency transistor applications [166]. Still, it has to participate against more mature technologies such as compound semi-

conductors (III-V materials). Graphene will be introduced after 2021 when even III-V material did not satisfy device performance. After 2021, according to projections, III-V material does not capable of attain a necessary cutoff frequency $f_T = 850$GHz (current modulation top frequency) and supreme oscillation frequency$f_{max} = 1.2$THz (power modulation top frequency) since expedient specifications may tighten up. Recently, Graphene cutoff frequency reached 300GHz to 1THz with a channel length of 100 nm [172,173]. According to the 2011 International Technology Roadmap for innovative materials like Graphene, f_max takes solitary achieved 30GHz in conventional Graphene designs, which is considerably behind 330GHz Si maximum frequency transistor capability.

The logic transistor in Si knowledge can be protracted to closely or level under 10nm. Graphene technology will replace Si technology after 2020. It has many issues like bandgap, nanoribbon [168, 174], single electron transistor [175, 176] formation, bilayer control [177]. The issues can resolved by using a new transistor design. When typical incoming light is incident on Graphene, electrons act by way of massless two-D particle, which causes sizeable wavelength-sovereign absorption ($\pi\alpha = 52.3\%$) for light below roughly 3 eV.

Additionally, due to Pauli blocking, mono and bi-coating Graphene becomes entirely translucent if the optical-energy lesser as twice the Fermi level [178]. One of the photonic devices that is now being researched the most is Graphene photodetectors. Graphene can theoretically be utilized to a broad spectral-range, thorugh ultraviolet to infrared, unlike semiconductor photodetectors with a constrained detecting spectral width. One of the most important active components in optical interconnects, optical modulators change the properties of light [142], including its phase, amplitude, and polarization, utilizing electro-refraction or electro-absorption to encode transmission data. Ultrafast passively mode-locked lasers have been used for many applications such as spectroscopy, material micromachining [179], bio-medicine [180], and security applications.

Most research has been done on fiber and solid-state lasers [181], but semiconductor laser technology can also utilize Graphene-saturable absorbers. A laser array with various wavelengths is necessary for optical connections using a wavelength-division-multiplexing system. Using a single laser having many longitudinal modes, such as a mode-locked laser [182], is one technique to supply a variety of wavelengths.

3.3.5 Conductivity of Graphene

BasicallyGraphene was considered an infinitesimally thin surface, a monoatomic thin surface. Conductivity is the best measure to describe the electromagnetic properties of Graphene due to its gapless electronic band structure. Therefore, "the Graphene sheet is represented by its surface current and surface conductivity, realted with the tangential electric field within the Graphene plane."

Fig. 3.2 shows that Graphene piece with the incidence of static magnetic field $\vec{B}_0 = \hat{z}B_0$ and electric field $\vec{E} = \hat{x}E_x$. The electric field force $\vec{F}_e = -\hat{x}_e E_x$, The electron has the ability to traverse through Graphene in the $-X$ direction. In general, the electron moves with a velocity given by $\vec{v} = -\hat{x}v_x$. This motion is influenced by the attractive field strength $\vec{F}_m = -e\vec{v} \times \vec{B} = -\hat{y}eB_0v$, which diverts the electron towards the $-Y$ direction. As a result, the induced current exhibits two distinct mechanisms, namely $\vec{J} = \hat{x}J_x + \hat{y}J_y = \hat{x}\sigma_{xx}E_x + \hat{y}\sigma_{yx}E_x$.

Similarly, in the presence of an electric field $\vec{E} = \hat{y}E_y$ and a stationary attractive field $\vec{B}_0 = \hat{z}B_0$, the induced current transforms into $\vec{J} = \hat{x}J_x + \hat{y}J_y = -\hat{x}\sigma_{yx}E_x + \hat{y}\sigma_{xx}E_x$.

Therefore, one of the important properties of Graphene is magnetically persuaded gyrotropy, can expressed in mathematical form:

$$\vec{j} = \boldsymbol{\sigma} \cdot \vec{E} \tag{3.1}$$

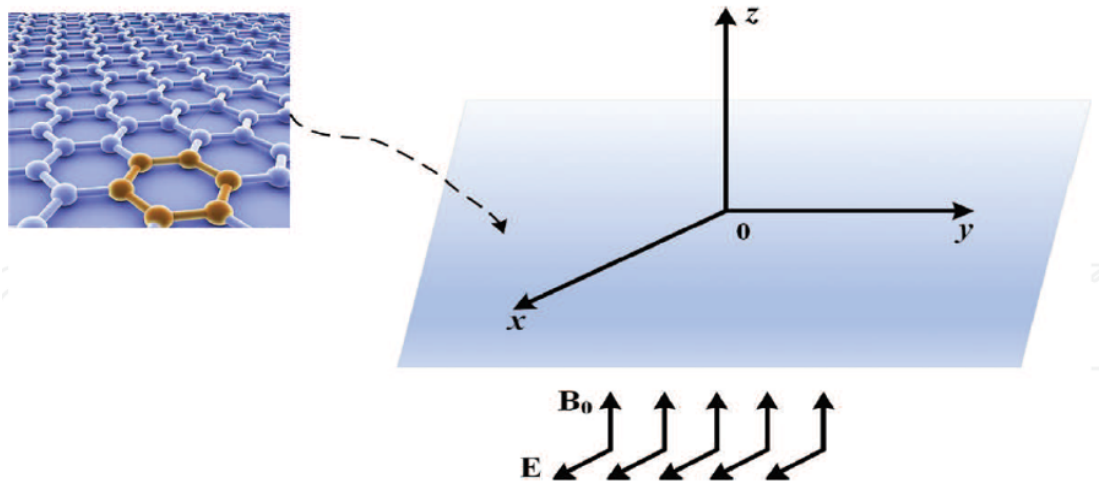

Figure 3.2: A Graphene piece by a stationary magnetic field.

where

$$\boldsymbol{\sigma} = \begin{bmatrix} \sigma_{xx} & -\sigma_{yx} \\ \sigma_{yx} & \sigma_{xx} \end{bmatrix} \tag{3.2}$$

The kubo formalism can be expressed as conductivity tensor of Eq. 3.3.5 and also the expression $\sigma_(xx)$ and $\sigma_y x$ with zero energy gap [183, 184].

$$\sigma_{xx} = \frac{e^2 v_F^2 |eB_0|}{-j\pi} \sum_{n=0}^{\infty} \frac{(n_F(M_n) - n_F(M_{n+1}) + n_F(-M_{n+1}) - n_F(-M_n))}{(M_{n+1} - M_n)[(M_{n+1} - M_n)^2 - h^2(\omega - j2\Gamma)^2]} + \frac{n_F(M_n) - n_F(M_{n+1}) + n_F(-M_{n+1}) - n_F(-M_n)}{(M_{n+1} + M_n)[(M_{n+1} + M_n)^2 - h^2(\omega - j2\Gamma)^2]} \tag{3.3}$$

$$\sigma_{yx} = -\frac{e^2 v_F^2 |eB_0|}{\pi} \sum_{n=0}^{\infty} \frac{n_F(M_n) - n_F(M_{n+1}) + n_F(-M_{n+1}) - n_F(-M_n)}{(M_{n+1} - M_n)^2 - h^2(\omega - j2\Gamma)^2} + \frac{n_F(M_n) - n_F(M_{n+1}) + n_F(-M_{n+1}) - n_F(-M_n)}{(M_{n+1} + M_n)^2 - h^2(\omega - j2\Gamma)^2} \tag{3.4}$$

"where $v_F \approx 10^6\,\mathrm{m/s}$ v_F is the velocity, $n_F(y) = 1 + \exp\left(\frac{y-\mu_c}{k_B T}\right)^{-1}$ represent Fermi-Dirac distribution, $M_n = \sqrt{2v_F^2 hn|eB_0|}$ inidcate energy of the nth Landau level, μ_c is belongs to chemical potential,$\tau = \frac{1}{2\Gamma}$ is the scattering time, e is the charge of an electron, h represents planck's constant, T is the temperature, K_B

represents Boltzmann constant."

Magnetic field have low limit then Eqns. 3.3 and 3.4 can be rewritten as [185]

$$\sigma_{xx} = -\frac{je^2(\omega - 2j\Gamma)}{\pi h^2}\left[\frac{1}{(\omega - 2j\Gamma)^2}\int_0^\infty \epsilon\left(\frac{\partial n_F(\epsilon)}{\partial \epsilon} - \frac{\partial n_F(-\epsilon)}{\partial \epsilon}\right)d\epsilon - \int_0^\infty \frac{n_F(-\epsilon) - n_F(\epsilon)}{(\omega - j2\Gamma)^2 - 4\left(\frac{\epsilon}{h}\right)^2}d\epsilon\right] \tag{3.5}$$

$$\sigma_{yx} = -\frac{e^2 v_F^2 B_0}{\pi h^2}\left[\frac{1}{(\omega + 2j\Gamma)^2}\int_0^\infty \epsilon\left(\frac{\partial n_F(\epsilon)}{\partial \epsilon} + \frac{\partial n_F(-\epsilon)}{\partial \epsilon}\right)d\epsilon + \int_0^\infty \frac{1}{(\omega + j2\Gamma)^2 - 4\left(\frac{\epsilon}{h}\right)^2}d\epsilon\right] \tag{3.6}$$

Where ω is the radian frequency. Here Eq. 3.5 and Eqn. 3.6 are valid for this condition $\sqrt{\frac{h|eB_0|v_F^2}{c}} \leq \Gamma$ Particularly absence of biased magnetic filed, we have $\sigma_{yx} = 0$ and thus Graphene reaching isotropic. Here Eq. 3.5 and Eq.3.6 have two types, One is associated with intra-band influence, while the other represents inter-band influence. The intra-band term in Eq.3.5 can be obtained analytically as referenced in [186].

$$\sigma_{xx,\text{intra}} = -j\frac{e^2 k_B T}{\pi h^2(\omega - j2\Gamma)}\left(\frac{\mu_c}{k_B T} + 2\ln\left(e^{\frac{\mu_c}{k_B}} + 1\right)\right) \tag{3.7}$$

The Eq.3.7 represents, the intra-band term adheres to the Drude model form, with the real part being positive and the imaginary part being negative.

$$\sigma_{xx,\text{inter}} = -j\frac{e^2}{4\pi h}\log\left(\frac{2|\mu_c| - (\omega - j2\Gamma)h}{2|\mu_c| + (\omega - j2\Gamma)h}\right) \tag{3.8}$$

The Eq. 3.8 represents if$\Gamma = 0$ and$(2|\mu_c| > h\omega)$,$(\sigma_{xx,intra} = j\sigma^{"}_{xx,inter})$ develops purely imaginary value. At the event of $\Gamma = 0$ and $(2|\mu_c| > h\omega), (\sigma_{xx,intra} = j\sigma^{"}_{xx,inter})$ belongs complex number, the imaginary still positive and real part $(\sigma^{"}_{xx,inter} = \sigma_{min} = \frac{\pi e^2}{2h})$ and $\mu_c \neq 0$ Low-frequency electrical transmission is mostly accounted for by intra-band conductivity, whereas optical excitations are mostly accounted for by inter-band conductivity.

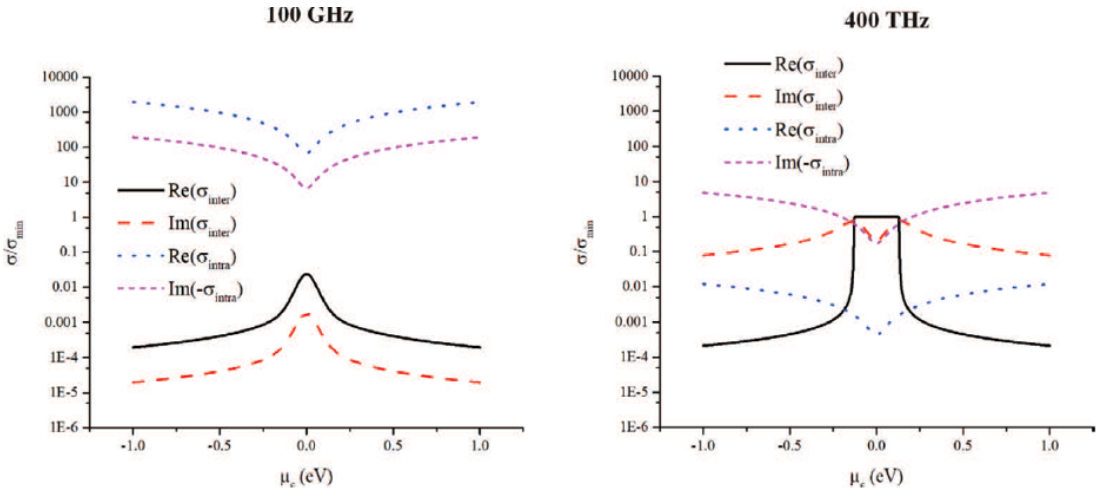

Figure 3.3: Conductivities of an isotropic Graphene at various frequencies: intraband and interband conductivities.

One of Graphene's key benefits is that chemical doping or a gate voltage can be used to adjust the material's chemical potential. The following formula [186] relates the carrier density n_s and μ_c for an isolated Graphene sheet.

$$n_s = \frac{2}{\pi h^2 v_f^2} \int_0^\infty \epsilon[f(\epsilon) - f(\epsilon + 2\mu_c)] \square d\epsilon \tag{3.9}$$

A monolayer of Graphene is created on an oxidized silicon (Si) substrate. Fig. 3.6 depicts the application of a gate voltage, referred to as V_g. This gate voltage leads to a change in the carrier density of the Graphene, as detailed in [187].

$$n_s = \frac{\varepsilon_0 \varepsilon V_g}{t_e} \tag{3.10}$$

Where ε_0 and ε belong to permittivity of free-space and substrate, and t stays reperesented as thickness for substrate. Eq. 3.9 and 3.10 can be written interns of chemical potential and gate voltage as [188]

$$\mu_c = h v_f \sqrt{\frac{\varepsilon_0 \varepsilon}{e t V_g}} \tag{3.11}$$

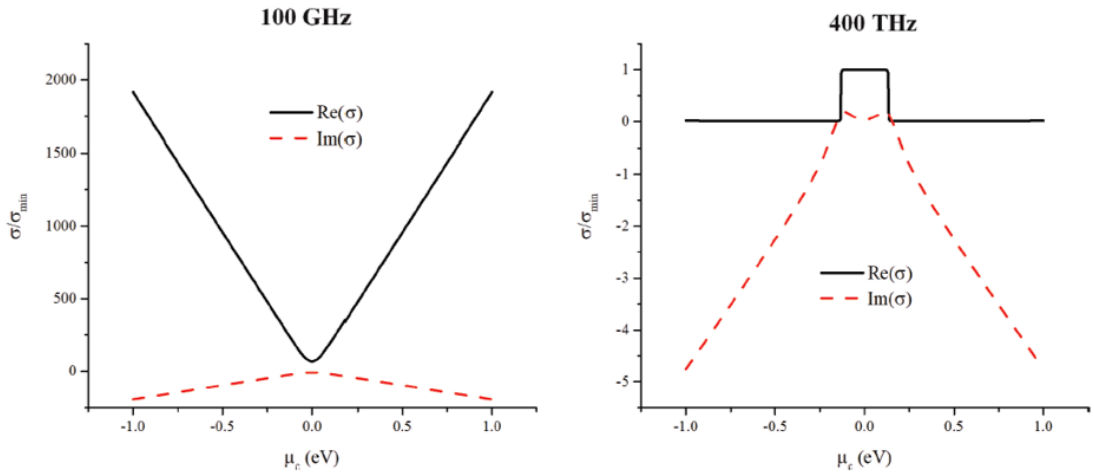

Figure 3.4: Isotropic Graphene sheet overall conductivities at varying frequencies.

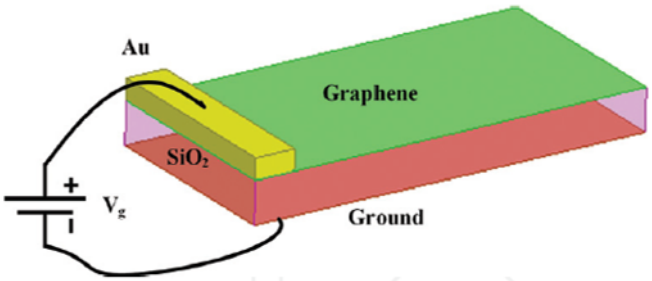

Figure 3.5: A Graphene sheet subjected to an external gate voltage.

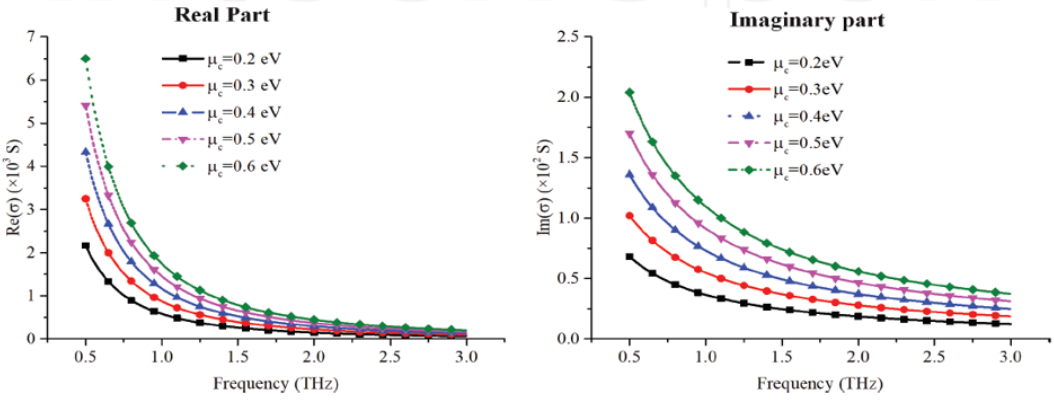

Figure 3.6: Total conductivity of the Graphene and chemical potential.

3.3.6 Terahertz Waves using Graphene Metamaterial

Terahertz frequencies, situated in the far-infrared region of the electromagnetic spectrum, hold considerable importance in the fields of photonics and electronics [189, 190]. At terahertz radiation, an inefficient response is produced because of the limitation of free carrier density and the electrically tunable semiconductor devices operating at room temperature [191, 192]. The efficient modulation of terahertz waves has concerned much courtesy in the last decade.

Various techniques have been employed to achieve significant amplitude and phase modulations in terahertz modulators and metamaterial-semiconductor hybrid structures. These techniques include the utilization of a semiconductor two-dimensional electron gas (2DEG) system and a hybridized metamaterial with a charge carrier injection/depletion mechanism. Specifically, a Schottky diode (as cited in [65,193]) or a high-electron-mobility transistor (as referenced in [194]) can be used as the charge carrier injection/depletion mechanism. It is worth noting that the terahertz modulator and metamaterial-semiconductor hybrid structure exhibit a substantial amplitude modulation of approximately 30% and a phase modulation of about 32.1 degrees. In contrast, the 2DEG system demonstrates a limited modulation depth, with a value of roughly 3% at room temperature.

Previous attempts relied on the injection of charge carriers to modify the conductivity in large substrates. It is important to highlight that the density of electron carriers, particularly in two-dimensional electron gases (2DEGs), is limited to an approximate value of $1 \times 10^{12} cm^{-2}$ within the limit of semiconductor breakdown [195].

A possible alternative method that could be considered involves the use of Graphene, a two-dimensional atomic structure. This material has the ability to significantly modify the Fermi level and the corresponding density of charge carriers through a simple process of electric gating. The capacity of Graphene to

handle charge carriers is an order of magnitude greater ($10^{13}-10^{14}cm^{-2}$) [196,197] than the capabilities of traditional 2DEG systems. Furthermore, the light-matter interaction can be fully maximized at the extreme sub wavelength scale thanks to the minimal effective mass of charge carriers in Graphene.

3.4 Graphene Using Absorber Design

Hysteresis in electrical transport results from flaws in Graphene-based devices, such as grain boundaries, adsorbed H_2O molecules, and other impurities functioning as charge trap sites on dielectric substrates or a Graphene sheet [198]. Graphene-based electronic memory systems can now be implemented utilizing electrochemical modification [199], Graphene oxide [200], or ferroelectric materials [192] thanks to this bistable behavior.

In contrast, the optical conductivity of Graphene can be shifted due to hysteresis, which can be induced by the retention of charge carriers or a delayed response to equilibrium. This shift holds promising prospects for the development of photonic memory applications, particularly within phase-change memory metamaterials [201]. The approach described in this study involves a light-matter interaction that is controlled by an electrical stimulus. This interaction takes place within a hybrid system composed of fabricated meta-atoms and two-dimensional carbon atoms. By combining the exceptional electrical and optical properties of Graphene with the robust resonance of meta-atoms, this innovative approach achieves an unprecedented level of light-matter interaction. As a result, it enables the persistent switching and linear modulation of terahertz wave transmission at an extremely subwavelength scale, which is ($< \lambda/1,000,000$). For a more detailed understanding of the structure designed using gate-controlled, terahertz Graphene metamaterial, please refer to Fig. 3.7.

The Graphene-uneven dielectric layered scheme is used, and this structure

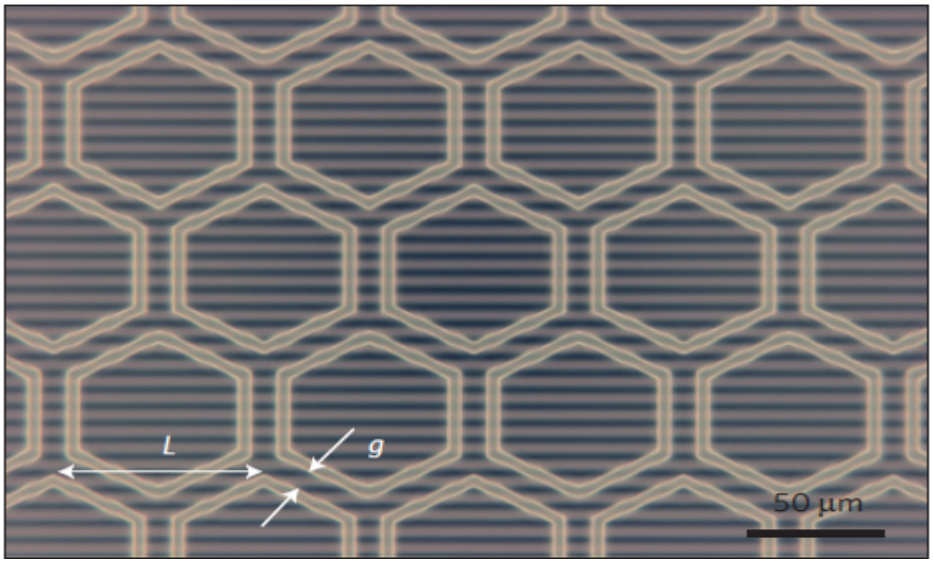

Figure 3.7: The fabricated gate-controlled active Graphene metamaterial with a hexagonal shape [203].

also allows frequency-wide Terahertz band and polarization. Based on chemical potential energy controlled with a Graphene-based absorber and used with large intervals, its conductivity was adjusted by Graphene voltage. It has many applications in spectroscopic detection, thermal detectors, polarization-sensitive sensors and tunable broadband planar filter [202].

Due to its unusual and special qualities, Graphene, two-dimensional honeycomb structure of carbon atoms, has been used in electrical and photonic devices. In THz frequency range Graphene layer also working as resistive film. It can consider as drude-like surface [204]. Generally carrier concentration controlled by chemical modification used [203, 205–207]. A Graphene-based Salisbury Screen THz absorber was explained. The sheet resistance was modified using chemical doping to achieve perfect absorption [208]. Here the structure designed polarization independent metamaterial absorber with tunable resonance frequency using with Graphene wires. According to simulation results, the absorption peak frequency can be actively changed in the lower terahertz range by adjusting the bias voltage on the gated Graphene wires. Metamaterial absorbers have a tuning

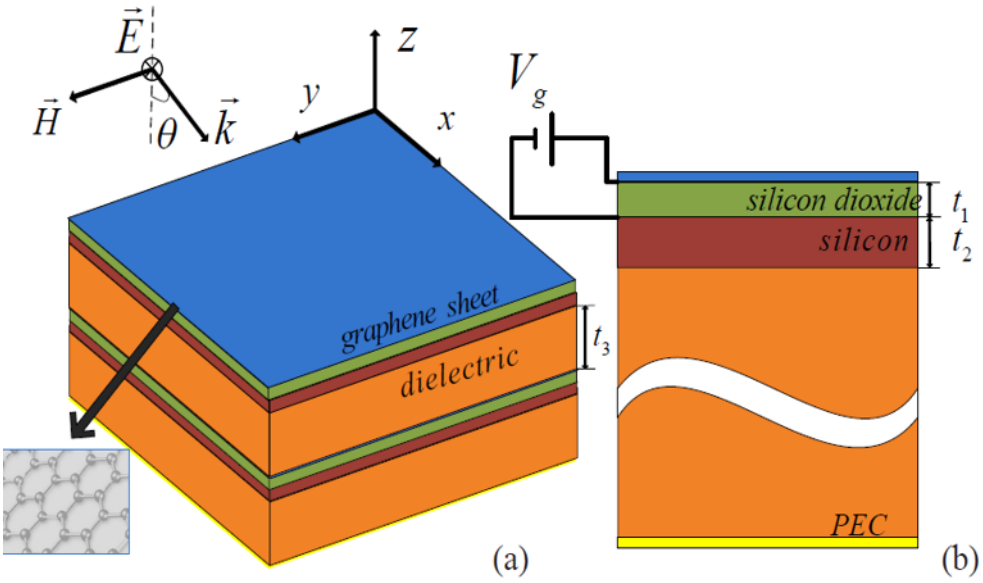

Figure 3.8: Structure separated by dielectric slab a) 3D View b) Cross section view [202].

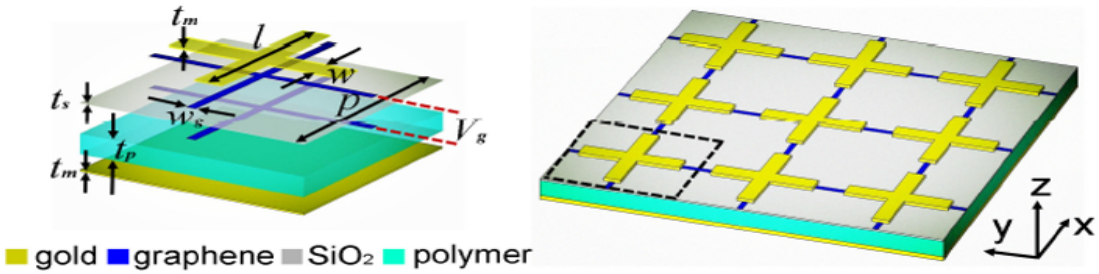

Figure 3.9: Structure designed with unit cell using with Graphene [209].

range of up to 15% and can achieve near-perfect peak absorption without any degradation. By integrating two polarization-dependent MA structures, we also suggested a polarization modulation system by EM wave reflection based on the MA that may vary its reflectance by spectrum shifting of its resonances. It is shown that the polarization modulator may produce linearly polarized waves in reflection with polarization azimuth angles that are continuously adjustable from 0^0 to 90^0 at a fixed operating frequency [209].

The absorption occurs due to multi-path reflection, which results in complete destructive interference in the EM wave's reflective component [210]. Many

techniques are used to improve the bandwidth of absorbers. In [211], vanadium dioxide is used to improve the bandwidth of the metamaterial, but due to its multilayer structure, it is complicated. The combination of Graphene, SiO_2 and gold-based double ring metamaterial structure is offered in [212], but this structure achieves only 36% bandwidth. The next metamaterial is a combination of the above two designs, i.e., vanadium dioxide used as the bottom layer, SiO_2 substrate and rectangular Graphene double ring on top [213]. All the above metamaterial combinations are used to improve the bandwidth, but they do not achieve more than 48%.

In this chapter, an effort has been made to design a monolayer broadband metamaterial absorber. The unit cell structure contains a circular Graphene ring on the top layer, the middle layer is SiO_2 and the bottom layer is gold. This circular Graphene ring metamaterial provides a bandwidth of 67% and is polarization insensitive for TE and TM waves, both EM waves with an incident angle up to 60^0.The metamaterial absorber is an array of unit cells. The unit cell of the proposed absorber is designed with three layers of different materials as shown in Fig. 3.10. The top layer is a circular Graphene ring, the middle layer is a substrate, and the bottom layer is gold. The substrate used in this design is amorphous SiO_2 with dielectric constant 2.25 and loss tangent 0.001. The substrate height is h_S, and the bottom metal gold height is h_G. The absorber is a periodic structurewith a periodicity of unit cell metamaterial is p. The proposed circular Graphene ring inner radius and outer radiusare rin and rout respectively. The circular Graphene ring thickness is t_G, the chemical potential is μ_c, the relaxation time τ_s , and the temperature is 300K. The bottom layer of gold has a conductivity of 4.56×10^7 S/m and the thickness of h_G. The dimenstions values of these symbols are tabulated in Table I. The absorptivity, $A(\omega)$ of the proposed metamaterial is given by [213]

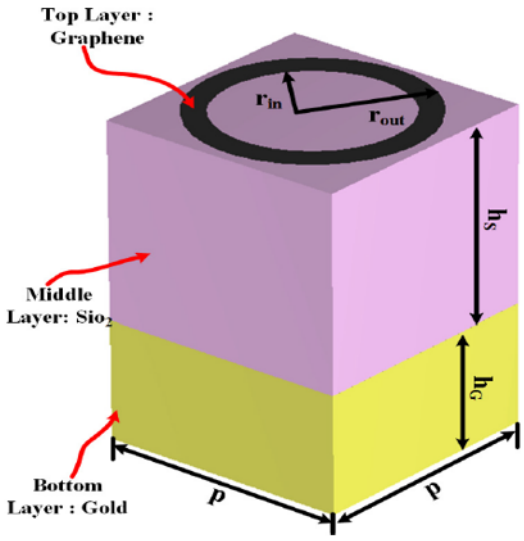

Figure 3.10: Proposed Unit cell structure using Graphene Ring Metamaterial.

$$A(\omega) = 1 - [R^2(\omega)] - [T^2(\omega)] \tag{3.12}$$

Where $R(\omega)$ is the reflection coefficient (i.e S11) and $T(\omega)$ is the transmission coefficient ((i.e. S21). These S-parameters can be extracted from the EM simulator CST Microwave Studio. The metamaterial structure contains gold in bottom, which has a thickness much thicker than the skin depth of the incident terahertz wave. Due to this, transmission can become zero. Because of this, the Eq. 3.12 is written as:

$$A(\omega) = 1 - [R^2(\omega)] \tag{3.13}$$

The structure designed with three layers, these three layers depending on the dimensions bottom layer used gold layer and its having width, breadth parameters $p = 20\mu m$, height $h_G = 1\mu m$ and middle one used silicon dioxide layer and it have height $h_s = 26\mu m$, top of the layer used Graphene material here using inner radius and outer radius $r_{in} = 7\mu m$and $r_{out} = 9\mu m$ and Graphene thickness $t_G = 0.1\mu m$.

The Graphene properties is anisotropic. To find the surface conductivity of Graphene, Dyadic Green's functionboundary condition is used [214]. In the EM simulator, a 2-D Graphene is specified as an impedance boundary, and itssurface conductivity is provided by the generalized Kubo's formula [215].

$$\sigma = \sigma_{\text{inter}} + \sigma_{\text{intra}} \tag{3.14}$$

$$\sigma_{\text{intra}} = \frac{2k_B T_e^2}{\pi\hbar_p} \ln\left[\frac{2\cosh\left(\frac{E}{2k_B T}\right)}{\omega + iR}\right] \tag{3.15}$$

$$\sigma_{\text{inter}} = \frac{e^2}{\pi\hbar_p}\left[H\left(\frac{\omega}{2}\right) + \frac{i4\omega}{\pi}\int_0^\infty \frac{H(\Omega) - H\left(\frac{\omega}{2}\right)}{\omega^2 - 4\Omega^2} d\Omega\right] \tag{3.16}$$

Where,

$$H(\Omega) = \frac{\sinh\left(\frac{\hbar_p \Omega}{k_B T}\right)}{\cosh\left(\frac{\hbar_p}{k_B T}\right) + \cosh\left(\frac{E}{k_B T}\right)} \tag{3.17}$$

'E' is electron charge density and T=300 K. The scattering rate R is inverse of electron scattering time of Graphene and it can vary from 0.02ps to 2ps. In the above equation h_p is plancks constant and K_{bol} Boltzman constant.

The scattering time is defined as collision time of electron in material. By tuning the scattering time of Graphene conductivity of Graphene can tune. Thus, for increasing the conductivity, settling time should be increase. In the terahertz frequency region, Drude's model can used for calculation of the surface conductivity of Graphene and it is given by [216].

$$\sigma_{\text{sc}}(\omega) = \frac{e^2 E}{\pi\hbar_p}\frac{i}{\omega + iR} \tag{3.18}$$

The proposed metamaterial is based on circular ring made of Graphene 2-D material whose properties are tunedusing the Graphene material's chemical potential and relaxation time. The surface conductivity of the Graphenecan be

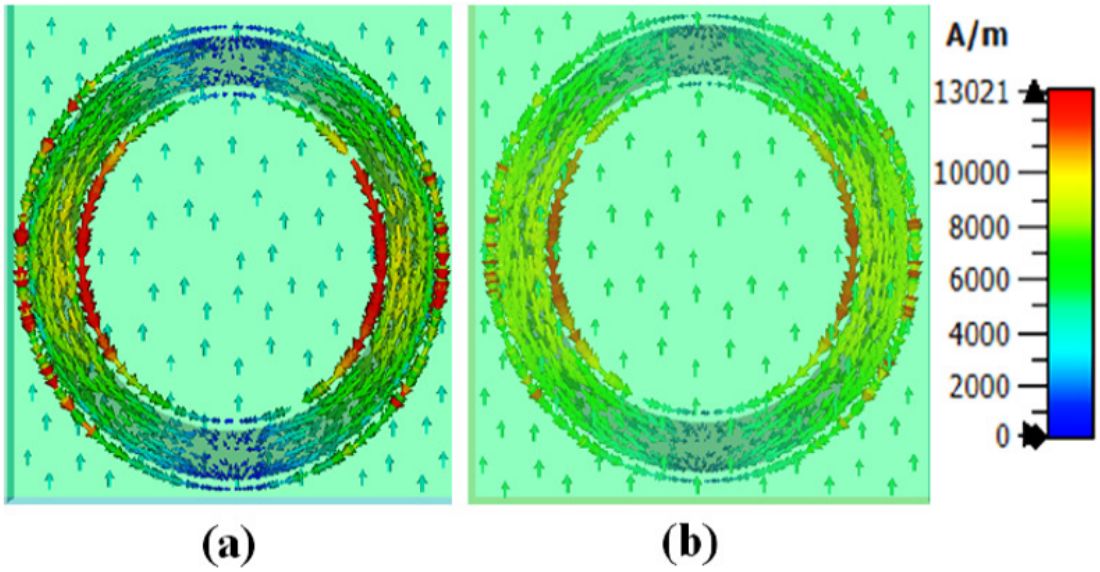

Figure 3.11: Surface current of Metamaterial at 1.3THz (a) Top view (b) bottom view.

tuned by tuning the chemical potential. The Graphene ring impedance depends upon surface conductivity. Torealize broadband absorption surface conductivity should tuned.

The absorber absorption properties can be examined by surface current of the structure. The top and bottom coupling of surface current can be change the absorption of structure. However, the electric and magnetic excitation of proposed circular Graphene ring validated by surface current distribution. The surface current top and bottom of proposed structure at 1.3 THz frequency is shown in Fig.3.5. Here from top and bottom view structure is showing in antiparallel direction. Similarly the top and bottom surface current of at 1.8 THz frequency shown in Fig. 3 is represented antiparallel. This means at this frequency magnetic excitationare realized. But the top and bottom surface current of structure at frequency 2.7 THz shown in Fig. 3.11 are parallel to each other. This indicated electric excitation at this frequency.

The surface current of the structure can examine the absorber absorption properties. The top and bottom coupling of surface current can change the struc-

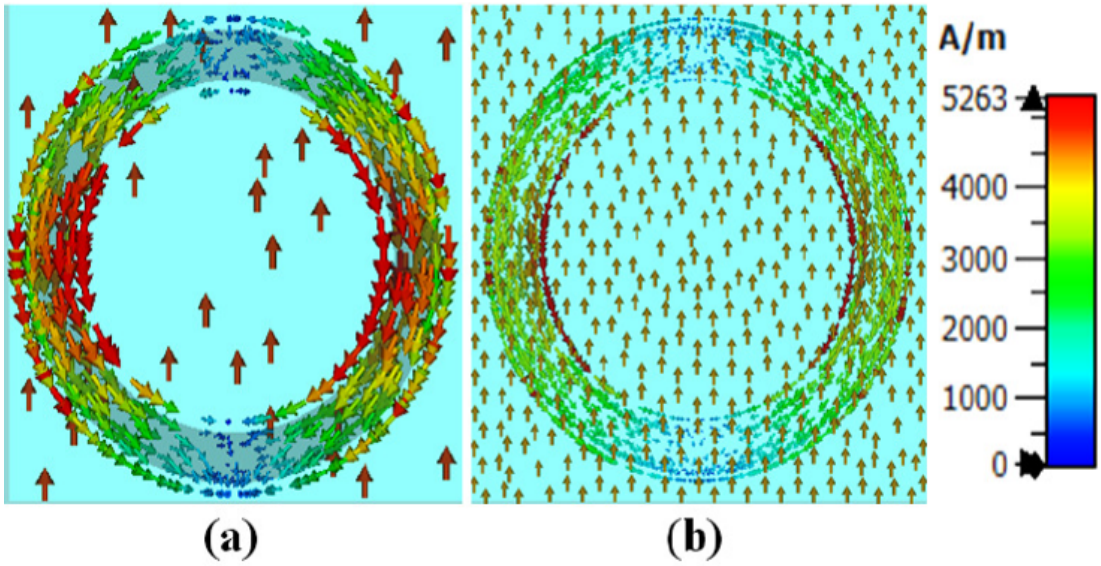

Figure 3.12: Surface current of Metamaterial at 1.8THz (a) Top view (b) bottom view.

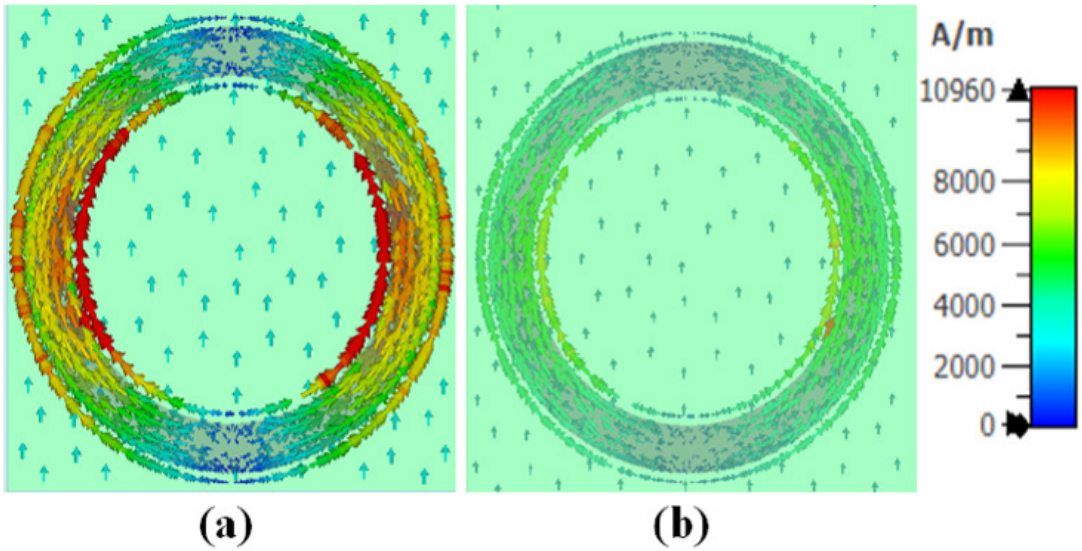

Figure 3.13: Surface current of Metamaterial at 2.7THz (a) Top view (b) bottom view.

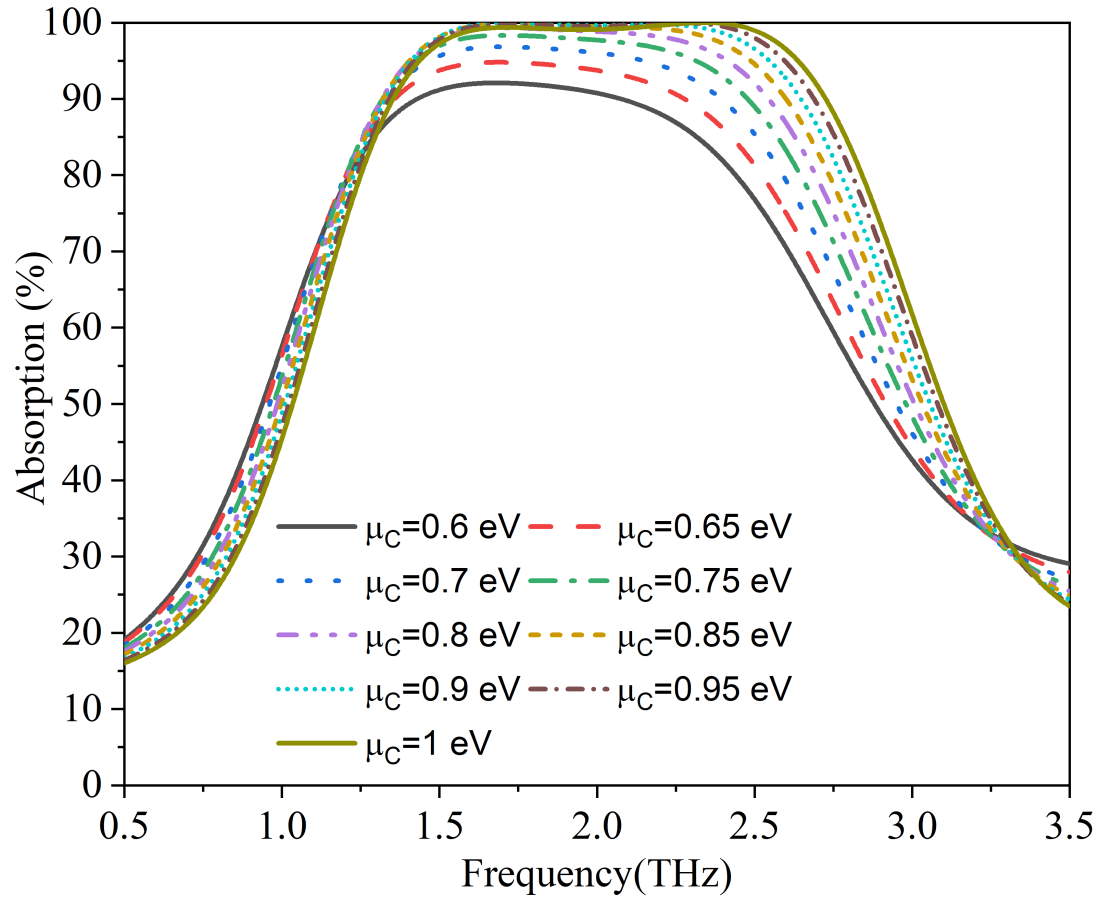

Figure 3.14: Absorption variation of Metamaterial w.r. t chemical potential.

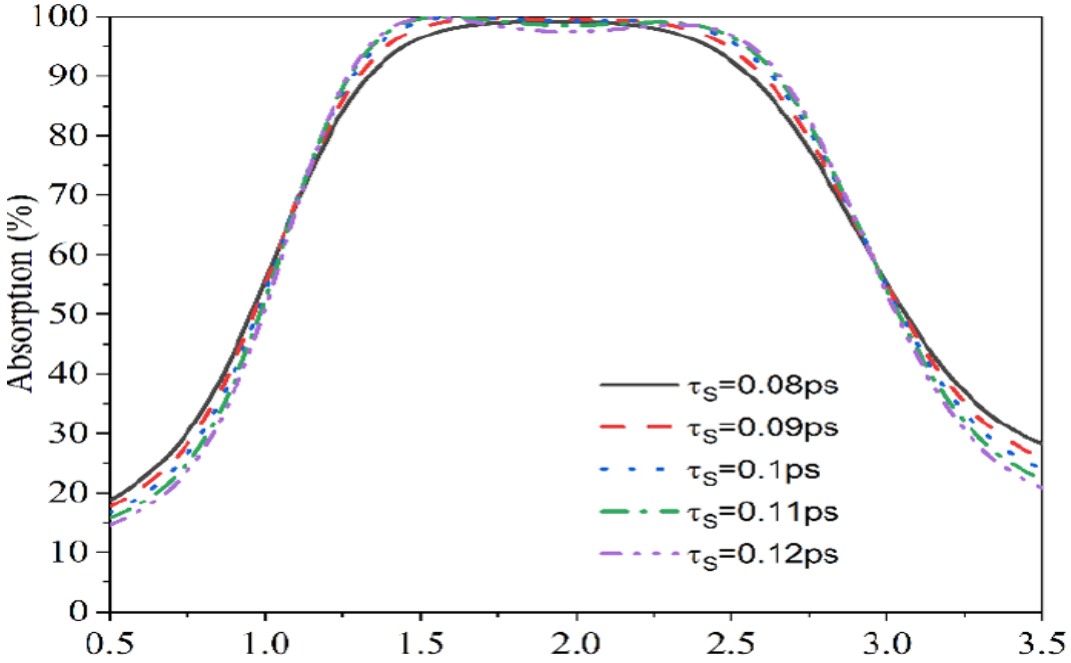

Figure 3.15: Absorption Variation of Metamaterial w.r.t relaxation time.

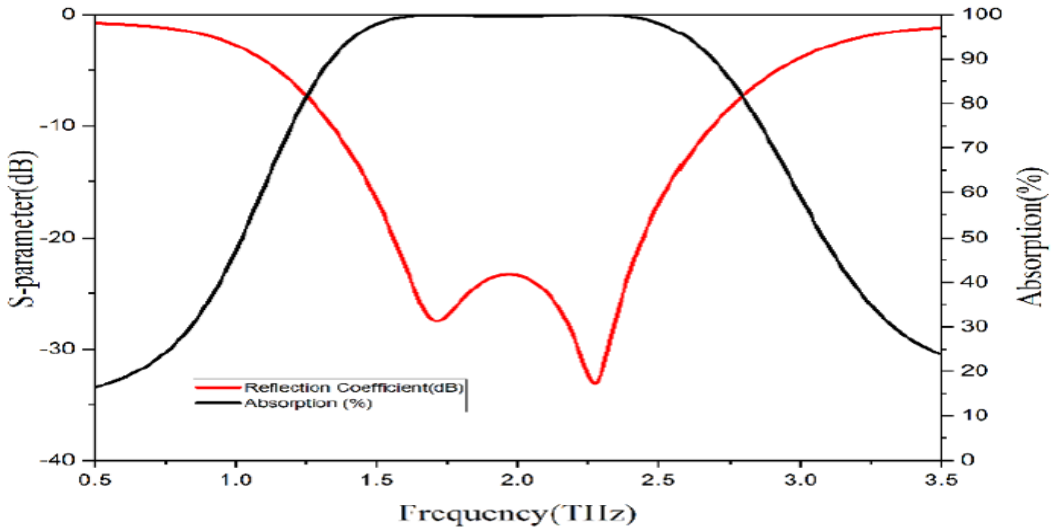

Figure 3.16: Simulated optimized value of S- parameters and absorption.

ture's absorption. However, the electric and magnetic excitation of the proposed circular Graphene ring is validated by surface current distribution. The surface current top and bottom of the proposed structure at 1.3 THz frequency is shown in Fig. 3.12. Here, from top and bottom view, the structure is shown in an antiparallel direction. Similarly, the top and bottom surface current of at 1.8 THz frequency shown in Fig. 3.13 is represented as antiparallel. This means at this frequency magnetic excitationare realized. But the top and bottom surface current of structure at frequency 2.7 THz shown in Fig. 3.13 are parallel to each other. This indicated electric excitation at this frequency.

3.5 Simulation Results

The broadband circular Graphene ring metamaterial is proposed in this work. The Graphene parameters are optimized using parametric simulation. The main chemical potential and relaxation time of Graphene metamaterials affect the absorption. The chemical potential of Graphene can affect the absorption of unit cell structure.The parametric optimization of chemical potential is shown in Fig.

Table 3.2: Comparison between Available Literature

Ref	Material	Fractional Bandwidth >90%	Fractional Bandwidth >99%
[211]	Au+ Polyimide Vo2+ Substrate	25%	0%
[212]	Graphene+SiO_2+Au	36%	3%
[213]	Graphene+SiO_2+Au	48%	9%
In this chapter	Graphene+SiO_2+Au	67%	46%

3.14. The study of chemical potential change of Graphene from 0.6-1 eV showed that the absorber bandwidth changes from 1.3 THz to 2.3 THz above the 80% absorption. The optimized value of chemical potential is 0.95 eV. The relaxation time versus absorption plot is shown in Fig. 3.14. In this study the chemical potential is fixed at above optimized value and relaxation time is change from0.08ps to 0.12ps. The optimized value realized of relaxation time is at 0.1ps. The finalized values of all parameters provide broadband absorption and good impedance matching as shown in Fig. 3.15. These values of Graphene properties provide bandwidth of 1.34-2.7 THz for absorption of more than 90% and bandwidth of 1.54-2.45 THz with absorption greater than 99%.

The proposed work is compared to the available literature tabulated in Table 3.2. The absorption more significant than 90% and 98% of the designed metamaterial has the highest.

3.6 Summary

This chapter introduces a Graphene-based broadband metamaterial absorber. Graphene, consisting of a single layer of carbon atoms arranged in a hexagonal lattice, possesses remarkable electrical, optical, and thermal properties. With applications spanning from cloaking to nonlinear optical devices, Graphene's excellent conductivity has enabled advancements in various fields. While prior attempts at broadband structures have yielded complex results with imperfect absorption,

this study addresses such challenges. While a combination of Graphene, SiO_2, and gold achieved just 36% bandwidth, and many methods struggled to surpass 46%, this study proposes a novel solution using a circular Graphene ring to enhance bandwidth. The resulting structure achieves impressive absorption levels, with a bandwidth of 67% for absorption exceeding 90%, and 46% for absorption surpassing 98%. This design's polarization insensitivity and wide incident angle range further solidify its value in electromagnetic wave applications.

4

Dual-Band Terahertz Metamaterial Absorber: Enhancing Sensing Applications

Contents

4.1 Introduction

Metamaterials are electromagnetic materials crafted by organizing metallic particles in periodic patterns, each lesser than the wavelength of incident electromagnetic waves. These materials showcase a range of distinct attributes, including phenomena such as backward propagation, the Doppler effect, and the Vavilov-Cerenkov effect [217], as well as negative refraction [44, 46], imaging [7, 218–220], and cloaking [8, 221, 222]. Surprisingly, these exceptional properties of metamaterials stem primarily from their structural geometry rather than their composition [223]. Pioneered by Pendry's theoretical insights and further substantiated by Smith et al.'s experiments, metamaterials are harnessed across diverse domains, engaging microwave engineers and physicists alike. Their applications extend broadly, from superlenses [224], slow light manipulation [225–227], and data storage [228] to optical switching [229]. Metamaterials traverse a broad frequency spectrum, spanning near, mid, and far-infrared commands and extending to optical frequencies [11, 230, 231].

Moreover, metamaterials offer the distinctive capability of localizing and intensifying electromagnetic fields, a characteristic that lends itself to detecting minuscule analyte quantities and enhancing sensor selectivity for nonlinear compounds [232]. This intriguing property has spurred the development of novel applications harnessing metamaterial attributes. Plasmon resonance sensors incorporating metallic components on surfaces have been proposed to enhance sensing efficacy [233], catering to high-frequency sensor requirements [23]. He et al. explored the potential of 2D sub-wavelength resonators for biosensing applications [234], while Alu et al. delved into dielectric sensing utilizing ε near-zero thin waveguide channels [235]. Leveraging metamaterial lenses, Schreiber et al. introduced a microwave nondestructive evaluation sensor capable of identifying flaws as minute as a wavelength [236]. In his analysis of future metamaterial

trends, Zheludev emphasized the expanding realm of sensor applications, noting metamaterials' potential to significantly elevate sensitivity and resolution [237]. Research by Huang et al. further corroborates this notion, demonstrating that metamaterials can notably augment the performance of sensors, offering enhanced degree of freedom in sensor strategy to amplify sensitivity and streamline readout [238].

In light of the remarkable progress in THz metamaterial research over the past decade, we classify the applications of THz metamaterial-based sensing into three distinct categories: molecule sensing, biomolecule sensing, and biosensors, as well as microfluidic sensor applications. We delve into the evolution and challenges associated with THz metamaterial sensing, encompassing diverse aspects such as the innovation of novel metamaterial designs, the integration of nanometamaterials in sensing paradigms, the emergence of graphene plasmonic, the fabrication of graphene metamaterial devices, and the intriguing concept of inducing THz surface plasmons through topological insulators.

4.1.1 The Mechanism of THz metamaterial sensing

Surface plasmon polaritons (SPPs), commonly observed in the visible spectrum for metals like gold and silver, face challenges in the THz domain due to the significant differences in physical properties. The high conductivity of these metals, appropriate for the visible spectrum, resembles that of a perfect electric conductor in the THz frequency range, where the frequency is much lower than the plasma frequency of metals (PEC) [239]. Consequently, the electric field of SPPs lacks effective confinement, barely penetrating the metal and losing its advantages. However, employing metals with rough surfaces can facilitate deeper penetration of the electric field into the metal, aiding in overcoming the weak penetration of THz waves. This enables these artificial metal exteriors to support SPP-like styles, serving as examples of metamaterials.

In the realm of metamaterials, various types exist, including dielectric metamaterials, multilayered metamaterial devices (MMDs), metasurfaces, metamaterial absorbers, and graphene-based metamaterials. Metasurfaces, metamaterial absorbers, and MMDs are frequently employed for THz sensing applications. In this context, we direct our attention to the sensing mechanisms underlying these metamaterials, specifically focusing on metamaterial-based thin film sensing, with further details provided in Table 4.1.

Table 4.1: A performance comparison table of metamaterial sensors and the current methods.

Technique	Sensitivity	Other benefits	Confines
THz metamaterials	High	Fruitful structure desing, quick discovery	Complex fabrication process
SPR	High	real time discovery, Labe-free	Device high cost
Colorimetric	Low	real time discovery, Easy to prepare	Sample Interference
Fluorescent	High	Easy operation, rapid detection	Photobleaching

4.1.2 THz metasurfaces

As depicted in Fig. 4.1(a), one can conveniently produce metasurfaces by employing lithography and nanoprinting methods to compose a single or a few layers of planar structures. Their ultrathin profiles minimize losses from resonant responses and metallic structures, and their dimensions are much lesser than the incident wavelength, preventing them from forming a novel material or medium. The continuity of field components governs the reflection and transmission characteristics at the boundary between two homogeneous media. Introducing periodic subwavelength resonators with insignificant thickness at the interface to create a metasurface significantly alters the reflection and transmission coefficients due to the impact on the boundary condition. Involving both charge oscillations within the resonators and the incident electromagnetic wave, a surface electromagnetic wave, akin to surface plasmons forms and propagates along the resonator's surface. Within the THz spectrum, spoof surface plasmons elucidate metamaterial

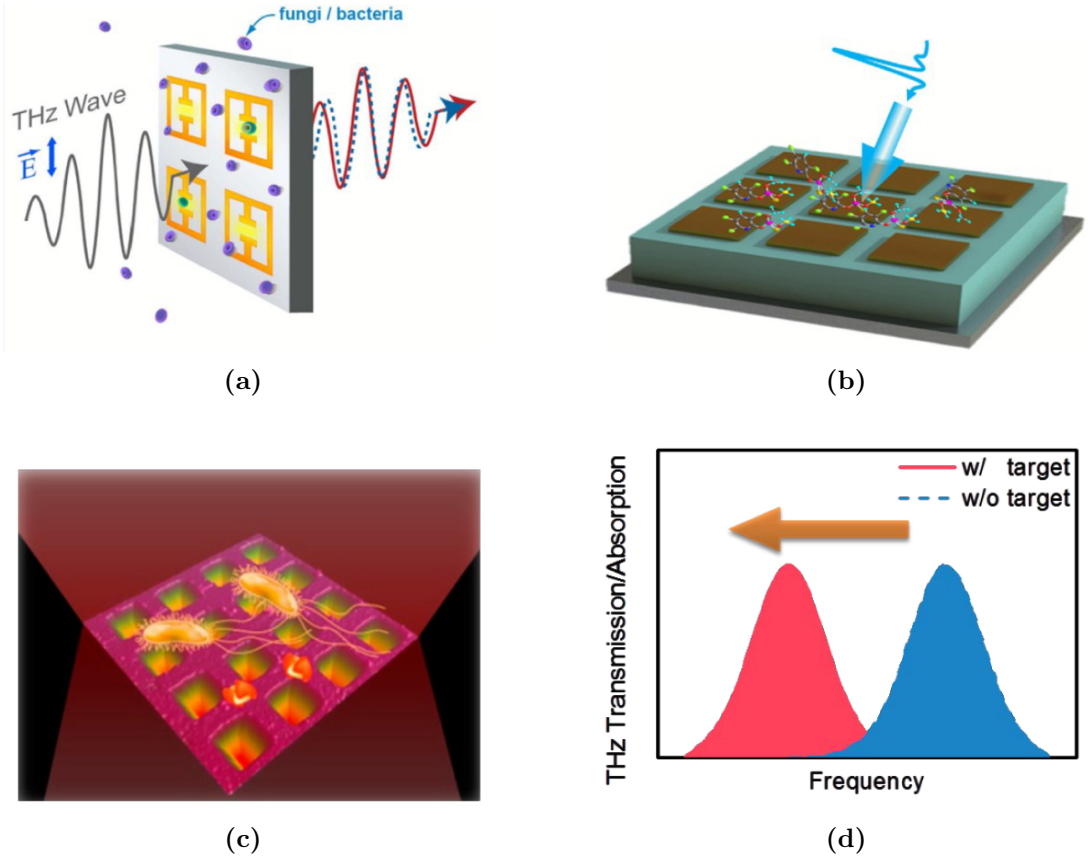

Figure 4.1: Conservative metamaterial sensing [240]. (a) metasurface, (b) metamaterial absorber, (c) metallic mesh device (MMD), (d) red shift of resonant peak induced by external sensing objectives.

mechanisms. With even slight environmental changes triggering shifts in resonant peaks, with resonant frequency and Q worth, THz metasurfaces' local electric field enhancement enables the susceptible detection of external targets.

4.1.3 THz Metamaterial Absorber

The metamaterial absorber was firstly designed in 2008 with dielectric film [22]. One of the most important uses is the demonstration of metamaterial absorbers, which takes advantage of the often-over looked loss mechanisms of optical numbers that may be modified to produce an efficient absorber. The effective

medium and impendence of metamaterial absorber defined as:

$$Z(\omega) = \sqrt{\frac{\mu(\omega)}{\varepsilon(\omega)}} \tag{4.1}$$

When effective impendence matches free space impendence Z_0, then reflection minimized. Then it acts as perfect absorber in particular frequency [210].

Creating a new metamaterial structure allows for adjusting the frequency of the near unity absorption highest. In impedance-matching metamaterial absorber, there is a notable enhancement in the localized magnetic and electric resonant fields, leading to substantial interaction with external sensing targets. This interaction can be harnessed for ultrasensitive target analysis and biosensing applications, as illustrated in Fig. 4.1(b) [241]. Furthermore, in the terahertz (THz) range, a sensing system based on metamaterial absorbers exhibits significantly greater sensitivity than planar metasurfaces [242]. The heightened sensitivity in metamaterial absorbers primarily arises from the substantial increase in resonant electrica and magnetica fields within the absorber cavity, making it particularly intriguing for sensing requests.

Flexible substitutes are comfortable for unshaped surface and suitable for application in various cases. The THz sensor platform shown in Fig. 4.1 [243] was created for sensing purposes and is based on a highly flexible ultrathin metamaterial absorber.

It achieved a maximum frequency sensitivity of 139 GHz RIU^{-1} (Refractive index unit). The sensor's sensitivity did not significantly increase when the spacer thickness was reduced to 15 m compared to the previously mentioned case (50 m thick spacer), indicating that the resonators' architectural designs were more important for very thin film detection than the spacer's thickness, in a single patterned structure, generating one resonance. To achieve a multiband perfect absorption, multiple metallic patterns are typically necessary. Nevertheless, a

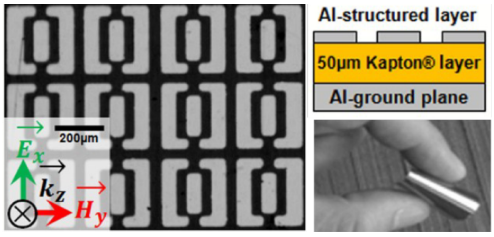

(a)

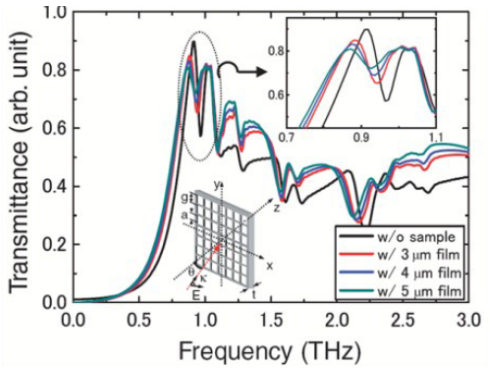

(b)

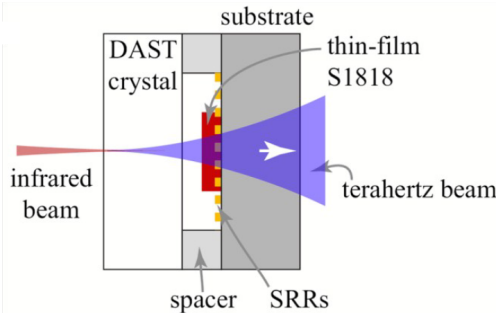

(c)

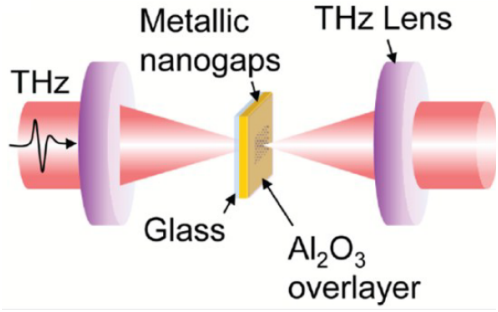

(d)

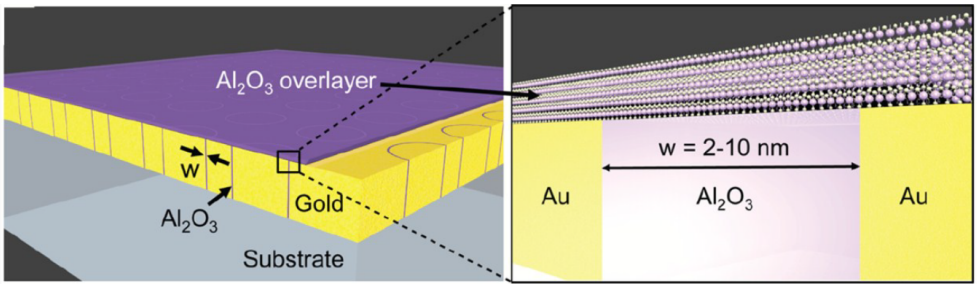

(e)

Figure 4.2: (a) The scanning Electron microscopic (b) dielectric film thick variations (c) a schematic diagram (d)spectroscopy system experimental setup (e) an Al_2O_3 ultrathin layer situated with an annular gap array.

straightforward design featuring an asymmetric cross structure was documented as a tri-band terahertz absorber in a previous study [244]. This design exhibited a maximum sensitivity of upto 1.6THz RIU^{-1} and proved highly responsive to even slight alterations in the external dielectric environment.

4.1.4 THz metallic mesh devices

In Fig. 4.1(c), MMDs are depicted and typically comprise regularly spaced square holes, exhibiting distinctive transmission characteristics. In the terahertz (THz) range, MMDs have shown specific transmission dips resembling Fano-like features, the size of which can be controlled by adjusting the MMD dimensions [245]. These structures can be seen as subwavelength apertures with grid intervals spanning from 10s to 100s of micrometers [246]. The origin of these dips is attributed to the first-order surface plasmon polarisation mode splitting. The Fano-like dip results from the MMDs' structure and the presence of oblique wave incidence, contributing to the creation of a sensitive device characterized by a high Q value resonance. Notably, the frequency shift, often referred to as a redshift, of this dip upon introducing external analyte coatings, as illustrated in Fig. 4.1(d), has garnered significant attention. This feature has made MMDs an appealing choice for label-free biosensing applications, underscoring their versatile sensing modality [247–250].

4.1.5 THz metamaterial-based thin film sensing

Thin film sensing, benefiting from thin films' flatness and predetermined optical properties, presents a straightforward application for THz metamaterials. This approach effectively demonstrates the sensing capabilities of THz metamaterial applications through a combination of simulation and experimentation. A prominent class of THz metamaterial applications is split ring resonators (SRRs). The resonant peak's frequency shift reportedly increases with greater photoresist

thickness atop the metamaterial, albeit slower due to electric field decay above the SRRs' space. Introducing a 16 μm dielectric overlayer resulted in an observable frequency shift of nearly 120 GHz, aligning with simulation results. Moreover, as the SRR thickness increased, the frequency shifted, suggesting a potential avenue for enhancing signals.

The investigation of the impact of the dielectric overlayer thickness on planar terahertz (THz) metamaterials, particularly a double split-ring resonator (SRR) structure, was conducted using THz time-domain spectroscopy (THz-TDS), as described in [251]. Through an analysis of the effects of uniform dielectric overlayers spanning from 100 nm to 16 μm, the challenges and constraints of THz metamaterial-based sensing were illustrated. Notably, an overlayer thickness of 100 nm approaches the detectability limit.

Asymmetric double split rings (aDSR) used in some frequency selective surfaces (FSS) also demonstrated a promising sensitivity [252]. This FSS had a Fano-like resonant peaks due to the addiction of asymmetry. This metasurface proved exceedingly sensitive to external overlayers, exhibiting a remarkable 4GHz frequency change with the addition of a mere 10 nm of material. A dual-band metasurface with low loss properties was designed, featuring high-Q Fano and quadrupole resonances [253]. These resonances offer substantial benefits for ultrasensitive THz metamaterial systems. The analyte was applied to the metamaterial's surface to measure sensitivities, and the two resonances' shifts were quantified as redshifts. The Fano resonance achieved refractive index unit (2.06×10^4) nm RIU^{-1} , high Q-factor compare to quadrupole resonance(5.07×10^3 nm RIU^{-1}). When they were used thinner substrate, it achieves good resonance in quadrupole resonance (7.75×10^3 nm RIU^{-1}), Fano resonance (5.70×10^4 nm RIU^{-1}) [254]. The traditional SRR structure used for delicate to the polarization of incident THz radiation, also Polarization-insensitive metamaterial devices [255], it applicable for Square ring resonator, it specially designed for

linear polarized femtosecond laser driven THz radiation along a negligible determination of 17.7 $\mu molL^{-1}$ for detecting of bovine serum albumin.

Miyamaru and his colleagues [256] employed metal hole arrays (MHA), which are similar to metasurfaces, to investigate the impact of dielectric film sensing. The reflection dip changes due to increases dielectric film thickness at lower frequencies, it applied to high sensitive application.

In the terahertz (THz) sensing domain, a "fishnet structure-based circular hole array was presented as a polarization-insensitive device [257]". Out of the research examined, the frequency change and amplitude inflection concerning the overlayer thickness and refractive index. This investigation demonstrated the sensor's potential to detect changes in refractive index with a sensitivity accomplishment approximately 128 GHz RIU^{-1}. Furthermore, the transmission peak of Metamaterial Hole Arrays (MHAs) was significantly reduced, with the minimum dielectric film thickness set at 50 μm). This reduction posed challenges in measuring the resonant top and lowered the SNR. These issues stemmed from the cutoff result of the metal holes and the incongruity of resonant frequencies on both sides [258].

The use of thickness detection is motivated by metamaterials, which have sensitivity to thin film thickness (The thickness of material $3\mu m$, $4\mu m$, $5\mu m$) as shown in Fig 4.2(b) [259]. The surface of MMD with a tinny film devoted to it was likewise captured in two dimensions, and the contrasts amid photographs of different tinny film widths might too be clearly seen. Similar techniques were used to determine SiO_2 film thickness using MMDs, with sensitivity down to sub-mm-thick SiO_2 films [260].

Introducing Fano resonances to metamaterials led to a remarkable enhancement in the least width resolution of Si, which was increased to 12.5 nm. This resolution represents a scale of 1/16000 times the wavelength of the incoming terahertz (THz) wave [261]. To further advance THz metamaterial sensing, a

near-field THz system was created to diminish the spot extent [262]. This system involved insertion the metasurface sensing stage near a sub-diffraction THz basis. In their study, this proximity was achieved at distances of 25 and 50 m, reducing the quantity of resonators and the negligible sensing film extent. The outcome was a decreased inter-cell link strength and a significantly higher Q factor likened to far-field THz schemes, as depicted in Fig. 4.2(c).

The near-field system exhibited a significantly smaller region for excitation compared to the extent agitated by the far-field method. Only a compact region of 3×3 resonators, equivalent to 0.2λ by 0.2λ (where 0.2λ is the wavelength), could be excited. Combining the near-field source with metamaterial sensing made it possible to increase sensitivity to a 0.2λ 1/375 thick dielectric sheet. This development in THz near-field-based metamaterial discovery held immense promise in biomolecular uncovering, given that it allowed for the excitation of smaller target areas with reduced thickness compared to typical THz far-field systems [263]. In Fig. 4.2(d), the highest level of sensitivity for THz metamaterial-based tinny film discovery touched 1 nm, representing 1/106 of the incident THz wavelength. This study utilized nanogaps to restrain THz surfs into sub-10 nm metallic holes, making it capable of detecting refractive index changes generated by a mere 1 nm thick layer of Al_2O_3, with up to a 5% shift in the top location, as displayed in Fig. 4.2(e). THz plasmonic waveguides were also introduced in THz nanofilm sensing [264].

4.1.6 Utilization of metamaterials in the terahertz frequency range for sensing purposes

THz metamaterial sensing process discussed in the above theory part. THz metamaterial has been used in many fields like molecule sensor, biomolecule sensor, biosensor, microfluidic sensor and other applications.

4.1.6.1 Molecule detection

In 2011, a planar metamaterial expedient using paper as its substrate was developed for glucose discovery, as illustrated in the Fig. 4.3(a) [265]. In this wok, they attained for glucose detection with sensitivity $3.0 mmol L^{-1}$ as shown in the Fig. 4.3(b) generally normal glucose in humanoid blood from $3.0 mmol L^{-1}$ to $30 mmol L^{-1}$, this expedient used for additional purposes. "The paper-based THz metamaterial sensor exhibited promising capabilities and the potential for integration into a lab-on-a-chip device", making paper-based biosensors more affordable and available to average consumers. The use of nano-antennas operating in the THz frequency band (0.5-2.5THz) was reported as a very sensitive and selective sugar detection approach (Fig. 4.3(c)) [266].This metamaterial sensing instrument might successfully increase the molecule absorption due to its tightly localised and increased THz transmission. As illustrated in Fig. 4.3(d) and Fig. 4.3(e) [266, 267], the selective detection at low concentrations was made possible once the transmission top of nano-antennas and the absorption peak of carbohydrate molecules remain coordinated.

The introduction of external D-glucose molecules, characterized by a significant 1.4 THz absorption peak, results in a distinct reduction in the intensity of the 1.4 THz transmission highest. In contrast, sucrose does not produce a comparable damping effect on the transmission peak. This innovative approach has the potential to differentiate between various well-known beverages, such as Pepsi-Cola Classic, Sprite, Coca-Cola Classic, Light, and Zero as shown in (Fig. 4.3(f)).

As the world's population rises from [268–270], two important challenges in global public health-food security and safety are gaining more and more attention.As externally hazardous substances like pesticides and antibiotics leave fingerprints in the THz area, 4–7THz spectroscopy applications for food safety show

significant promise. In recent years, metamaterials have been incorporated into food quality and safety monitoring to further increase the sensitivity of THz detection. In recent years, metamaterials were incorporated into diet security eminence and monitoring to further increase the sensitivity of THz detection [271] (Fig. 4.3(g)). With the use of metasurfaces, extraordinary sensitivity was achieved with the lowest detectable attentiveness downto 100 pg $L-1$ (Fig. 4.3(h)), exhibiting a significant $\sim 10^{10}$ times enhancement in comparison to the lowermost noticeable attentiveness of kanamycin sulfate on bare silicon ($\sim 1 gramme L^{-1}$). Tetracycline hydrochloride (TCH) was quickly detected using a circle-slit metasurface at a nominal noticeable concentration of 0.1 mg L^{-1} [272]. The widespread use of pesticides and the negative impact they have on both social fitness and the atmosphere have led to a global concern. When the herbicide chlorpyrifos-methyl was detected, a THz metamaterial absorber was observed. By contrasting the sensing capabilities of THz metamaterial absorbers and Teflon plates, the sensitivity improvement could be discovered. Based on the metamaterial at THz frequency used in Biomolecule detection with THz frequency and also used in microfluidic applications, it is also used in many applications like nanoparticles, nanorods, nano objects.

4.1.6.2 Metamaterial at THz methodology

The sensing of analytes at THz frequency is an interesting area of research in the present situation. Several methods implemented in research area for analytes detection, it also including absorption spectroscopy, frequency shift, refractive index sensing etc. One of the most sensitive and promising tools for sensing a variety of analytes and their precursors has emerged as the frequency shift sensing techniques [273, 274]. The geometry's design acts crucial level in the terahertz detecting of analytes. Waveguides and metamaterial are important of analytes of sensing [251, 275, 276]. Theuer et al. examined the usage of cylindrical waveg-

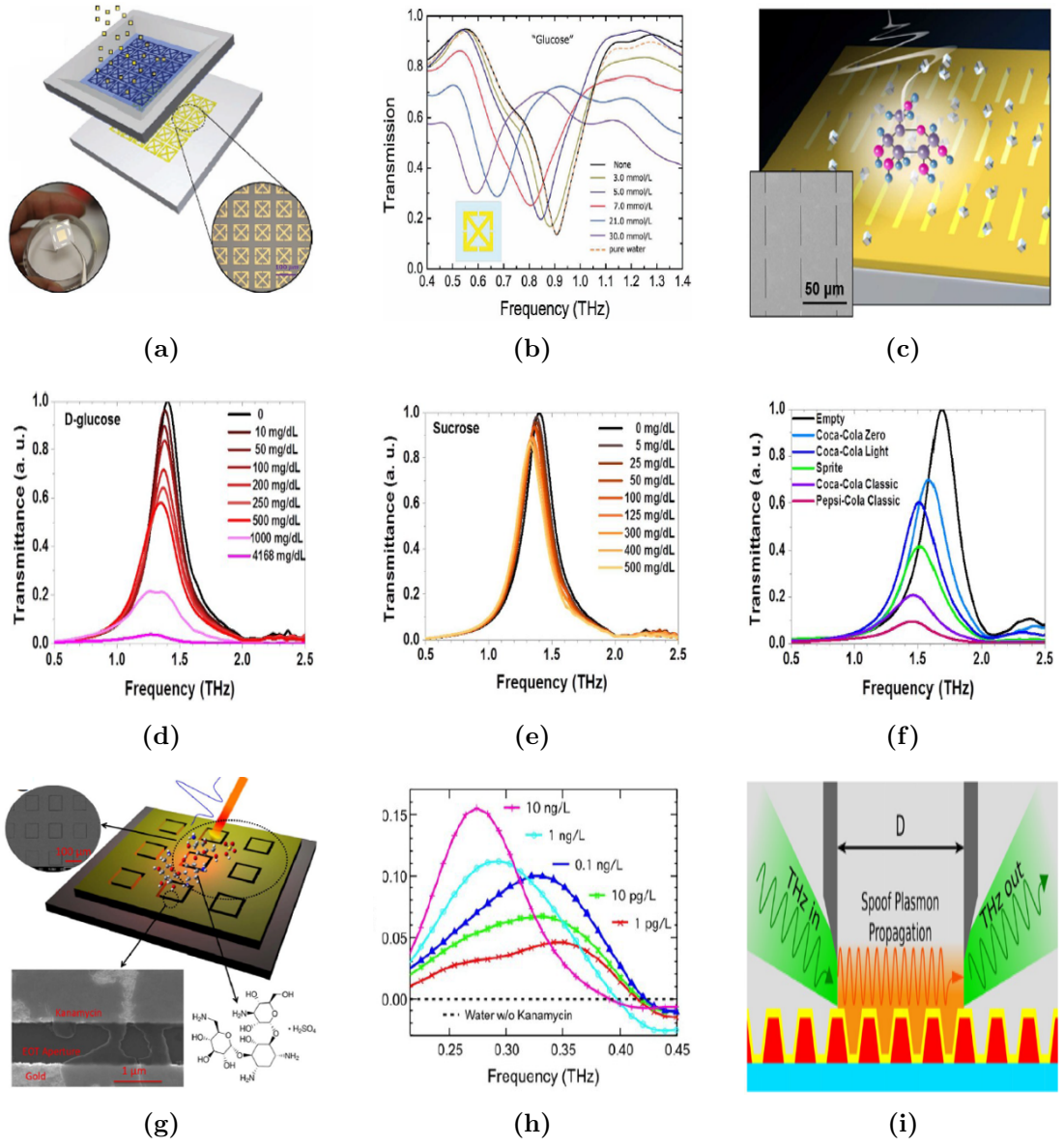

Figure 4.3: (a) Graphic designed with micrometer-sized metamaterial resonators with microstencil. (b)varying concentrations of glucose elucidations. (c)A sensor chip was schematically depicted. (d) Normalized THz spectra for D-glucose were obtained utilizing the glucose antenna, (e) Surface molecules were illustrated in context, (f) THz transmittances were shown by means of a nano-antenna selection featuring a fundamental resonance at1.7 THz, (g) A schematic of the metasurface structure was presented, (h) Changes in transmittance versus frequency were displayed for kanamycin sulfate, (i) A diagram showcased a linear array of sub-wavelength furrows for spoof plasmon sensing, used in guiding THz waves.

uide geometry in the waveguide geometry to explore the detection of analytes with higher sensitivity [277]. We also used nano films sensing using THz range with metal rods [278]. But in this work metal rods detecting phase variations in the surrounding analytes. In that study, the metal rods' evanescent THz fields are employed to detect the phase fluctuations of the nearby analytes. Terahertz spectroscopic transmission studies have been made by Lo et al. on a porous silicon substrate, which is better able to gather and catch analytes in the pores and sense them with increased sensitivity [279]. Various designs employing terahertz metamaterials have been implemented to enhance the sensitivity of analyte detection, making them promising candidates for thin film analyte sensing. In this regard, Singh et al. presented a method for terahertz sensing using high-quality factor resonances in metasurfaces, leading to exceptionally narrow line widths and heightened sensitivity to analytes [254]. Furthermore, in biosensing, Xu et al. introduced the incorporation of gold nanoparticles into terahertz metamaterials to augment the sensitivity of protein detection [280]. Their research highlighted that adding gold nanoparticles with high refractive indices significantly enhanced the detection sensitivity. These developments represent various mechanisms aimed at improving the sensing of analytes.

Metamaterial used in advanced research areas.Novel improved properties of metamaterials can be produced as a result of ongoing development in metamaterial design and production on the submicron and nanoscale scales. Thus, the multidisciplinary boundary between sensing and metamaterial science technology has a become lush ground for novel technical and scientific improvement. Generally metamaterial made up with advanced versions sensor to detect information.

Sensors detect a small modification occur in the device and it's depend upon four key criteria. The first criterion involves ensuring that the sensor operates at a low frequency to mitigate interference arising from background and substrate absorption. Traditional sensing devices, often constrained by limited surface areas,

tend to operate at higher frequencies, which can present significant challenges. Therefore, it is imperative to maintain a compact sensor design while minimizing its operating frequency. The second criterion mandates that sensors generate a distinct and easily detectable read out indication, possessing a resonant characteristic shrill sufficient to precisely way shifts in broadcast bands. The 3rd criterion is centered around the linearity of detecting, which is intricately linked to the superiority factor of devices.

The 4th principle is device compassion, essential for detecting small shifts in transmission spectra caused by external loads, particularly in cases with limited data points in a single-frequency scan. Metamaterial sensors are used in this context to detect a variety of liquids, such as oils, fluids, chemicals, and mixed compositions. These sensors are known for their high-quality factor, remarkable sensitivity, superior accuracy, and a high figure of merit, all contributing to their enhanced performance [281]. Sensing used in various methods to applicable and specially bio sciences area also used and this sensor to detect resonance absorber performance. Here we design two different Perfect metamaterial absorber for sensing application at THz frequency range and also used planar metasurface sensors with resonators of sensitivity and FoM [242] and The importance of biosensing in the THz domain is due to the fact that biomolecules like bovine serum albumin exhibit vibrational resonances in the THz domain [282] and also achieved lower sensitivity and FoM values.

Here we design metamaterial absorber integrated microfluidic sensor, experimentally observed in the THz range. A channel is created between two parallel metal structures that introduce analytes. Within the metal-microstructure array-dielectric-metal (MDM) metamaterial absorber, transverse cavity resonance is observed, as opposed to their detection on the surface of the metamaterial structure, where field distributions are relatively weak and decayed. The channel serves as an MDM metamaterial absorber's spacer as well as a microfluidic channel. Be-

cause of the significantly improved light-matter interaction in the dual-function channel, the sensitivity of the sensors is significantly improved as compared to the standard metamaterial absorber sensors. Furthermore, the deep subwavelength and angle independence of the MPA sensor (metamaterial perfect absorber) are both features. The metamaterial absorber integrated microfluidic sensor also extends to other frequency, explaining a promising method for high-sensitivity chemical and bio-sensors [242].

We focused on this characteristic and reported the sensing performances of odd and even resonance orders within the terahertz (THz) metamaterials framework based on a simple single split-gap ring resonator geometry. We employed a metamaterial design consisting of single split ring resonators to enhance the resonance quality and sensing capability. Our study employed analytes with varying thickness levels and incorporated them into our lossless metamaterial structures. We calculated the refractive index based on thin film variations and measured the sensitivity and Figure of Merit (FoM) for different resonance modes [283].

In metamaterial-based sensor design, several key challenges are encountered, including attaining a high Q-factor, ensuring polarization insensitivity, and maintaining performance independence from varying incident angles [284]. A study by [284] proposed the use of two metal rings in combination with a cylinder to create a dual-band absorption system with a high Q-factor. However, this design was limited to an incident angle of only 30^0. In a different approach, a design employed two rectangular rings and a circle made of silver to achieve a dual-band perfect absorber, providing a high Q-factor [262]. Nevertheless, this structure required three resonators for dual-band operation. Another design focused on bio-sensing applications and utilized a simple cross slot [cite: refb88]. However, the current trend in the field of biomedical research is shifting toward optical sensing [264]. In this context, [264] introduced a microfluidic-based sensor, although it demonstrated a lower Q-factor. An alternative design featured a dual-band

rectangular Complementary Split Ring Resonators (CSRR) based metamaterial. Gold metal enhanced absorption in this mono-layer structure, which operates at two distinct frequency bands: 0.845 THz and 2.12 THz.

4.2 Narrow band Absorber

The structure of a unit cell is presented in Fig. 4.4. The construction has thriple-layer. This construction have dimensions $a = 70\mu m$, $t = 0.4\mu m$ and dielectric material polyamide height $h = 7\mu m$, on the top of dielectric material used two CSRR (Complimentary split ring resonator) rings outer ring have $w1 = 48\mu m$,length $l1 = 64\mu m$, gap of the outer ring $g = 5\mu m$ and inner ring $w2 = 20\mu m$, length $l2 = 32\mu m$ gap of the inner ring is $g = 5\mu m$.

In this structure, a substrate is sandwiched between the bottom and top metal layers. The top-layer comprises metallic Complementary Split Ring Resonators (CSRRs), allowing for dual-band absorbance. The substrate utilized is polyimide thru a dielectric continuous of $\epsilon_r = 3.5$, and a elevation denoted as h. Gold, with a high conductivity of $(4.09 \times 10^7 S/m)$, is employed for both the top and bottom metal layers, with their respective thicknesses represented as t and t_g. The unit cell dimensions are defined as $a \times b$, and the lengths of the CSRRs are denoted as l_1 and l_2. Specific parameter values can be found in Table 4.1. The metamaterial's absorption, $A(\omega)$, is described by the formula from reference [217].

$$A(\omega) = 1 - |R^2(\omega)| - |T^2(\omega)| \tag{4.2}$$

here $R(\omega)$ and $T(\omega)$ represent s_{11} (i.e., the reflection coefficient) and s_{21} (i.e., the transmission coefficient), correspondingly. To compute $A(\omega)$, one requires s_{11} and s_{21}. The simulator named CST Microwave-Studio is used to derive the S-parameters of the structure. Owing to the occurrence of metallic (i.e., gold) in the bottom-layer, it can be stated that $T(\omega) = 0$. As a result, the equation given

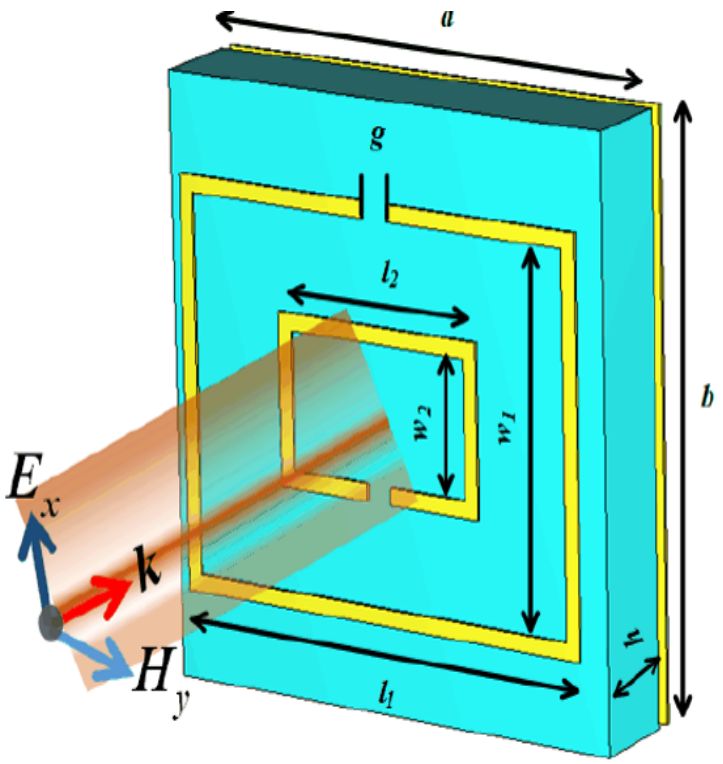

Figure 4.4: Proposed unit call based on CSRR.

above in Eq. 4.2 can be rewritten as:

$$A(\omega) = 1 - |R^2(\omega)| \tag{4.3}$$

4.2.1 Outcomes and Discussions

As a resonator, the planned structure incorporates CSRR. The reflection spectrum, as simulated, is depicted in Fig. 4.5. Notably, the proposed CSRR exhibits resonance at two distinct frequencies, namely 0.846 THz and 2.12 THz, as shown in Fig. 4.6. The absorption spectrum corresponding to these resonances indicates that the structure functions as a perfect absorber, achieving a 98.6% absorption rate at the frequency of 2.12 THz and resonance at 0.846 THz.

The performance analysis of the absorber with varying refractive index is illustrated in Fig. 4.7. To analysis, the refractive index, denoted as 'n,' is adjusted

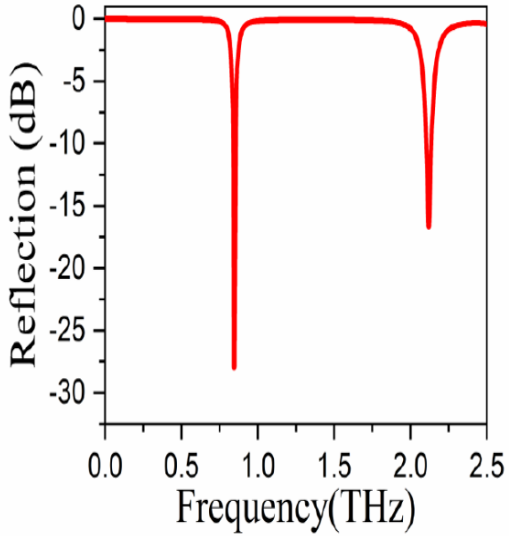

Figure 4.5: Spectrum of Reflection for the CSRR.

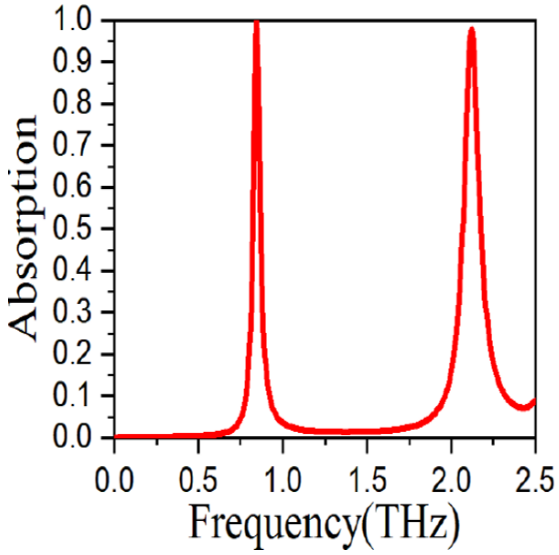

Figure 4.6: Spectrum of Absorption for the Proposed CSRR.

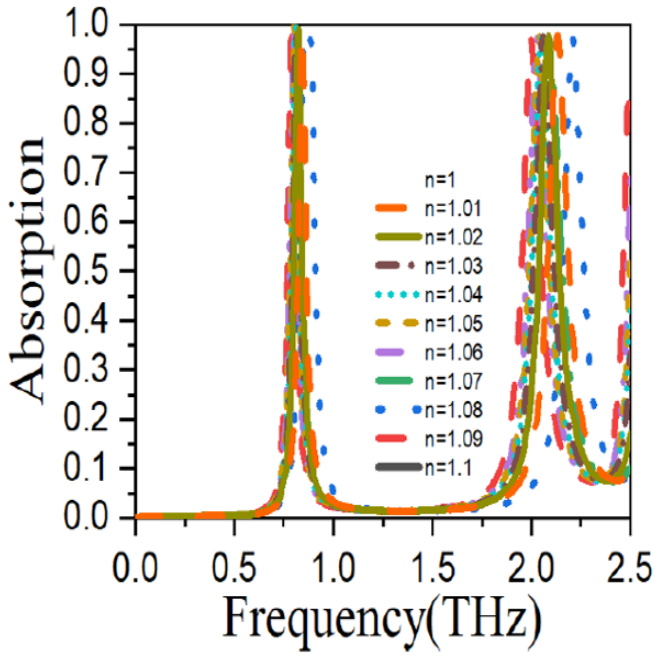

Figure 4.7: Analysis of Absorber Performance with Changing Refractive Index.

within the range of 1 to 1.1 with increments of 0.01. Fig. 4.8 presents the frequency shifts concerning changes in the refractive index. Notably, the upper band experiences a more pronounced frequency shift than the lower-band. The Q-factor of the metamaterials is computed using the formulation referenced in [46].

$$Q = \frac{f_0}{\text{FWHM}} \tag{4.4}$$

In this context, the term 'peak frequency' refers to the frequency at the peak, and 'FWHM' denotes the full width at half maximum. The Q-factor, calculated while varying the refractive index, is presented in Fig. 4.9. The highest Q-factor value, 19.2, is observed at the lower band frequency when the refractive index is n=1.1. For the upper band, a Q-factor of 19.56 is achieved with a refractive index of n=1. The compassion, denoted as 'S,' for the projected design can be determined using the formula provided in [7].

$$S = \frac{\Delta f}{\Delta n} \tag{4.5}$$

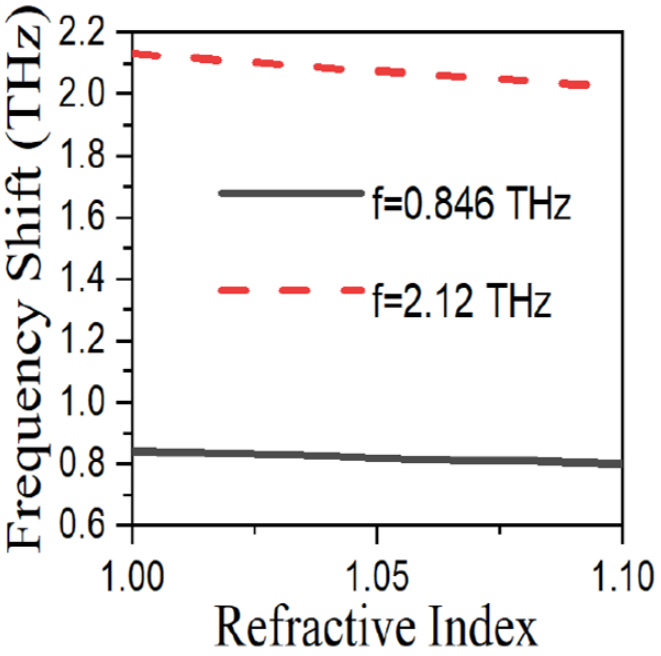

Figure 4.8: Analysis of Frequency Shift with Varying Refractive Index.

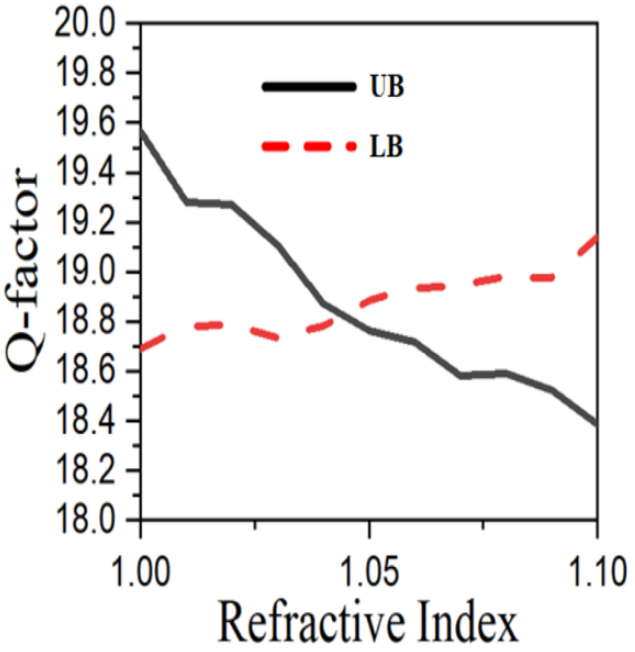

Figure 4.9: Assessment of Q-Factor with Changing Refractive Index.

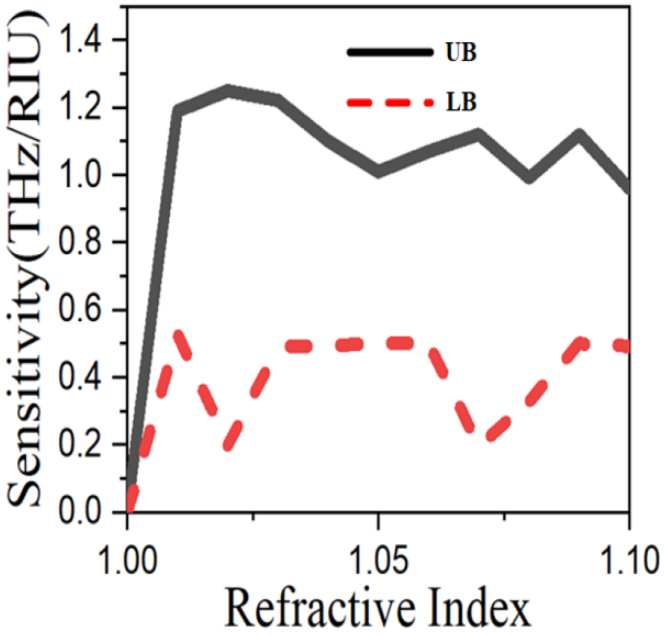

Figure 4.10: Analysis of Sensitivity with Changing Refractive Index.

"In the equation, Δn represents the change in refractive index, and Δf signifies the frequency shift. Fig. 4.10 illustrates the sensitivity plot, demonstrating that the upper band exhibits greater sensitivity than the lower band. In the upper band, the sensitivity varies from 1 THz/RIU to 1.3 THz/RIU concerning changes in the refractive index. Conversely, for the lower band, it ranges from 0.2 THz/RIU to 0.6 THz/RIU. The Figure-of-Merit (FOM) is computed by dividing sensitivity by FWHM. The FOMs of the projected design are determined to be 11.43 RIU^{-1} and 11.79 RIU^{-1} for the Lower Band (LB) and Upper Band (UB), correspondingly. To emphasize the improvement achieved, we compared with existing literature, and the results are presented in Table 4.2. The projected project offers dual-band functionality by high-quality factors, and its FOM is notably more."

In the metamaterial initially designed by using metallic electric ring resonator in 2008. Initially designed for SRR but it can applicable some part of application after that they designed for CSRR(Complimentary Split Ring Resonator).

Table 4.2: Comparative Analysis with Existing Literature.

Method	$FOM(RIU^{-1})$	$Q(THz/RIU)$
7	2.30	11.60
8	4.00	8.57
9	0.85	8.51
10	0.51	7.00
11	0.70	7.80
This Work	11.44 & 11.78	19.20 &19.56

It can be used many applications like thermal index sensing, detection using with narrowband. In metamaterial design, the primary challenges include achieving a high Q-factor, ensuring polarization insensitivity, and maintaining independence from incident angles. Currently, there is a growing trend in designing metamaterials for biomedical applications. A CSRR-based metamaterial is considered, which offers a band absorber. In bottom layers used gold material and top one also, middle ones used polyimide layer . The structure exhibits absorption rates of 100% in the lower band and 98.6% in the upper band. Notably, the upper band demonstrates higher sensitivity compared to the lower band frequencies. The projected design boasts excellence factors of 19.20 THz/RIU for the lower band and 19.56 THz/RIU for the upper band. Furthermore, the Figure of Merit (FOM) for the structure is measured at 11.43 RIU^{-1} for the lower band and 11.79 RIU^{-1} for the upper band.

4.3 Graphene based Absorber Design

Metamaterials have the potential benefit to the sensors by improving their sensitivity, selectivity, and SNR. One of the ways for improving sensor performance is with varying unit cell size and its geometry to get maximizes sensing

property. Metamaterials can be made to have adjustable or tunable resonance characteristics. These characteristics are useful for the sensor to identify the specific frequencies of electromagnetic radiation. The metamaterial (MM) sensors are used in many different applications like medical, agriculture, and industrial, etc. Yusheng Zhang designed a Split Disk Metamaterials (SDM) structure for Gas detection applications. Where the resonance frequency is controlled by adjusting the gaps on the metamaterial. It achieves a maximum sensitivity and figure of merit (FoM) values of 3567 nm/RIU and 20.89 [285]. Ayesha Mohanty designed square shape structure and it achieved Quality factor 225, sensitivity at 1.6 THz/Refractive index unit and Figure of merit (FOM) achieved 80 but it generates very narrow absorption peak [286]. In this structure designed with circle shape and it achieved Q-factor 8.887 RIU^{-1}, 8.163μm^{-1} but it has four band peaks [287]. Zhonggang designed a square shape split ring resonator a Narrow resonance peaks, it achieved absorption, Q-factor, Sensitivity of 99% at 0.53 THz, 44.17, 126.0 GHz/RIU respectively and it depends on the thickness levels of material. It has very narrow peak [36]. This article was designed a square shape split ring resonator structure, it achieved Quality factor 32.167, and FoM 6.015. It's mainly used for biosensor application but it's depend different refractive index media [288]. Hence the reported works suffer from various issues like large variation in tunablity.

The present chapter focuses on a novel approach that combines three distinct layers: an Au bottom layer, silicon dioxide in the middle, and an outer ring of Complementary Split Ring Resonator (CSRR) with a Graphene inner layer. This innovative design leverages the unique properties of graphene to enhance performance and overcome limitations observed in previous designs. By strategically integrating different materials and structures, the aim is to achieve a heightened level of performance and sensitivity in the realm of graphene-based absorber design.

4.3.1 Geometrical Description

In this structure bottom gold layer and middle one layer silicon diode act as dielectric material and top inner ring used Graphene material and outer ring used gold material, entire structure design using CST software FDTD (Finite difference time domain method).when signal passed through the top layer of the material and reached at the dielectric material, it matches impendence passed through dielectric material and its reached bottom gold layer here gold layer block signal, it reflected signal and transmission part was zero, these structure produce two resonance peaks.

$$A = 1 - |S_{11}^2| - |S_{21}^2| \tag{4.6}$$

Here transmission part blocks signal so we get the

$$A = 1 - |S_{11}^2| \tag{4.7}$$

S_{11} = Transmission co-efficient , S_{21} = Reflection co-efficient. This is a three-layer structure, the middle layer is basically a dielectric medium. The thickness of the same was found to be $70\mu m$, height $15\mu m$ with dielectric constant 3 of 0.9. In addition to that this layer also has electrical conductivity and thermal conductivity$10^{-12}s/m$, 1.4W/mk respectively. As we are using graphene in this design and the chemical property of Graphene subjected to change when temperature changes. It is good to consider the refractive index and melting temperature of Sio_2 also asit is part of design and the values are 1.46, $1713 - 2950^0$c.

When we talk about the top layer which is a CSRR structure made up of Graphene and Gold. The inner layer is composed of a Graphene with dimensions Win=$32\mu m$, Lin=$27\mu m$,W2=$5\mu m$, h=0.4, g2= $9.9\mu m$ and the outer layer consists of Gold having Wout=$64\mu m$,Lout=$43\mu m$,h=$0.4\mu m$,g1=$9\mu m$. The absorption rate for the said structure is 92% and 99% respectively.

In the proposed design, the three peaks of 100%, 97% and 76% shows the

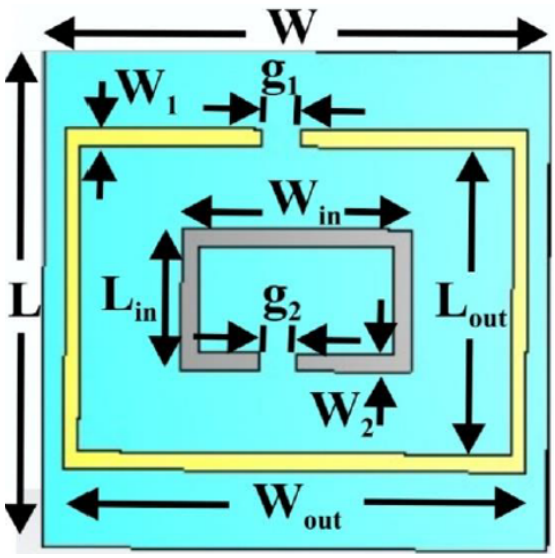

Figure 4.11: Proposed structure.

absorption efficiency applicable for biomedical diagnostics, imaging in security screening, harvesting etc., and fig.3 shows that in reflection of the structure, two peaks narrow, the middle one wider, and Fig. 4 shown that absorption of structure here we achieved triple band peak occurred and based on CSRR design. The carrier density of graphene is defined by its chemical potential. The quantity of charge carriers (electrons or holes) in the material can be changed by varying the chemical potential. Because of their tunability, metamaterials can be created with customised electronic characteristics like conductivity or optical responsiveness. Tunable metamaterials can be made possible by the manipulation of the chemical potential of graphene. When exposed to external stimuli like an electric field or chemical reactions, these materials' characteristics can change. For instance, by adjusting the chemical potential, you can change the plasmonic resonance frequency in graphene-based metamaterials. In Fig. 4.14, for every 0.1ev chemical variation different tunability will occur. In Table 4.3, tunable achievement is compared between available literature and the earlier one.

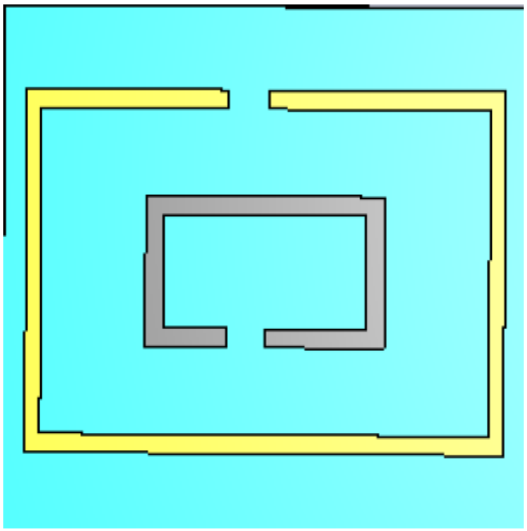

Figure 4.12: Top View.

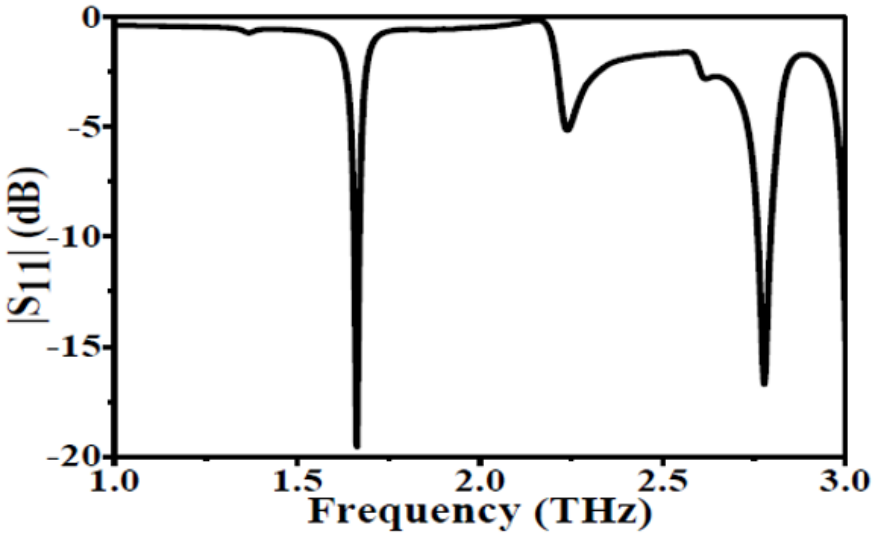

Figure 4.13: Reflections.

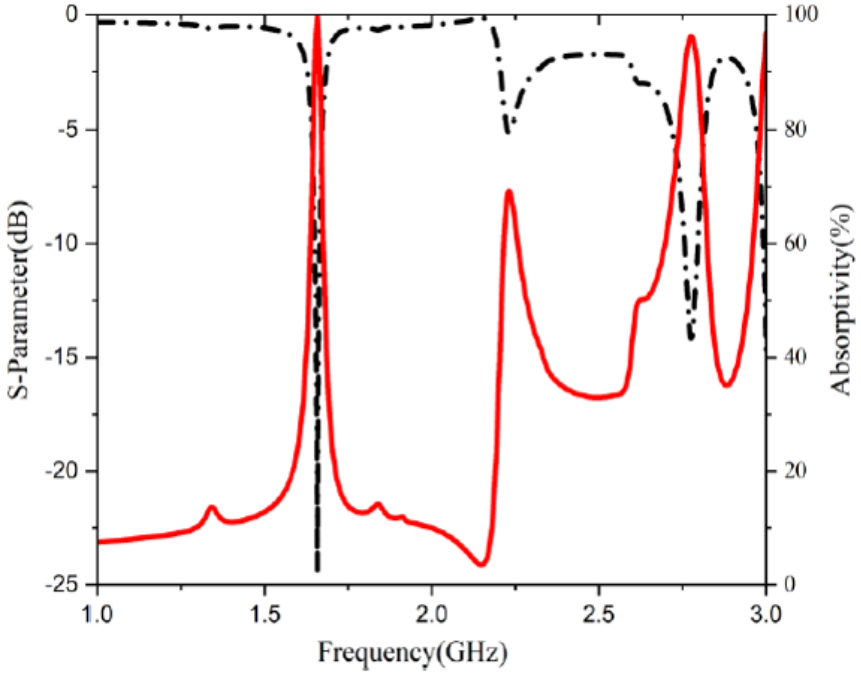

Figure 4.14: Absorption Percentage.

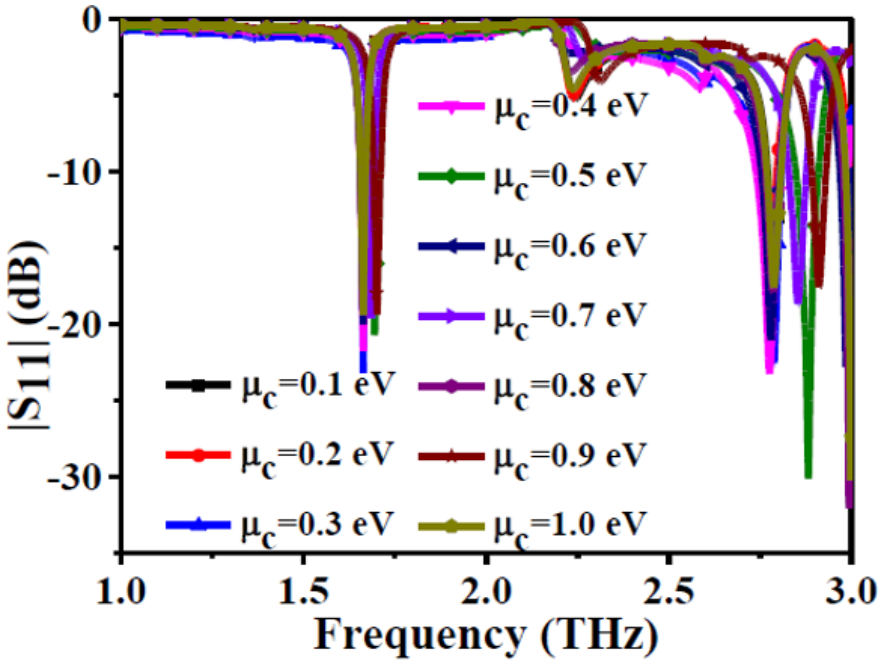

Figure 4.15: Chemical Variations.

Table 4.3: Comparison between available literatures.

Ref	Type of structure	Number of bands	Tunable
1	Split Disk Metamaterial	single band	No
2	Square shape design	single band	No
3	Circle shape designed	four band	No
4	Square shape Split Ring Resonator	Single band	No
Present work	CSRR structure designed	Triple Band	Yes

4.4 Summary

In this chapter, we explored the utilization of a dual-band metamaterial absorber and a graphene-based absorber for sensing applications. The dual-band design employed CSRR with Rectangle Ring shapes, featuring gold and polyimide layers on top, and a gold layer at the bottom. This arrangement resulted in impressive absorption peaks of 100% and 98.6% at 0.846 THz and 2.12 THz, along with Q-factors of 19.2 and 19.56. The Figure of Merit (FOM) values stood at 11.43 RIU^{-1} for the lower band and 11.79 RIU^{-1} for the higher band.

For the graphene-based absorber, we designed a simple structure using a multiband peak generated here we achieved two resonance peaks getting one is higher peak and the other one is lower peak i.e. first peak absorption is 100% and the other peak is 96% and the other one is 70% compare previous result we getting good results.This structure is mainly designed for sensing applications and it generates multiband peaks.This structure can be extended to biomedical applications by further reducing its size which is possible by adding one more SRR structure. Also, the performance can be observed with different materials like Au, etc.

5

An Ultrathin Triple-Band Absorber for Tunable THz Bio-sensing

Contents

5.1 Introduction

Metamaterials, artificially engineered materials with unique properties such as negative refractive index, cloaking, reverse Doppler effect, and more, have emerged as a groundbreaking field of study. These materials also function as perfect absorbers, contributing to developing sensing devices in various applications, including bio-sensing. Metamaterials have found use in detecting phenomena such as glucose levels and pesticides in agriculture, under scoring their versatility. This chapter delves into how biosensors leverage metamaterials to detect various substances. The significance of biosensors spans multiple domains, encompassing biological research, disease diagnosis, environmental monitoring, and food safety assurance. Techniques such as fluorescence-based as says and imaging methodologies have greatly benefited from biosensor integration [289, 290]. However, the need for fluorescent labeling can be costly, time-consuming, and inapplicable in specific contexts. Furthermore, the intricate three-dimensional structure of biomolecules can be altered by fluorescent markers. Consequently, there has been a growing interest in label-free bioanalytical sensing approaches that directly identify target molecules.

With metamaterial-based biosensing technologies gaining momentum across a broad frequency spectrum, from microwaves to optical frequencies, they offer an affordable and label-free means for detecting biomolecules. These technologies are classified into three primary categories based on their operating frequencies and components: microwave biosensors, terahertz biosensors, and plasmonic biosensors. Each category addresses specific sensing requirements, paving the way for innovative and precise detection methodologies.

5.1.1 Microwave biosensor

In the context of microwave biosensing, the utilization of a split-ring resonator (SRR) results in the creation of a material characterized by a negative magnetic permeability (NMPM) when it interacts with a time-varying H-field component of a perpendicularly polarized wave [5, 291]. The unique property that makes SRRs particularly suitable for this purpose is their diminutive electrical size, allowing them to be smaller than the signal wavelength during resonance. This essential feature facilitates the creation of an efficient NMPM. Notably, SRRs are well-suited for miniaturizing planar microwave devices such as filters [292–294] and antennas [295–297].

SRRs have found recent applications in the development of devices and sensors. Lee et al. [298] introduced an SRR-based biosensor through a minute electrical dimension to identify biomolecular binding events. The structure of the biosensor's structure, depicted in Fig. 5.1, consisted of two pairs of SRRs and a planar microwave transmission line. The planar microstrip transmission line generated a time-varying H-field component perpendicular to the surface of the SRRs. Notably, the electromagnetic field was not confined solely within the transmission line; instead, it served as an open conduit for wave propagation.

Additionally, a minor E-field component was present along the axis of the transmission line. Consequently, as illustrated in Fig. 5.1, the mode through which microwaves propagated was a quasi-TEM mode rather than solely a transverse electromagnetic (TEM) mode. Faraday's law dictates that resonance takes place when a time-varying H-field component impacts the surface of the SRR perpendicularly. This behavior arises from the fundamental LC resonant circuit nature of the SRR. The equation governs the resonance frequency (f_0): of $f_0 = \frac{1}{2\pi(LC)^{1/2}}$. Thus, changes in inductance or capacitance induce corresponding alterations in the resonant frequency. This resonant behavior underlies the

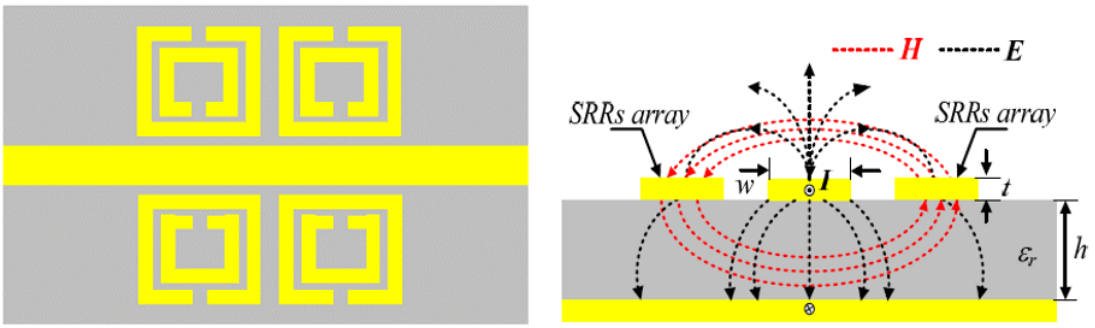

(a) (b)

Figure 5.1: The structure of biosensing based on SRR array: (a) The Top view of a microstrip transmission line and (b) Cross section of a microstrip transmission line with a pair SRRs and a schematic electromagnetic field distribution.

SRR-based biosensor's ability to detect biomolecular binding events.

A biosensor, consisting of a biological sensing component linked to a transducer, detects specific biological interactions. It comprises a transducer or detector, a sensitive biological part, and relevant electronics for signal processing. To investigate sensitivity and selectivity in SRR-based biosensors, we employed single-stranded DNA (ss-DNA) linked to biotin. This ss-DNA-biotin combination adhered to gold (Au) surfaces due to their strong chemical attraction, facilitating thorough exploration of biosensor attributes.

We harnessed the established affinity between biotin and streptavidin after immobilization through a bioprocess. This binding, depicted in Fig. 5.2, amplified sensitivity and selectivity in the biosensor.

The SRR-based biosensor exhibited a resonance frequency of 10.82 GHz without biomaterials. Upon the addition of biotin, the resonant frequency shifted to 10.70 GHz, resulting in a frequency change of $\Delta f_B = 120$ MHz.Further binding of streptavidin and biotin led to a frequency of 10.66 GHz, accompanied by a frequency change of $\Delta f_{B-s} = 40$ MHz.These resonant frequency shifts were driven by capacitance alterations induced by the binding of biotin and streptavidin. Thus, the biosensor based on SRR demonstrated its potential for imme-

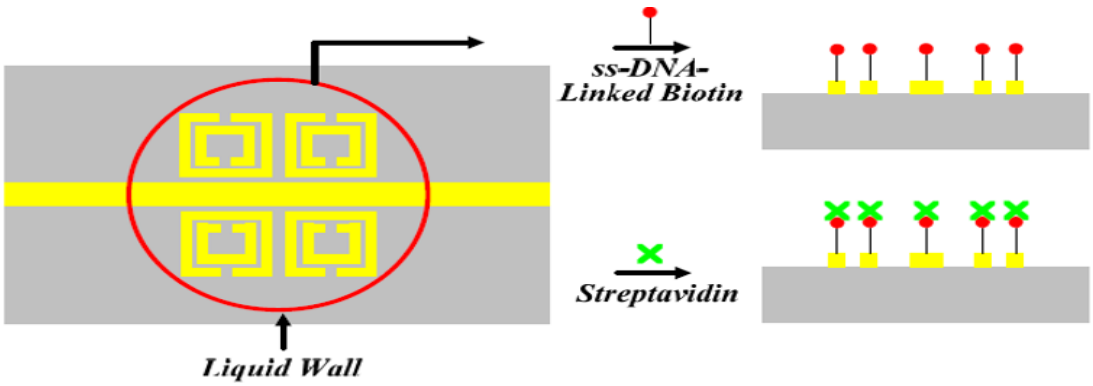

Figure 5.2: Streptavidin and biotin-binding the bioprocess: The container for liquid solution confinement is shown by the liquid wall (red circle). The biotin (red) for 12h rinsed and exposed to streptavidin (green) for 6h.

diate label-free biomolecular recognition. Despite the relatively large occupied regions of the devices and their higher biomolecular concentration $\sim \mu g/mL$, significant resonant frequency shifts were observed in biosensors utilizing the resonator array.

In a study [299], a single planar double split-ring resonator (DSRR) was introduced for microwave-frequency biomolecular recognition, akin to the resonator array-based biosensors. The 50Ω microstrip transmission line induced time-varying magnetic fields that stimulated the small resonator.

The DSRR-based biosensor's resonance frequency is 12.35 GHz without biomolecules, just like the SRR-based biosensor. When ss-DNA was immobilized on an Au surface, the frequency shifted to 12.33 GHz, resulting in a frequency change of $f_{ss-DNA} = 20$ MHz. Subsequently, after ss-DNA and complementary-DNA (c-DNA) hybridization, the resonant frequency decreased further to 12.27 GHz, with a frequency change of $\Delta f_{hybridization} = 60$ MHz. This frequency alteration was attributed to the interaction between two nanometer-sized biomolecules, ss-DNA ($\epsilon_{r1}^{\text{eff}}$) and c-DNA ($\epsilon_{r2}^{\text{eff}}$), each possessing distinct effective permittivities. This interaction induced changes in the capacitance and inductance of the resonator surface, enabling the detection of nanosized proteins using miniature microwave

resonators.

In conclusion, the biosensor operation based on time-varying magnetic fields from the microstrip transmission line primarily hinges on resonant frequency changes resulting from the binding of two different proteins onto LC resonators.

5.1.2 Terahertz biosensor

Terahertz (THz) waves, occupying the frequency spectrum among microwaves and infrared, have exhibited attractive potential for chemical and biological sensing over the last two decades [300]. Leveraging the resonant absorption of molecules or phonon resonances in the terahertz frequency range, these biosensors ascertain a sample's complex dielectric properties to directly discern its chemical or biochemical composition [301, 302]. Detecting dielectric alterations arising from biomolecular binding facilitates unequivocal identification of macromolecules, particularly for large biomolecules where pronounced absorption characteristics are absent. However, the diverse range of applications for terahertz sensing, spanning from foundational research to security contexts, necessitates detecting minute quantities of chemical and biomolecular components. The discrepancy between the sensor's wavelength and the nanoscale dimensions of analyte quantities in real-world applications challenges conventional terahertz spectroscopy systems. Thus, there is a pressing need for adaptable and sensitive solutions to probe the dielectric characteristics of trace chemical or biochemical molecules.

Yoshida et al. [303] recently introduced a label-free sensing technique employing a thin metallic mesh in the terahertz range. This approach capitalizes on modulating terahertz radiation transmittance through the mesh holes when introducing a sample. Remarkably, the thin metallic mesh's transmittance remains unaffected by absorption. Nonetheless, when horseradish peroxidase was deposited at a 500 pg/mm^2 density on the mesh, a distinct shift in the trans-

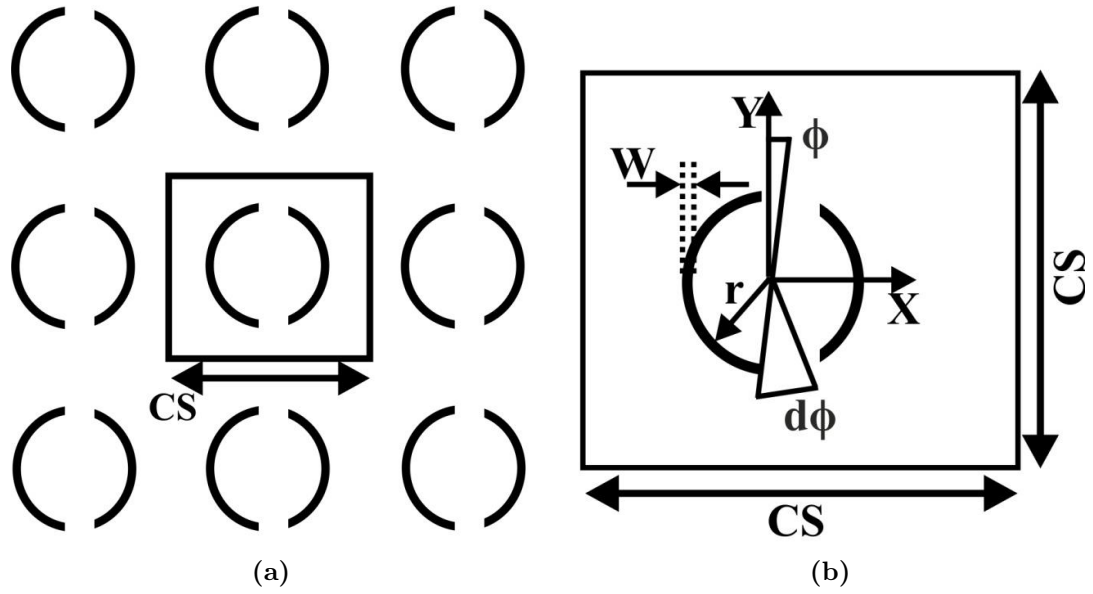

Figure 5.3: (a) Demonstration partition of a DSR-based FSS appropriate a rectangular frame and (b) Unit cell having with gap angle $d\varphi = 20°$, asymmetry angle $\varphi = 4°$, cell size cs=220 μm, width w= 5 μm, and radius r= 50μm [305].

mission dip frequency occurred, attributed to variations in the sample material's refractive index near the holes.

A crucial requisite for the sensor's effectiveness is a pronounced frequency response edge and a region of intense electric field concentration, facilitating heightened sensitivity [304]. Addressing this, Christian et al. [305] introduced a second gap into split rings, breaking symmetry to establish a high-concentration electric field point. This design yielded a metamaterial structure termed the asymmetric split ring resonator (aDSR) terahertz frequency selective surface (FSS), as illustrated in Fig. 5.3. This innovation has the potential to sense minute quantities of both chemical and biochemical substances, offering a promising advancement in terahertz biosensor technology.

The reflection of the terahertz sensor revealed dual critical characteristics after the terahertz biosensor was activated by open space radioactivity, as shown in Fig. 5.4(a). An extensive extreme is seen at 1,090 GHz, where the span of

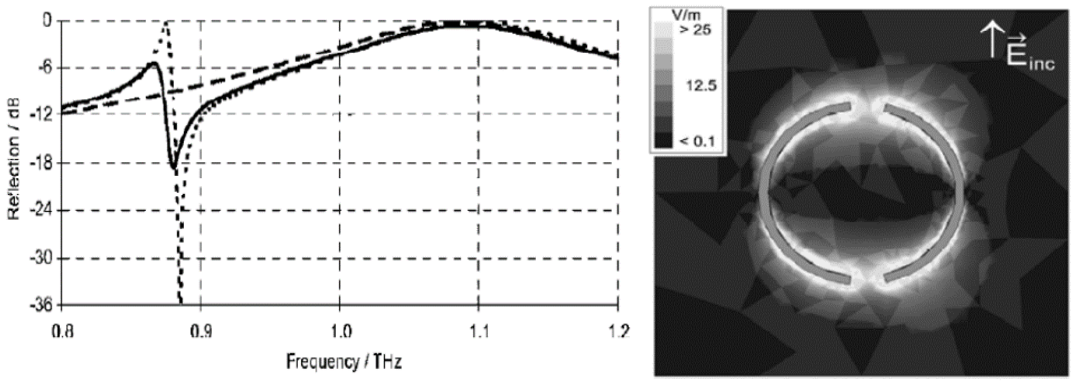

(a) **(b)**

Figure 5.4: (a) FSS reflection in a perfect conductor (dotted line) and in gold (solid line) for symmetric (dashed line) and asymmetric (solid line) DSRs with $varphi = 4°$; (b) The E-field showing resonator plane, a strong concentration (white) at the closing of the arcs. F= 875 GHz, amplitude of excitation 1V/m [305].

each aDSR arc roughly corresponds to half the wavelength. This dipole exhibits antenna-like performance for the symmetric DSR $\varphi = 0°$, and a tiny angle φ has little impact. The length of the two DSR arcs differs as the angle $\varphi > 0°$ is increased. The reflection of this asymmetric case displayed a 13 dB over 13 GHz strong and sharp modulation at around 875 GHz. For an FSS built of gold, a flank with a very high steepness of 7 dB over 4 GHz was maintained outside the 3 dB ranges. Intriguingly, Fig. 5.4(b) illustrates how the electric field concentrated considerably at this steep slope towards the ring with amplitudes 25 times higher than the excitation E_{inc}. As a result, the dielectric loading frequently changed the frequency response of the resonant structures used in high-sensitivity terahertz sensors. The dielectric characteristics of the material used to construct such a structure can immensely affect the frequency shift.

Tao et al.'s recent proposal [306] for a terahertz paper-based metamaterial (MM) device holds promise for quantitative analysis in biological sensing Fig. 5.5. The technique employed photoresist-free shadow mask deposition on paper to craft planar metallic resonators with features under 5 μm.

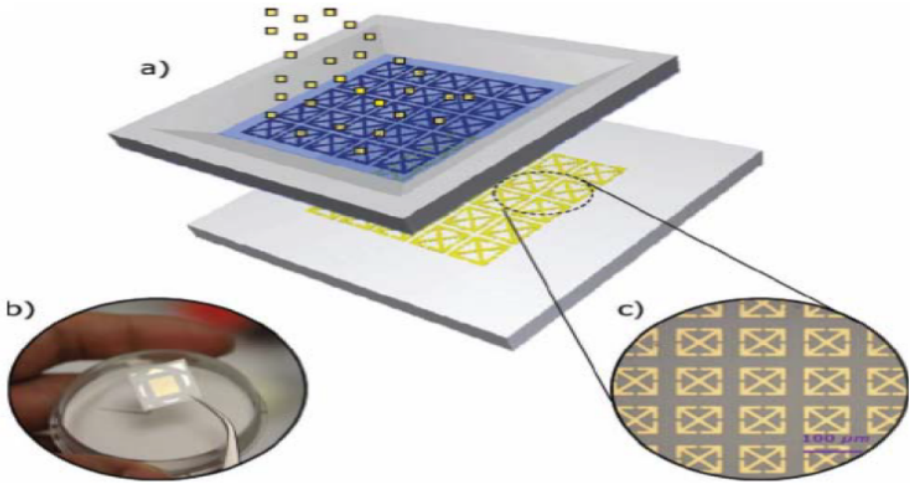

Figure 5.5: " (a) Illustration of micrometer-sized metamaterial resonators adhered to paper substrates through a predefined microstencil. (b) A photograph displaying a terahertz metamaterial sample fabricated on paper. (c) An optical microscopy perspective concentrating on a particular section of an as-constructed paper metamaterial sample" [306].

The resulting paper MM devices display discernible electromagnetic (EM) resonant reactions at predetermined frequencies, contingent upon the resonator's size. This characteristic could serve as a distinctive marker for biological sensing applications. The paper acts as the dielectric substrate for the sensing structure and as a medium to house and interact with analytes.

The application of metamaterial patterning on paper substrates offers a platform where the resonance shifts, primarily influenced by changes in the SRR capacitance due to introduced analytes, could be harnessed for quantitative biochemical sensing purposes. Furthermore, Proof-of-Concept experiments were conducted to observe the alteration in resonance resulting from applying varying concentrations of glucose solutions to the paper MM structure.

In higher frequencies, the effectiveness of metal-based absorbers can be compromised due to the degradation of electrical properties such as permeability and permittivity [307]. These absorbers also exhibit high sensitivity to temperature and are limited in their application at terahertz (THz) frequencies. The

susceptibility of metals to oxidation and corrosion further curtails the lifespan of these absorbers [308]. Although graphene has been explored for tuning frequency responses, its complex fabrication poses challenges [309]. Alternatively, dielectric-based absorbers have gained prominence [310], being both pragmatic and uncomplicated to manufacture compared to graphene-based counterparts.

Furthermore, dielectric-based absorbers remain resilient against temperature and environmental influences [311], unlike graphene-based absorbers, which suffer from bulkiness and intricate structures, leading to fabrication complexities [311, 312]. Recent advancements have focused on slim absorbers with simplified configurations to achieve narrow or ultra-narrow absorption frequency responses [313]. However, attaining high sensitivity, the figure of merit (FOM), and the quality factor (Q) in these absorbers necessitates considerable effort [314]. Achieving perfection in a dielectric-based absorber for biosensing applications is also a formidable challenge [315, 316].

Nevertheless, absorbers with single-band absorption characteristics present limitations in numerous applications. Designs for multiple-band and broadband absorbers hold paramount importance in biosensing applications. Strategies often involve stacking multiple layers or adopting coplanar super-unit structures to achieve multiple absorption peaks or broadened resonance bandwidths. Broad bandwidths are realized by deploying two perpendicular anti-symmetric resonators [317]. As multiple frequency bands increase, structural alterations like toothed resonators, split ring resonators, and perforated square patches come into play [318–320]. Notably, the tunability of these absorbers can be altered through material conductivity adjustments [321]. However, the flexibility in tunability is lacking, contrasting with graphene-based counterparts [322].

Addressing the above design-related issues in dielectric absorbers, several key considerations emerge. Firstly, a reduction in thickness is imperative for compatibility with nanotechnology. Secondly, effective parameters must align with

multi-band criteria, selecting ideal narrow-band absorption tailored for biosensing. Thirdly, simplicity in structure is vital to ensure ease of fabrication. Lastly, the issue of tunability in dielectric absorbers requires resolution.

This chapter presents a novel dielectric metamaterial absorber structure to tackle these challenges. The design incorporates a rectangular ring structure for resonance, with rotation introducing triple resonance capabilities. Additionally, a circular graphene ring is integrated to fine-tune absorption peaks and enhance sensitivity. The proposed structure's performance is evaluated across parameters such as analyte thickness, refractive index, malaria disease detection, and glucose levels in water. This innovative approach promises advancements in the field of dielectric-based absorbers, specifically tailored for biosensing applications.

5.2 Structure Design Detail

The unit cell structure of the tri-band absorber is shown in Fig. 5.6 The structure has three layers: the bottom layer consists of gold, the top layer is a square silicon ring with $\epsilon_r = 11.9$ and a silicon dioxide (SiO_2) with $\epsilon_r = 2.25$ between these two layers. The square silicon ring (SSR) dimensions are of outer side l, thickness t, and width of ring w. Here, silicon dioxide (SiO_2) behaves like a substrate with periodicity p and thickness ts. The proposed SSR is used as a resonator, and its length is assumed to be multiple of guided wavelength (λg)—the value of λg calculated at a frequency of fundamental resonance of the SSR resonator. The SSR is rotated by 45^0 to get impedance matching for three bands. The gold is used as a reflector due to the overall height of the unit cell that remains $\approx \lambda_g/12$. A graphene ring tunes resonance and frequency in the unit cell by shifting the fermi energy with applied biasing. Therefore, a single layer of thick graphene is grown above SiO_2 whose inner and outer radius are r_i =5 μm and r_o=7 μm, respectively. Initially, the electrical properties of graphene

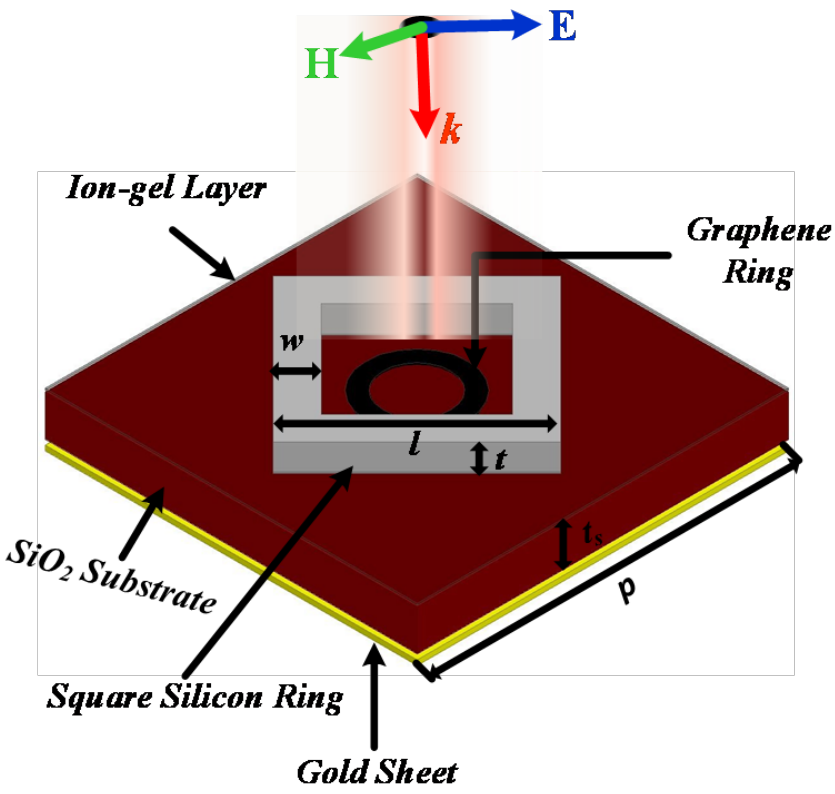

Figure 5.6: Unit cell structure of proposed absorber.

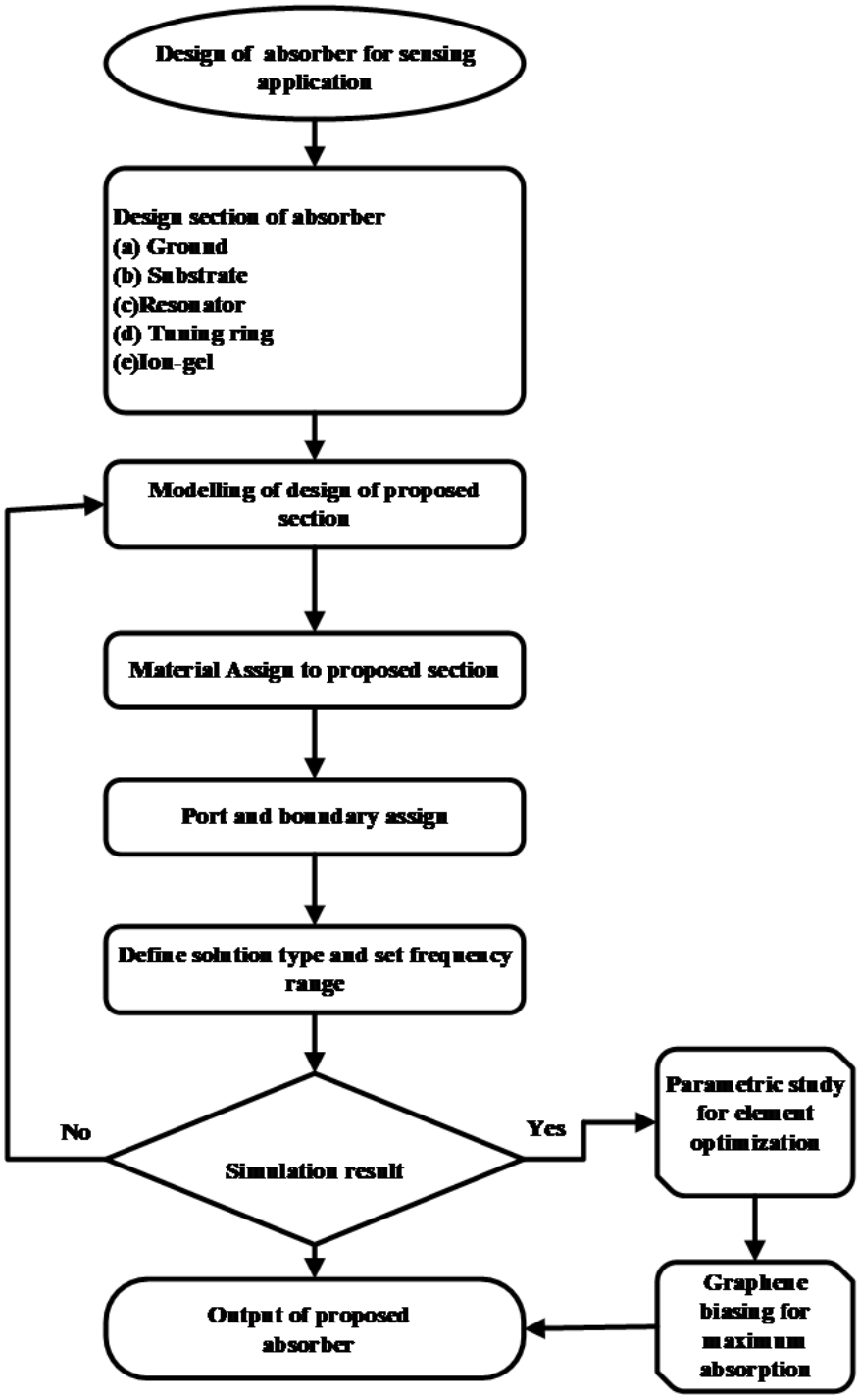

Figure 5.7: Simulation flow chart of proposed absorber

are chosen from the literature [306]. These properties include chemical potential, $\mu_c = 0eV$ with relaxation time $\tau_r = 0.1ps$, and temperature. To provide the biasing, ion-gel is introduced above this graphene ring with height $h_{ion} = 0.1\mu m$.

The proposed absorber is designed using CST Microwave Studio. The simulation process of designing the absorber using CST-2019 microwave studio is presented in the following flowchart in Fig. 5.7. In this software, the proposed absorber design and signal analysis have been carried out with a frequency domain solver, which uses the finite element method (FEM) numerical techniques. In this, a periodic boundary condition is applied to realize the absorber. This technique breaks the structure into small subsections to form a tetrahedral structure to generate finite element mesh. The field solution is determined by using Maxwell's equation in inter-element boundaries. The proposed unit cell is analyzed using floquet ports with open add space boundaries in the direction of propagation. The mesh size is taken $\lambda/20$, and the total tetrahedrons for the solution are 3, 96,240 because the graphene ring's thickness is relatively small compared to the SRR resonator.

5.3 Absorber Analysis

The comprehensive analysis of the proposed Split-Step Resonator (SSR) design was conducted across various layers, each exhibiting distinct absorption characteristics. This analytical journey is illustrated in Fig. 5.8. Fig.5.8(a) initially showcases a pure gold metal layer, functioning as a near-perfect reflector within the operational frequency range. Subsequently, Fig.5.8(b) presents the addition of a SiO_2 substrate over the gold layer, yet this configuration yields a response akin to the gold layer alone. The subsequent design iteration introduces a rectangular silicon ring layer placed above the SiO_2 substrate. This arrangement, illustrated in Fig. 5.8(c), portrays resonance at 6.2 THz, 6.57 THz, and 7.72

THz. This resonant behavior is also mirrored in the absorption peaks and their corresponding phases. Notably, 0.98, 0.97, and 0.76 absorption peaks occur at 6.2 THz, 6.57 THz, and 7.72 THz, respectively.

Continuing this evolution, the silicon ring is rotated by 45^0 degrees, maintaining the same resonant frequencies. However, the absorptivity significantly escalates to more than 0.97, as evidenced in Fig. 5.8(d). The final iteration encompasses introducing a graphene annular ring surrounded by a thin layer of ion-gel with dimensions equivalent to the substrate. This addition precipitates a shift in the absorption peak towards lower frequencies. Resonant frequencies are measured at 6.15 THz, 6.53 THz, and 7.7 THz. This alteration is paralleled by a remarkable enhancement in absorptivity, exceeding 0.99 for all three frequency bands. It is pivotal to recognize that the absorptivity and resonance characteristics of the proposed structure are chiefly governed by the presence of graphene, as discernible in Fig. 5.8(e).

In essence, the absorber analysis journey systematically assessed the evolution of the SSR design across various layers. Each modification yielded distinct absorption behaviors, ultimately culminating in the introduction of graphene, which exerted substantial control over the absorptivity and resonant characteristics of the structure. The proposed structure is analyzed using absorption A, which can be calculated by

5.4 Equivalent Electrical Circuit

The equivalent electrical circuit (EC) of the proposed absorber is examined by using the transmission line method (TLM) as shown in Fig. 5.9. The ABCD parameter of EC can be written as,

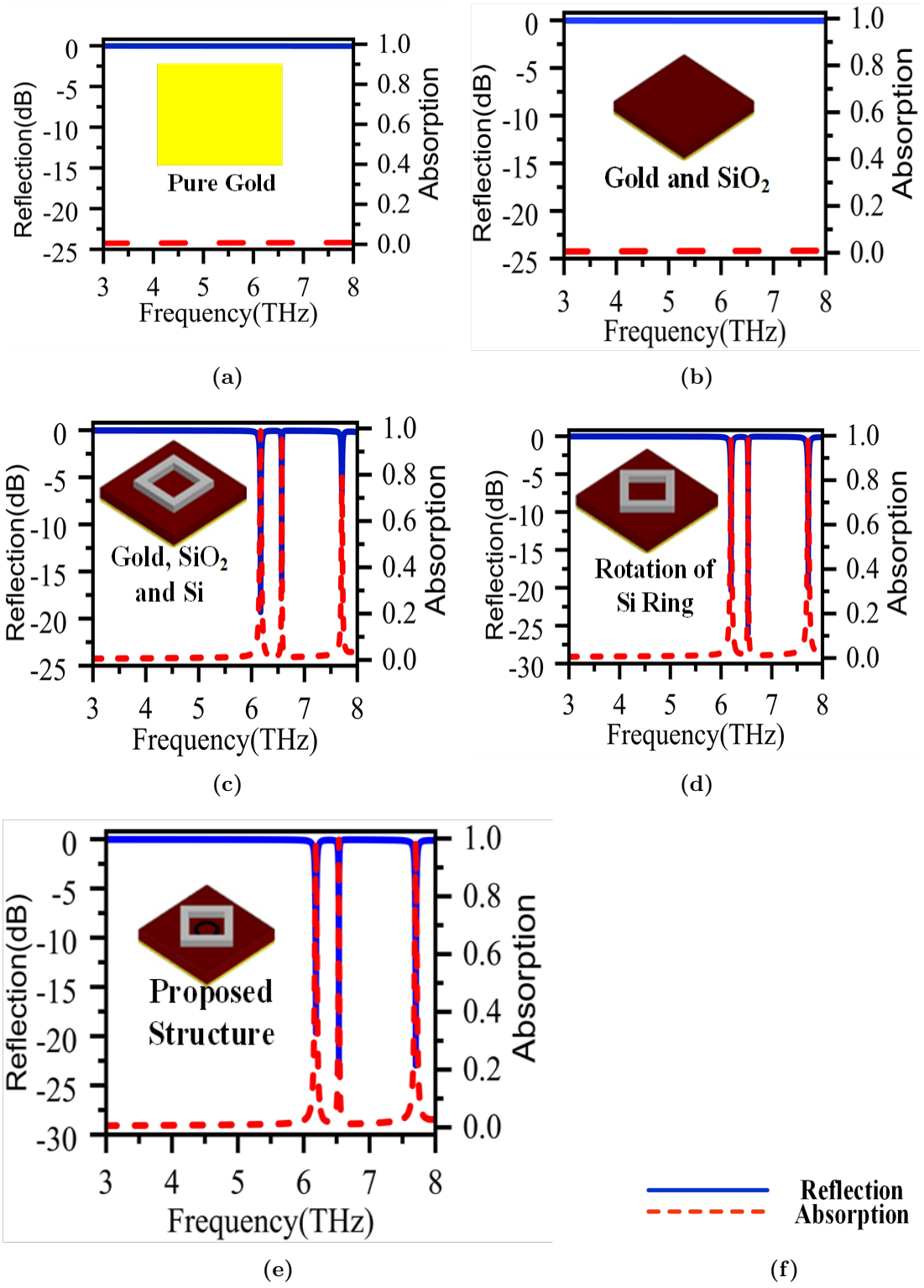

Figure 5.8: Design evolution of absorber.

$$\begin{bmatrix} A & B/Z_0 \\ CZ_0 & D \end{bmatrix} = \begin{bmatrix} Z_g & 0 \\ 1 & 1 \end{bmatrix} \times \begin{bmatrix} 1 & 0 \\ Y_{Si} & 1 \end{bmatrix} \times \begin{bmatrix} \cos\theta_T & jZ_T \sin\theta_T \\ jY_T \sin\theta_T & \cos\theta_T \end{bmatrix} \tag{5.1}$$

Where $\theta_T = \beta_T d$ and Z_T is the impedance of the transmission line. The impedance Z_T is a series combination of $Z_{ion-gel}$ and Z_{SiO_2} i.e. $Z_T = Z_{ion-gel} + Z_{SiO_2}$. The value of these impedances $Z_{ion-gel}$ and Z_{SiO_2} can be calculated by

$$\begin{aligned} Z_{SiO_2} &= {}^{Z_0}/_{\sqrt{\varepsilon_s}} \\ Z_{ion-gel} &= {}^{Z_0}/_{\sqrt{\varepsilon_{ion-gel}}} \end{aligned} \tag{5.2}$$

Here,$Z_0$is free space impedance. β_T and d are phase constant and height of transmission line. Hence the value of phase constant, β_T and height, d are given by:

$$\begin{aligned} \beta_T &= \frac{\omega}{c}\left[\sqrt{\varepsilon_s} + \sqrt{\varepsilon_{ion-gel}}\right] \\ d &== t_s + t_{ion-gel} \end{aligned} \tag{5.3}$$

From the calculated ABCD matrix, the reflection coefficient, $S_{11}$of structure can be calculated [313],

$$S_{11} = \frac{A + {}^{B}/_{Z_0} - Z_0 C - D}{A + {}^{B}/_{Z_0} + Z_0 C + D} \tag{5.4}$$

5.5 Sensing Performance Analysis

5.5.1 Analyte Thickness Sensing

The proposed absorber's test material thickness (ta) can be analyzed by varying analyte thickness. The refractive index (n) of the analyte is chosen as 1.3. The sensing parameters that are key for any absorbers are sensitivity (S), a figure of merit (FOM), full-width at half-maximum (FWHM), and quality Factor (Q). The sensitivity is defined as the shift in frequency (Δf) concerning change in test

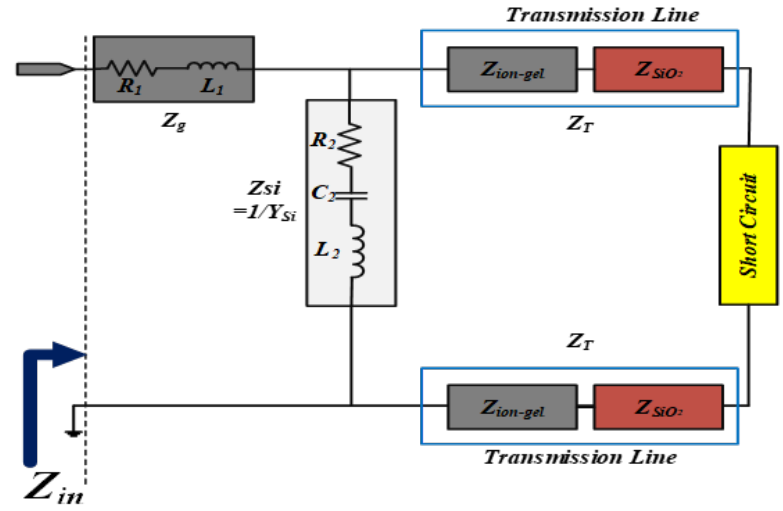

(a)

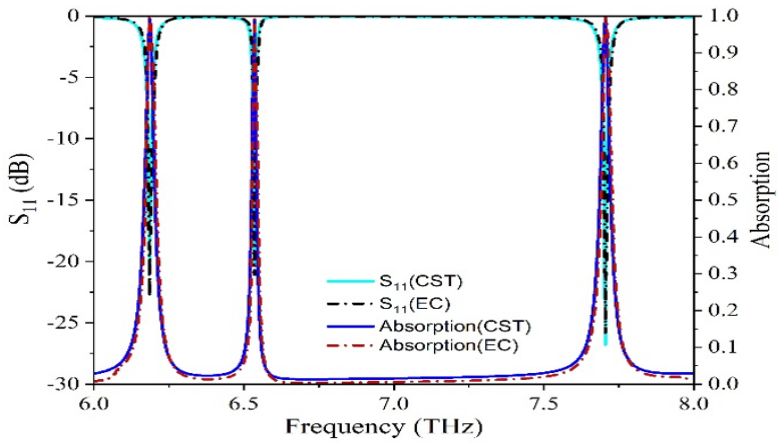

(b)

Figure 5.9: (a)Equivalent circuit of absorber (b) Plot of S_{11} and absorption obtained from simmulator and electrical circuit (EC).

material thickness (Δt_a). The highest sensitivity values with analyte thickness are 0.445 THz TU^{-1}, 0.4255 THz TU-1, and 0.4305 THz TU^{-1} in the lower, middle, and upper bands, respectively, shown in Fig. 5.10(b). The absorber's merit (FOM) can be calculated as sensitivity ratio to full-width half maximum absorption. The maximum values of FOM are 13.9 TU^{-1}, 21.25 TU^{-1}, and 10.64 TU^{-1} in the lower, middle, and upper bands, respectively, as shown in Fig. 5.10(c). The quality factor of the absorber can be given as a ratio of peak absorption frequency to FWHW. The proposed structure provides the highest Q values of 235, 653, and 264 in the lower, middle, and upper bands, respectively, shown in Fig. 5.10(d).

5.5.2 Refractive Index Sensing

The realization of the refractive index sensor of the proposed absorber with a thickness of analyte is $t_a = 0.6\mu m$. The refractive index value varies from 1 to 2 with step 0.2 to calculate their sensing parameter. Here, the sensitivity is defined as frequency shift (Δf) concerning the change in refractive index (Δn). The highest sensitivity values with change of refractive index are 0.480 THz RIU^{-1}, 0.403 THz RIU^{-1}, and 0.562 THz RIU^{-1} in lower, middle and upper bands, respectively, shown in Fig 5.10(f). The maximum value of FOM is 16.57 RIU^{-1}, 22.38 RIU-1, and 17.03 RIU-1in the lower, middle and upper bands, respectively, as shown in Fig. fig5:10(g). The quality factor of the absorber can be given as a ratio of peak absorption frequency to FWHW. The proposed structure providing the highest Q values 203, 555, and 261 in the lower, middle and upper bands, is shown in Fig. 5.10(h).

5.5.3 Diagnosis of Malaria

The worldwide malaria infection is very high, according to a report provided by WHO. Therefore, the detection of this disease is necessary to avoid fatality.

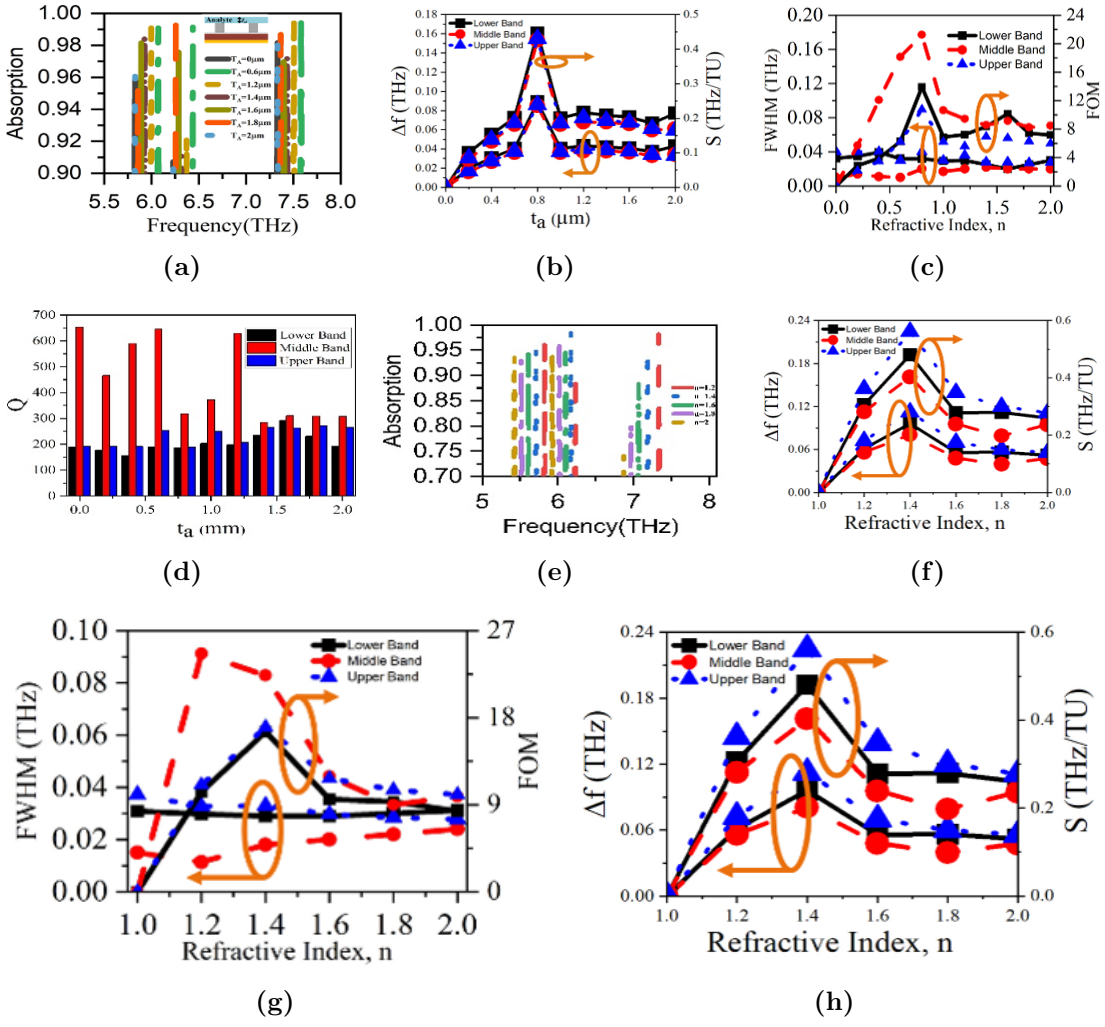

Figure 5.10: Design evolution of absorber.

Table 5.1: Sensing Performance for Malaria and Water/ Glucose.

	n	S [THz TU^{-1}]			FWHM [THz]			FOM [RIU-1]			Q		
Malaria	1.373	0.75	0.643	0.817	0.0125	0.013	0.0111	60.053	49.49	73.66	473.6	486.92	668.01
	1.383	0.6	0.5	0.6	0.0102	0.013	0.0107	58.82	38.46	56.07	579.60	486.40	692.1
Water/Glucose	1.3198	0.830	0.721	0.89	0.0193	0.0162	0.0187	43.04	44.50	47.77	307.51	391.36	397.6
	1.3594	0.57	0.47	0.61	0.0176	0.0139	0.0212	32.34	33.83	28.84	335.90	454.75	349.54

Malaria detection uses red blood cells (RBC), which have a refractive index of 1.383 and 1.373 in different stages [305]. The performance of the proposed structure is tabulated in Table 5.1. Here the sensitivity of refractive index 1.373 are 0.75 THz RIU^{-1}, 0.643 THz RIU^{-1}, and 0.817 THz RIU^{-1} in the lower, middle and upper band, respectively and their FOM of 60.053 RIU^{-1}, 49.49 RIU^{-1}, and 73.66 RIU^{-1} and high Q of 473.6, 486.92, and 668.01 in lower, middle and upper band. Further, the sensitivity of refractive index 1.383 are 0.6 THz RIU^{-1}, 0.5THz RIU^{-1}, and 0.5 RIU^{-1} in lower, middle and upper bands, respectively and their FOM of 58.82 RIU^{-1}, 38.46 RIU^{-1}, and 56.07 RIU^{-1} and high Q of 579.60, 486.40, and 692.1 in lower, middle and upper band. The proposed sensor has very high Q, good sensitivity and high FOM.

5.6 Water/Glucose Detection

The structure performance as a sensor can be analyzed for water and water with 25% of glucose. The refractive index of water and water with 25% of glucose are 1.3198 and 1.3594, respectively. Table 5.1 contains the performance parameters of water and water with 25% glucose. The proposed sensor has very high Q, reasonable sensitivity, and high FOM, making it a good candidate for glucose detection in water.

5.7 Performance Comparison

The absorber performance has been compared with some existing work of a similar nature available in the literature, as reflected in Table 5.2. This table

Table 5.2: Comparision of absorber performance.

Ref	No. of Band	Frequency (THz)			Sensitivity (THz RIU^{-1})			FOM (RIU^{-1})			Q			Tunability
		LB	MB	UB	LB	MB	UB	LB	MB	UB	LB	MB	UB	
[296]	Two	1.8	-	2.26	0.188	-	0.36	7.2	-	19.1	120	-	94	No
[295]	Two	1.42	-	2.99	0.28	-	1.48	1.2	-	24.6	7.11	-	59.8	No
	Two	0.76	-	1.28	0.47	-	0.51	9.4	-	14.4	23	-	3.7	No
[303]	Single	2.25	-		0.3	-		2.94	-		22.05	-		No
[312]	Two	4.515	-	4.914	0.2	-	0.1	4.76	-	3.5	105.2	-	211.8	Yes
[304]	Two	5.78	-	6.465	0.5	-	0.462	33.3	-	43.2	394.2	-	624.4	Yes
[314]	Three	1.09	2.86	4.06	0.10	0.38	0.48	0.7	1.88	2.38	7.05	12.7	18.06	No
This work (Analyte)	Three	6.00	6.37	7.532	0.44	0.425	0.430	13.9	21.2	10.6	235	653	264	Yes
This work (RI)		5.91	6.24	7.41	0.48	0.403	0.562	16.57	22.4	17.0	203	555	261	
This work (Malaria)		5.92	6.33	7.415	0.75	0.643	0.817	60.05	49.5	73.7	473.6	486.9	668	
This work (Glucose)		5.93	6.34	7.435	0.83	0.721	0.89	43.04	44.5	47.8	307.51	391.4	397.6	

compares the number of bands, sensitivity, FOM and quality factor with their tunning properties. Furthermore, the proposed sensor provides good sensitivity, high FOM, and high-quality factors.

5.8 Summary

This chapter mainly focused on designing a THz absorber as a biosensor. The design involves a collaborative interaction between a silicon rectangular ring and a circular graphene ring. The silicon ring establishes resonance characteristics, while the graphene ring controls resonance shifting. We have also incorporated an equivalent circuit model to validate the biosensor's performance. We have evaluated key parameters like Sensitivity, Quality Factor (Q), and Figure of Merit (FOM) to gauge the sensor's effectiveness. Our analysis covers two scenarios: one with varying analyte thickness and the other with changing refractive index. Sensitivity values vary between 0.445 to 0.4305 THz TU^{-1} for analyte thickness, with corresponding quality factors ranging from 235 to 264. When considering refractive index changes, the sensor's effectiveness improves. Sensitivity shifts to values between 0.480 to 0.562 THz RIU^{-1}, and quality factors range from 203 to 261. This design stands out as a promising biosensor with its strong polarization insensitivity.

6

Multi-Band Absorber with Tunable Bio-Sensor Application

Contents

6.1 Introduction

Metamaterials are artificially engineered electromagnetic materials and these properties are different from natural materials. Metamaterials have properties such as negative refractive index, inverse Doppler effect, superlensing, electromagnetic wave cloaking, and perfect absorber. Metamaterial absorbers can absorb electromagnetic radiation over a specific frequency range or at particular frequencies. Metamaterial absorbers have applications such as thermal images, solar cells, sensors, multiband, and broadband. This can be used to detect electromagnetic signals within those frequencies in sensing applications. The design of a metamaterial absorber capable of resonance at a specific frequency for microwave or terahertz sensing can allow for the detection of any changes in that frequency. In chapter 5, content the dual band biosensor here in this chapter we are getting pentaband for biomedical applicaions. In this, a hexagonal structure with a graphene ring will generate five band peaks through which an ultra-thin multiband absorber creates biosensing applications. At the bottom layer of the structure is a ground plane which is made up of gold, and works asa good reflector. A SiO_2 dielectric material is used for the substrate that provides a high dielectric strength and excellent thermal stability. With the help of a graphene ring which is in the center, a hexagonal ring that creates multi-band resonance will give better tuning. As shown in the Fig. 6.1.

6.2 STRUCTURE DESIGN DETAIL

The unit cell structure of the quad-band absorber is shown in Fig. 6.1.The structure mainly has three layers, the bottom layer consists of gold, the top layer is made up of a square silicon ring with $\epsilon_r = 11.9$ and in between these two layers a silicon dioxide (SiO_2) with $\epsilon_s = 2.25$ is grown. The square silicon ring (SSR) dimensions are outer sidel, thickness t,and width of ring w. Here silicon dioxide

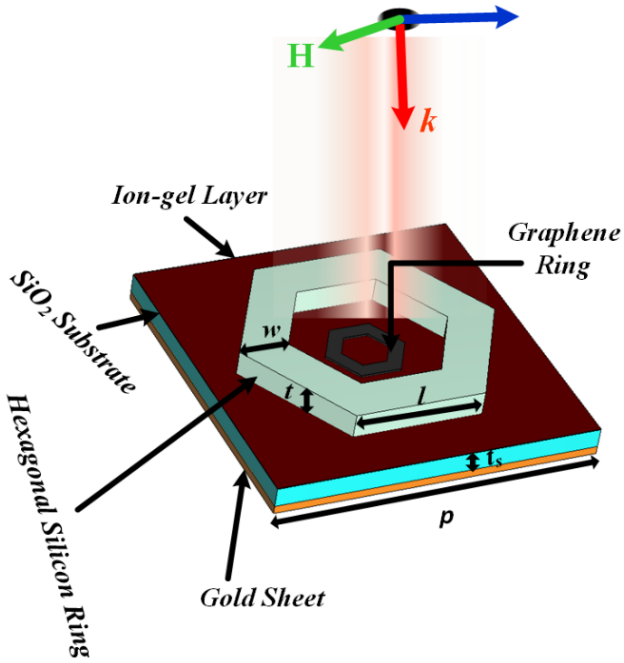

Figure 6.1: Unit cell structure. Here l=70 μm, p=150 μm, $t_s = 0.5\mu m$, $w = 16.8m$, $t_g = 0.34$ μ m, and $t = 3.1$ μm.

(SiO_2) behaves like a substrate with periodicity p and thickness t_s. The proposed SSR is used as a resonator and its length is multiple of guided wavelength (λ_g). The value of λ_g calculated at a frequency of fundamental resonance of the SSR resonator. The gold is used as a reflector, due to the overall height of the unit cell remains $\approx \lambda_g/12$. In the unit cell, a graphene ring is used to tune resonance and frequency by shifting the fermi energy with applied biasing. Therefore, a single layer graphene with a thickness λ_g is grown above Whose width=5 μm and side length=12 μm respectively. Initially, the electrical properties of graphene are selected according to the literature [22]. These properties include chemical potential, $\mu_c = 0\ eV$ with relaxation time, $\tau_r = 0.1\ ps$ at temperature $T = 300K$.To provide the biasing, ion-gel is introduced above this graphene ring with height $h_{ion} = 0.1\ \mu m$. The proposed absorber is designed on a commercially available 3D EM simulator CST Microwave studio by DASSULT. The simulation process involved in the designing absorber using CST microwave studio is presented in

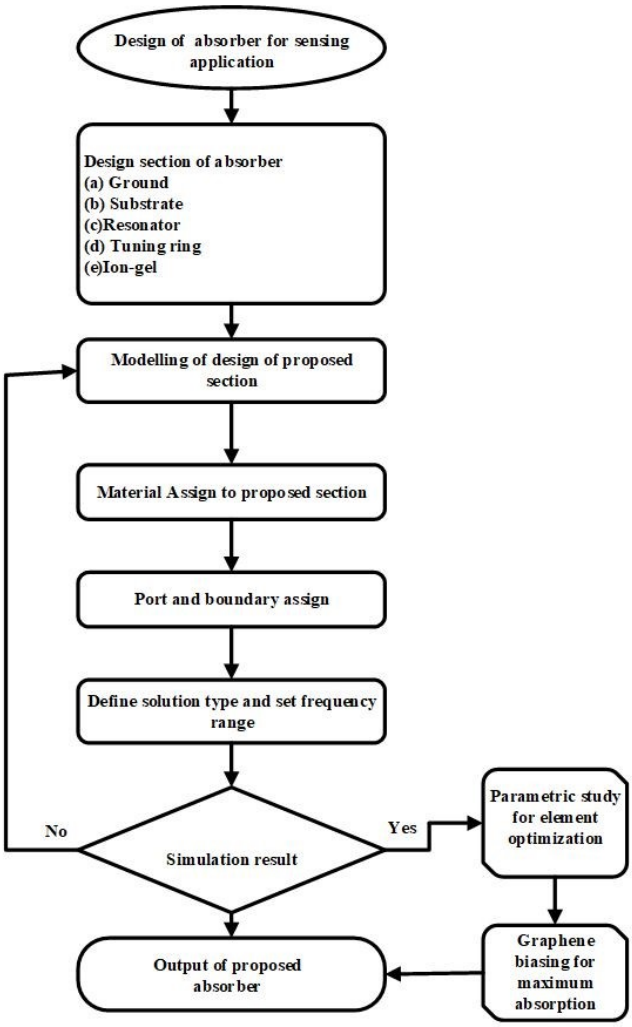

Figure 6.2: Unit cell structure. Here l=70 μm, p=150 μm, $t_s = 0.5\mu m$, $w = 16.8m$, $t_g = 0.34$ μ m, and $t = 3.1$ μm.

the following flowchart shown in Fig. 6.2. In this software proposed absorber is based on a frequency domain solver which uses the finite element method (FEM) numerical techniques. In this technique, the structure is brokeninto small subsections to form a tetrahedral structure to generate finite element mesh. The field solution is determined by using Maxwell's equation in inter-element boundaries. The proposed unit cell is analyzed using floquet ports with open add space boundaries in the direction of propagation. The mesh size is taken $\lambda/20$ and the total tetrahedrons for the solution are $3,96,500$ because the thickness of the graphene ring is quite smaller than the SRR resonator.

6.3 ABSORBER ANALYSIS

The design evolution of the proposed SSR was analyzed for different layers and their absorption characteristic in Fig. 6.3. Fig. 6.3(a) shows a pure gold metal layer, which behaves as a perfect reflector in the working frequency band. Later, a SiO2 substrate was cladded tothe gold layer as shown in Fig. 6.3(b) but it also showsa similar response as the gold layer. The third layer of the rectangular silicon ring is grown above the SiO2 substrate. The frequency response plot in Fig. 6.3(c) shows resonance at 4.75THz, 5 THz, 5.536 THz, 5.4 THz 5.76 THz, and 5.88 THz, it also reflected in absorption peak and their phase. The absorption peak is 0.88,0.99, 0.50, 0.89, 0.75, and 0.59 at 4.75 THz, 5 THz, 5.536 THz, 5.4 THz 5.76 THz, and 5.88 THz. Next evolution, a graphene hexagonal ring is introduced which is cladded by a thin layer of ion-gel with equal dimensions of the substrate. The addition of a graphene ring shifted the absorption peak with the resonant frequency at 4.78 THz, 5.1 THz, 5.4 THz, 5.76 THz, and 5.88 THz and improves the absorptivity level by more than 0.97 for all five bands. The absorptivity and resonance of the proposed structure are controlled by graphene, which can realizedin Fig. 6.3(d).

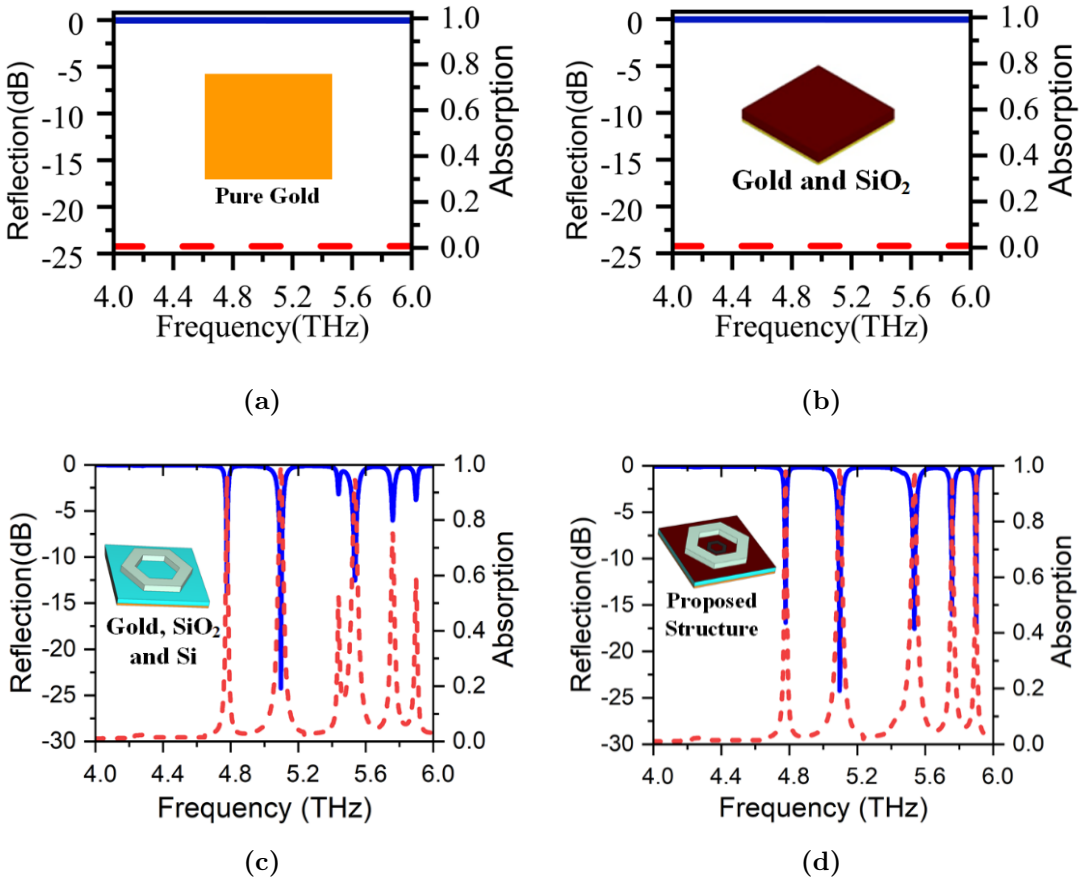

Figure 6.3: Design evolution of absorber.

$$A = 1 - T - R \tag{6.1}$$

Where T and R are transmission co-efficient and reflection co-efficient of structure respectively. This coefficient can be obtained directly from the EM simulator. Here, the proposed structure uses gold as a bottom, therefore transmission coefficient (T) becomes zero and absorption,$A = 1 - R$.

6.4 EQUIVALENT ELECTRICAL CIRCUIT

The equivalent electrical circuit (EC) of the proposed absorber is examined by using the transmission line method (TLM) as shown in Fig. 6.4. The ABCD

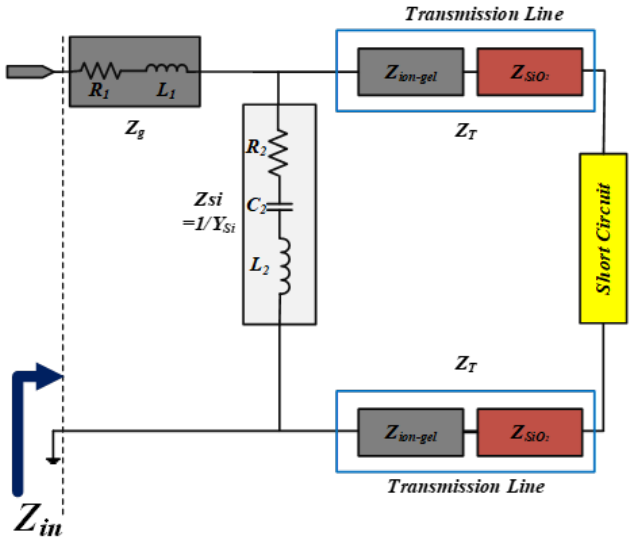

(a)

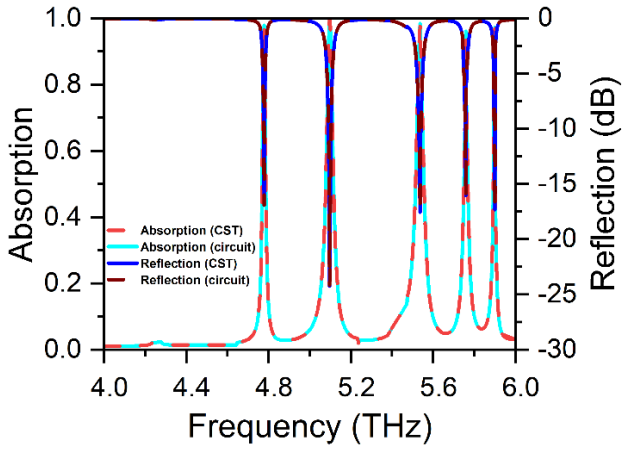

(b)

Figure 6.4: (a)Equivalent circuit of absorber (b) Plot of S_{11} and absorption obtained from simmulator and electrical circuit (EC).

parameter of EC can be written as,

$$\begin{bmatrix} A & B/Z_o \\ CZ_o & D \end{bmatrix} = \begin{bmatrix} Z_g & 0 \\ 1 & 1 \end{bmatrix} \times \begin{bmatrix} 1 & 0 \\ Y_{Si} & 1 \end{bmatrix} \times \begin{bmatrix} \cos\theta_T & jZ_T \sin\theta_T \\ jY_T \sin\theta_T & \cos\theta_T \end{bmatrix} \tag{6.2}$$

where $\theta_T = \beta_T d$ and Z_T is the impedance of the transmission line. The impedance Z_T is series combination of $Z_{ion-gel}$ and Z_{SiO_2} i.e.$Z_T = Z_{ion-gel} + Z_{SiO_2}$. The value of these impedances $Z_{ion-gel}$ Z_{SiO2} can be calculated by

$$Z_{ion-gel} = Z_0/\sqrt{\varepsilon_{ion-gel}} \tag{6.3}$$

$$Z_{Sio2} = Z_0/\sqrt{\varepsilon_s} \tag{6.4}$$

Here Z_0 is free space impedance. β_T and d are phase constant and height of the transmission line. Hence the value of the phase constant, $\beta_T$and height, $d$are given by

$$\beta_T = \frac{\omega}{c}(\sqrt{\varepsilon_s} + \sqrt{\varepsilon_{ion-gel}} \tag{6.5}$$

$$d == t_s + t_{ion-gel} \tag{6.6}$$

From the calculated ABCD matrix, the reflection coefficient,S_{11} of the structure can be calculated [22],

$$S_{11} = \frac{A + {}^{B}/_{Z_0} - Z_0 C - D}{A + {}^{B}/_{Z_0} + Z_0 C + D} \tag{6.7}$$

6.5 SUMMARY

This chapter generates Multi-band resonance for biosensing applications.A silicon hexagonal ring to provide a pentaband of resonance and their properties is introduced using a hexagonal graphene ring in the center. The absorber performance parameter is verified using an equivalent circuit model. The proposed design has a resonance at 4.78 THz, 5.1 THz, 5.4 THz, 5.76 THz, and 5.88 THz and improves the absorptivity level by more than 0.97 for all five bands.Another

important feature of the proposed absorber is polarization insensitive.

7

Summary and Conclusions

Contents

7.1 Summary

Chapter 1 discusses an overview of metamateral absorbers and their applications briefly. Chapter 2 presented a survey on existing woks on metamaterial absorber. In Chapter 3, a ring shape of graphene based structure is investigated to enhance the bandwidth. Chapter 4 illustrated two different metamaterial absorbers such as dual-band and triple band absorbers using CSRR structure to achieve a good absorption level. In Chapter 5, a graphene ring incorporated with silicon ring as a sensor has been implemented for biomedical applications. Chapter 6 detailed about hexagonal shape structure to generate multiband peaks.

7.2 Contributions of the Work

This research analyzes different metamaterial structures with different operating frequencies at the THz level. Firstly, a graphene-based broadband metamaterial absorber has been proposed. This design uses a circular graphene ring to enhance the bandwidth. The structure exhibits a bandwidth of 67% for absorption of more than 90% and a bandwidth of 46 for absorption more significant than 98%. The proposed structure is compared with the available literature, and the presented structure offers better performance characteristics than the existing one. Also, it offers TE and TM polarization insensitivity up to a 600 incident angle of electromagnetic wave.

Design 2 presents a dual band metamaterial absorber based on Complementary Split Ring Resonators (CSRR). This structure exhibits exceptional absorption efficiencies of 100% in the lower band and 98.6% in the upper band. Notably, it is observed that the upper band frequency is more sensitive compared to the frequencies in the lower band. The proposed structure achieves maximum quality factors of 19.20 THz/RIU in the lower band and 19.56 THz/RIU in the upper band. Furthermore, the Figure of Merit (FOM) is measured at 11.43 RIU^{-1} in

the lower band and 11.79 RIU^{-1} in the upper band. In Design 3, we designed a simple structure using CSRR called MM, which provides multiple bands. The multiband peaks generated here are not identical in terms of height. The first peak absorption is 100%, and the other peak is found to be 96% followed by the third one as 70%. This structure is mainly designed for sensing applications. It can further be extended for biomedical applications by reducing its size and number of CSRR structures. The results and the performance of the proposed structure are very much modified with the inclusion of many other material in place of graphene and gold.

In design 4, we emphasize the design to perform as an absorber at the THz regime. It is just a composite structure to function as a biosensor primarily dictated by the collective response of a silicon rectangular ring incline at 45^0 and a circular graphene ring structure placed above the substrate. The rectangular Si ring will provide the required resonance characteristics, whereas the graphene ring controls the shifting of that. This literature also encompasses an equivalent circuit model to ensure the performance of biosensors. Sensitivity, Quality factor, and FOM results are the key parameters that could comprehend the structure's utility as a sensor. Two sets of results for the said parameter are projected with and without refractive index variation. From the analysis, it is found that the sensitivity with analyte thickness is 0.445 THz TU^{-1}, 0.4255 THz TU^{-1}, and 0.4305 THz TU^{-1} and the corresponding quality factor for the lower, middle, and upper bands as 235, 653, and 264 respectively. With a variation of the refractive index value, the obtained results provide a fair amount of changes, which bring the structure to perform as a sensor. The changed results for the same parameter are 0.480 THz RIU^{-1}, 0.403 THz RIU^{-1}, and 0.562 THz RIU^{-1} in terms of sensitivity, and the corresponding quality factors values are 203, 555, and 261 for lower, middle, and upper bands respectively. As an extensive result, its good polarization-insensitive nature makes the structure elegant as a sensor.

In the design 5, it generates Multi-band resonance for biosensing applications. A silicon hexagonal ring to provide a pentaband of resonance and their properties is introduced using a hexagonal graphene ring in the center. The absorber performance parameter is verified using an equivalent circuit model. The proposed design has a resonance at 4.78 THz, 5.1 THz, 5.4 THz, 5.76 THz, and 5.88 THz and improves the absorptivity level by more than 0.97 for all five bands.Another important feature of the proposed absorber is polarization insensitive.

7.3 Future Scope

Terahertz (THz) metamaterials have special qualities such as high sensitivity, non-ionizing, and biomolecule interaction, making them very promising for future biosensor technology development. The following are some important domains where THz metamaterials may influence biosensors in the future:

(i) Enhanced sensitivity and specificity

- **Molecular fingerprinting:** It is possible to accurately identify and quantify different biological components by engineering THz metamaterials to resonate at certain frequencies that correspond to the vibrational modes of biomolecules.
- **Label-Free Detection:** THz biosensors have the ability to identify biomolecules without the use of radioactive or fluorescent labels, which streamlines the detection procedure and lowers the possibility of interferences.

(ii) Cancer detection: THz waves use a tissue's dielectric characteristics to distinguish between healthy and cancerous cells. The precise and early detection of cancer can be enhanced by metamaterial-based sensors.

(iii) Pathogen Detection: To ensure food product safety and quality, THz sensors can be used to identify substances and pathogens.

(iv) Biomolecular Research: THz metamaterials can support basic biological research by aiding in the study of the dynamics and structure of proteins, DNA, and other biomolecules.

(v) Agricultural applications: THz sensors analyse changes in the spectral signatures of plants to identify illnesses and stress.

(vi) Improved data analysis: Combining THz biosensors with AI and machine learning can enhance data analysis, improving the accuracy and speed of diagnostics.

In the works reported in this thesis, experimental analysis at THz frequencies was absent. Therefore, future research could involve developing a fabricated prototype to validate the simulated performance outcomes.

List of Publications

Journal Publications

1. **Deekonda LN**, Sahu SK, Panda AK, Ranjan R, Khera S. An Ultrathin Triple-Band Absorber for Tuneable THz Bio-sensing. Microw Opt Technol Lett. 2023; 65: 3035-3042. doi:10.1002/mop.33826.

2. **Deekonda LN**, Sahu SK, Panda AK, Ranjan R, Ultrathin Multi-Band AbsorberUsing Graphene Silicon Ring for Tuneable THz Sensing, (Under Review).

Conference and Workshop Publications

1. **L. N. Deekonda**, S. K. Sahu and A. K. Panda, "A Graphene-Based Broadband Metamaterial Absorber," 2021 Advanced Communication Technologies and Signal Processing (ACTS), 2021, pp. 1-4,
doi: 10.1109/ACTS53447.2021.9708250.

2. **L. N. Deekonda**, S. K. Sahu and A. K. Panda, "Dual-Band Terahertz Metamaterial Absorber for a Sensor Application," 2022 International Conference Small Satellities (ICSS), 2022 .

3. **L. N. Deekonda**, S. K. Sahu and A. K. Panda, "A Graphene based a sensor application," Springer ICICS, 2023 . (under Review)

Bibliography

[1] R. M. Walser, "Electromagnetic metamaterials," in *Complex Mediums II: beyond linear isotropic dielectrics*, vol. 4467. SPIE, 2001, pp. 1–15.

[2] N. I. Zheludev, "The road ahead for metamaterials," *Science*, vol. 328, no. 5978, pp. 582–583, 2010.

[3] M. DARPA and N. CHALLENGE, "Defense advanced research projects agency," 2018.

[4] B. Ung, "Metamaterials: a metareview," *Ecole Polytechnique of Montreal: http://www. polymtl. ca/phys/doc/art_2_2. pdf*, vol. 1, 2009.

[5] D. R. Smith, J. B. Pendry, and M. C. Wiltshire, "Metamaterials and negative refractive index," *science*, vol. 305, no. 5685, pp. 788–792, 2004.

[6] N. Seddon and T. Bearpark, "Observation of the inverse doppler effect," *Science*, vol. 302, no. 5650, pp. 1537–1540, 2003.

[7] J. B. Pendry, "Negative refraction makes a perfect lens," *Physical review letters*, vol. 85, no. 18, p. 3966, 2000.

[8] D. Schurig, J. J. Mock, . B. Justice, S. A. Cummer, J. B. Pendry, A. F. Starr, and D. R. Smith, "Metamaterial electromagnetic cloak at microwave frequencies," *Science*, vol. 314, no. 5801, pp. 977–980, 2006.

[9] V. M. Shalaev, "Optical negative-index metamaterials," *Nature photonics*, vol. 1, no. 1, pp. 41–48, 2007.

[10] T. Driscoll, H.-T. Kim, B.-G. Chae, B.-J. Kim, Y.-W. Lee, N. M. Jokerst, S. Palit, D. R. Smith, M. Di Ventra, and D. N. Basov, "Memory metamaterials," *Science*, vol. 325, no. 5947, pp. 1518–1521, 2009.

[11] N. Liu, H. Guo, L. Fu, S. Kaiser, H. Schweizer, and H. Giessen, "Three-dimensional photonic metamaterials at optical frequencies," *Nature materials*, vol. 7, no. 1, pp. 31–37, 2008.

[12] P. Tuong, Y. Yoo, J. Park, Y. Kim, K. Kim, Y. Kim, H. Cheong, L. Chen, and Y. Lee, "Multi-plasmon-induced perfect absorption at the third resonance in metamaterials," *Journal of Optics*, vol. 17, no. 12, p. 125101, 2015.

[13] X. Wang, C. Luo, G. Hong, and X. Zhao, "Metamaterial optical refractive index sensor detected by the naked eye," *Applied Physics Letters*, vol. 102, no. 9, 2013.

[14] J. Hendrickson, J. Guo, B. Zhang, W. Buchwald, and R. Soref, "Wideband perfect light absorber at midwave infrared using multiplexed metal structures," *Optics letters*, vol. 37, no. 3, pp. 371–373, 2012.

[15] N. Liu, M. Mesch, T. Weiss, M. Hentschel, and H. Giessen, "Infrared perfect absorber and its application as plasmonic sensor," *Nano letters*, vol. 10, no. 7, pp. 2342–2348, 2010.

[16] F. B. Niesler, J. K. Gansel, S. Fischbach, and M. Wegener, "Metamaterial metal-based bolometers," *Applied Physics Letters*, vol. 100, no. 20, 2012.

[17] B. Wang, K. H. Teo, T. Nishino, W. Yerazunis, J. Barnwell, and J. Zhang, "Experiments on wireless power transfer with metamaterials," *Applied Physics Letters*, vol. 98, no. 25, 2011.

[18] K. Aydin, V. E. Ferry, R. M. Briggs, and H. A. Atwater, "Broadband polarization-independent resonant light absorption using ultrathin plasmonic super absorbers," *Nature communications*, vol. 2, no. 1, p. 517, 2011.

[19] M. K. Hedayati, B. Mozooni, F. Faupel, and M. Elbahri, "Tunable broadband plasmonic perfect absorber at visible frequencies," in *META'12*, 2012.

[20] A. S. Hall, M. Faryad, G. D. Barber, L. Liu, S. Erten, T. S. Mayer, A. Lakhtakia, and T. E. Mallouk, "Broadband light absorption with multiple surface plasmon polariton waves excited at the interface of a metallic grating and photonic crystal," *ACS nano*, vol. 7, no. 6, pp. 4995–5007, 2013.

[21] P. Tuong, J. Park, V. Lam, W. Jang, S. Nikitov, and Y. Lee, "Dielectric and ohmic losses in perfectly absorbingmetamaterials," *Optics Communications*, vol. 295, pp. 17–20, 2013.

[22] N. I. Landy, S. Sajuyigbe, J. J. Mock, D. R. Smith, and W. J. Padilla, "Perfect metamaterial absorber," *Physical review letters*, vol. 100, no. 20, p. 207402, 2008.

[23] Y. Yoo, H. Zheng, Y. Kim, J. Rhee, J.-H. Kang, K. Kim, H. Cheong, Y. Kim, and Y. Lee, "Flexible and elastic metamaterial absorber for low frequency, based on small-size unit cell," *Applied physics letters*, vol. 105, no. 4, 2014.

[24] X. Liu, T. Starr, A. F. Starr, and W. J. Padilla, "Infrared spatial and frequency selective metamaterial with near-unity absorbance," *Physical review letters*, vol. 104, no. 20, p. 207403, 2010.

[25] X. Liu, T. Tyler, T. Starr, A. F. Starr, N. M. Jokerst, and W. J. Padilla, "Taming the blackbody with infrared metamaterials as selective thermal emitters," *Physical review letters*, vol. 107, no. 4, p. 045901, 2011.

[26] J. Hao, L. Zhou, and M. Qiu, "Nearly total absorption of light and heat generation by plasmonic metamaterials," *Physical review B*, vol. 83, no. 16, p. 165107, 2011.

[27] X.-Y. Peng, B. Wang, S. Lai, D. H. Zhang, and J.-H. Teng, "Ultrathin multi-band planar metamaterial absorber based on standing wave resonances," *Optics express*, vol. 20, no. 25, pp. 27 756–27 765, 2012.

[28] Y. Cheng, Y. Nie, R. Gong, and H. Yang, "Multi-band metamaterial absorber using cave-cross resonator," *The European Physical Journal-Applied Physics*, vol. 56, no. 3, p. 31301, 2011.

[29] Y. Ma, Q. Chen, J. Grant, S. C. Saha, A. Khalid, and D. R. Cumming, "A terahertz polarization insensitive dual band metamaterial absorber," *Optics letters*, vol. 36, no. 6, pp. 945–947, 2011.

[30] H. Li, L. H. Yuan, B. Zhou, X. P. Shen, Q. Cheng, and T. J. Cui, "Ultrathin multiband gigahertz metamaterial absorbers," *Journal of applied physics*, vol. 110, no. 1, 2011.

[31] J. W. Park, P. Van Tuong, J. Y. Rhee, K. W. Kim, W. H. Jang, E. H. Choi, L. Y. Chen, and Y. Lee, "Multi-band metamaterial absorber based on the arrangement of donut-type resonators," *Optics express*, vol. 21, no. 8, pp. 9691–9702, 2013.

[32] Y. J. Yoo, Y. J. Kim, P. Van Tuong, J. Y. Rhee, K. W. Kim, W. H. Jang, Y. Kim, H. Cheong, and Y. Lee, "Polarization-independent dual-band perfect absorber utilizing multiple magnetic resonances," *Optics express*, vol. 21, no. 26, pp. 32 484–32 490, 2013.

[33] Y. Cui, J. Xu, K. Hung Fung, Y. Jin, A. Kumar, S. He, and N. X. Fang, "A thin film broadband absorber based on multi-sized nanoantennas," *Applied Physics Letters*, vol. 99, no. 25, 2011.

[34] B. Zhang, Y. Zhao, Q. Hao, B. Kiraly, I.-C. Khoo, S. Chen, and T. J. Huang, "Polarization-independent dual-band infrared perfect absorber based on a metal-dielectric-metal elliptical nanodisk array," *Optics express*, vol. 19, no. 16, pp. 15 221–15 228, 2011.

[35] N. Landy, C. Bingham, T. Tyler, N. Jokerst, D. Smith, and W. Padilla, "Design, theory, and measurement of a polarization-insensitive absorber for terahertz imaging," *physical review B*, vol. 79, no. 12, p. 125104, 2009.

[36] Z. Xiong, L. Shang, J. Yang, L. Chen, J. Guo, Q. Liu, S. A. Danso, and G. Li, "Terahertz sensor with resonance enhancement based on square split-ring resonators," *IEEE Access*, vol. 9, pp. 59 211–59 221, 2021.

[37] P. Tuong, J. Park, J. Rhee, K. Kim, W. Jang, H. Cheong, and Y. Lee, "Polarization-insensitive and polarization-controlled dual-band absorption in metamaterials," *Applied Physics Letters*, vol. 102, no. 8, 2013.

[38] B. Zhu, Y. Feng, J. Zhao, C. Huang, and T. Jiang, "Switchable metamaterial reflector/absorber for different polarized electromagnetic waves," *Applied Physics Letters*, vol. 97, no. 5, 2010.

[39] B. Munk, "Frequency selective surfaces-theory and design, wiley," *New York*, 2000.

[40] P. Gay-Balmaz and O. J. Martin, "Electromagnetic resonances in individual and coupled split-ring resonators," *Journal of applied physics*, vol. 92, no. 5, pp. 2929–2936, 2002.

[41] J. D. Baena, J. Bonache, F. Martin, R. M. Sillero, F. Falcone, T. Lopetegi, M. A. Laso, J. Garcia-Garcia, I. Gil, M. F. Portillo *et al.*, "Equivalent-circuit models for split-ring resonators and complementary split-ring resonators coupled to planar transmission lines," *IEEE transactions on microwave theory and techniques*, vol. 53, no. 4, pp. 1451–1461, 2005.

[42] R. Marqués Sillero, F. Medina Mena, J. Martel Villagrán, and F. L. Mesa Ledesma, "Left-handed-media simulation and transmission of em waves in subwavelength split-ring-resonator-loaded metallic waveguides," *Physical Review Letters, 89 (18), 183901-1-183901-4.*, 2002.

[43] J. Naqui, M. Durán-Sindreu, and F. Martín, "Novel sensors based on the symmetry properties of split ring resonators (srrs)," *Sensors*, vol. 11, no. 8, pp. 7545–7553, 2011.

[44] J. B. Pendry, A. J. Holden, D. J. Robbins, and W. Stewart, "Magnetism from conductors and enhanced nonlinear phenomena," *IEEE transactions on microwave theory and techniques*, vol. 47, no. 11, pp. 2075–2084, 1999.

[45] D. R. Smith, W. J. Padilla, D. Vier, S. C. Nemat-Nasser, and S. Schultz, "Composite medium with simultaneously negative permeability and permittivity," *Physical review letters*, vol. 84, no. 18, p. 4184, 2000.

[46] R. A. Shelby, D. R. Smith, and S. Schultz, "Experimental verification of a negative index of refraction," *science*, vol. 292, no. 5514, pp. 77–79, 2001.

[47] J. Parsons, E. Hendry, J. Sambles, and W. Barnes, "Localized surface-plasmon resonances and negative refractive index in nanostructured electromagnetic metamaterials," *Physical Review B*, vol. 80, no. 24, p. 245117, 2009.

[48] V. G. Veselago, "The Electrodynamics of Substances with Simultaneously Negative Values of ε and μ," *Soviet Physics Uspekhi*, vol. 10, no. 4, pp. 509–514, Apr. 1968.

[49] J. B. Pendry, A. Holden, D. Robbins, and W. Stewart, "Low frequency plasmons in thin-wire structures," *Journal of Physics: Condensed Matter*, vol. 10, no. 22, p. 4785, 1998.

[50] J. B. Pendry, A. J. Holden, D. J. Robbins, and W. Stewart, "Magnetism from conductors and enhanced nonlinear phenomena," *IEEE transactions on microwave theory and techniques*, vol. 47, no. 11, pp. 2075–2084, 1999.

[51] D. R. Smith, W. J. Padilla, D. Vier, S. C. Nemat-Nasser, and S. Schultz, "Composite medium with simultaneously negative permeability and permittivity," *Physical review letters*, vol. 84, no. 18, p. 4184, 2000.

[52] J. Pendry, "Negative refraction," *Contemporary Physics*, vol. 45, no. 3, pp. 191–202, 2004. [Online]. Available: https://doi.org/10.1080/00107510410001667434

[53] D. R. Smith, J. B. Pendry, and M. C. K. Wiltshire, "Metamaterials and negative refractive index," *Science*, vol. 305, no. 5685, pp. 788–792, 2004. [Online]. Available: https://www.science.org/doi/abs/10.1126/science.1096796

[54] B.-I. Wu, W. Wang, J. Pacheco, X. Chen, T. M. Grzegorczyk, and J. Kong, "A study of using metamaterials as antenna substrate to enhance gain," *Progress in electromagnetics research*, vol. 51, pp. 295–328, 2005.

[55] D. R. Smith, W. J. Padilla, D. Vier, S. C. Nemat-Nasser, and S. Schultz, "Composite medium with simultaneously negative permeability and permittivity," *Physical review letters*, vol. 84, no. 18, p. 4184, 2000.

[56] G. T. Ruck, D. E. Barrick, W. D. Stuart, and C. K. Krichbaum, "Radar cross section handbook," *(No Title)*, 1970.

[57] K. L. Ford and B. Chambers, "Improvement in the low frequency performance of geometric transition radar absorbers using square loop impedance layers," *IEEE Transactions on Antennas and Propagation*, vol. 56, no. 1, pp. 133–141, 2008.

[58] D. Holtby, K. Ford, and B. Chambers, "Geometric transition radar absorbing material loaded with a binary frequency selective surface," *IET radar, sonar & navigation*, vol. 5, no. 4, pp. 483–488, 2011.

[59] G. Manara, A. Monorchio, and R. Mittra, "Frequency selective surface design based on genetic algorithm," *Electronics Letters*, vol. 35, no. 17, pp. 1400–1401, 1999.

[60] Y. P. Lee, J. Y. Rhee, Y. J. Yoo, and K. W. Kim, *Metamaterials for perfect absorption*. Springer, 2016.

[61] O. Kazmina, V. Suslyaev, M. Dushkina, and B. Semukhin, "Characterization of porous glass-ceramic material as absorber of electromagnetic radiation," in *IOP Conference Series: Materials Science and Engineering*, vol. 81, no. 1. IOP Publishing, 2015, p. 012036.

[62] G. Li, T. Xie, S. Yang, J. Jin, and J. Jiang, "Microwave absorption enhancement of porous carbon fibers compared with carbon nanofibers," *The Journal of Physical Chemistry C*, vol. 116, no. 16, pp. 9196–9201, 2012.

[63] G. P. Williams, "Filling the thz gap—high power sources and applications," *Reports on Progress in Physics*, vol. 69, no. 2, p. 301, 2005.

[64] S. Borri, P. Patimisco, A. Sampaolo, H. Beere, D. Ritchie, M. Vitiello, G. Scamarcio, and V. Spagnolo, "Terahertz quartz enhanced photo-acoustic sensor," *Applied Physics Letters*, vol. 103, no. 2, 2013.

[65] H.-T. Chen, W. J. Padilla, J. M. Zide, A. C. Gossard, A. J. Taylor, and R. D. Averitt, "Active terahertz metamaterial devices," *Nature*, vol. 444, no. 7119, pp. 597–600, 2006.

[66] Y. P. Lee, J. Y. Rhee, Y. J. Yoo, K. W. Kim, Y. P. Lee, J. Y. Rhee, Y. J. Yoo, and K. W. Kim, "Mmpas operating in different frequency ranges," *Metamaterials for Perfect Absorption*, pp. 55–98, 2016.

[67] J. B. Pendry, A. Holden, D. Robbins, and W. Stewart, "Low frequency plasmons in thin-wire structures," *Journal of Physics: Condensed Matter*, vol. 10, no. 22, p. 4785, 1998.

[68] S. Zouhdi, A. Sihvola, and A. P. Vinogradov, *Metamaterials and plasmonics: fundamentals, modelling, applications*. Springer Science & Business Media, 2008.

[69] M. Wiltshire, J. Pendry, and J. Hajnal, "Chiral swiss rolls show a negative refractive index," *Journal of Physics: Condensed Matter*, vol. 21, no. 29, p. 292201, 2009.

[70] G. Dolling, C. Enkrich, M. Wegener, J. Zhou, C. M. Soukoulis, and S. Linden, "Cut-wire pairs and plate pairs as magnetic atoms for optical metamaterials," *Optics letters*, vol. 30, no. 23, pp. 3198–3200, 2005.

[71] C. Imhof and R. Zengerle, "Pairs of metallic crosses as a left-handed metamaterial with improved polarization properties," *Optics express*, vol. 14, no. 18, pp. 8257–8262, 2006.

[72] B. Bandyopadhyay, S. Bhattacharya, R. K. Jaiswal, M. Saikia, and K. V. Srivastava, "Wideband rcs reduction of a linear patch antenna array using amc metasurface for stealth applications," *IEEE Access*, vol. 11, pp. 127 458–127 467, 2023.

[73] J. Kim, K. Han, and J. W. Hahn, "Selective dual-band metamaterial perfect absorber for infrared stealth technology," *Scientific reports*, vol. 7, no. 1, p. 6740, 2017.

[74] H. Zheng, X. Jin, J. Park, Y. Lu, J. Y. Rhee, W. Jang, H. Cheong, and Y. Lee, "Tunable dual-band perfect absorbers based on extraordinary optical transmission and fabry-perot cavity resonance," *Optics express*, vol. 20, no. 21, pp. 24 002–24 009, 2012.

[75] W. Li, T. Wu, W. Wang, J. Guan, and P. Zhai, "Integrating non-planar metamaterials with magnetic absorbing materials to yield ultra-broadband microwave hybrid absorbers," *Applied Physics Letters*, vol. 104, no. 2, 2014.

[76] M. Schussler, A. Fleckenstein, J. Freese, and R. Jakoby, "Left-handed metamaterials based on split ring resonators for microstrip applications," in *33rd European Microwave Conference Proceedings (IEEE Cat. No. 03EX723C)*, vol. 3. IEEE, 2003, pp. 1119–1122.

[77] F. Martın, J. Bonache, F. a. Falcone, M. Sorolla, and R. Marqués, "Split ring resonator-based left-handed coplanar waveguide," *Applied Physics Letters*, vol. 83, no. 22, pp. 4652–4654, 2003.

[78] F. Martin, F. Falcone, J. Bonache, R. Marqués, and M. Sorolla, "Miniaturized coplanar waveguide stop band filters based on multiple tuned split ring resonators," *IEEE microwave and wireless components letters*, vol. 13, no. 12, pp. 511–513, 2003.

[79] F. Falcone, F. Martín, J. Bonache, R. Marqués, T. Lopetegi, and M. Sorolla, "Left handed coplanar waveguide band pass filters based on bi-layer split ring resonators," *IEEE Microwave and Wireless Components Letters*, vol. 14, no. 1, pp. 10–12, 2004.

[80] K. Srinivasan, N. B. Ali, Y. Trabelsi, M. M. Rajan, and M. Kanzari, "Design of a modified single-negative metamaterial structure for sensing application," *Optik*, vol. 180, pp. 924–931, 2019.

[81] N. Ramanujam, K. J. Wilson, P. Mahalakshmi, and S. A. Taya, "Analysis of photonic band gap in photonic crystal with epsilon negative and double negative materials," *Optik*, vol. 183, pp. 203–210, 2019.

[82] C. Sabah, "Novel, dual band, single and double negative metamaterials: nonconcentric delta loop resonators," *Progress In Electromagnetics Research B*, vol. 25, pp. 225–239, 2010.

[83] V. Özkan, A. Yapıcı, M. Karaaslan, and O. Akgöl, "Investigation of electromagnetic properties of glass-fiber reinforced epoxy composites containing pan nanofibers with mwcnt/graphene additive," 2019.

[84] Y. I. Abdulkarim, L. Deng, O. Altıntaş, E. Ünal, and M. Karaaslan, "Metamaterial absorber sensor design by incorporating swastika shaped resonator to determination of the liquid chemicals depending on electrical characteristics," *Physica E: Low-dimensional systems and Nanostructures*, vol. 114, p. 113593, 2019.

[85] O. Akgol, M. Bağmancı, M. Karaaslan, and E. Ünal, "Broad band ma-based on three-type resonator having resistor for microwave energy harvesting," *Journal of Microwave Power and Electromagnetic Energy*, vol. 51, no. 2, pp. 134–149, 2017.

[86] J. García-García, F. Martin, F. Falcone, J. Bonache, I. Gil, T. Lopetegi, M. A. Laso, M. Sorolla, and R. Marques, "Spurious passband suppression in microstrip coupled line band pass filters by means of split ring resonators," *IEEE Microwave and Wireless Components Letters*, vol. 14, no. 9, pp. 416–418, 2004.

[87] F. Falcone, T. Lopetegi, J. D. Baena, R. Marqués, F. Martín, and M. Sorolla, "Effective negative-/spl epsiv/stopband microstrip lines based on complementary split ring resonators," *IEEE microwave and wireless components letters*, vol. 14, no. 6, pp. 280–282, 2004.

[88] N. Engheta, "Thin absorbing screens using metamaterial surfaces," in *IEEE Antennas and Propagation Society International Symposium (IEEE Cat. No. 02CH37313)*, vol. 2. IEEE, 2002, pp. 392–395.

[89] H. Tao, N. I. Landy, C. M. Bingham, X. Zhang, R. D. Averitt, and W. J. Padilla, "A metamaterial absorber for the terahertz regime: design, fabrication and characterization," *Optics express*, vol. 16, no. 10, pp. 7181–7188, 2008.

[90] D. Y. Shchegolkov, A. Azad, J. O'hara, and E. Simakov, "Perfect subwavelength fishnetlike metamaterial-based film terahertz absorbers," *Physical review B*, vol. 82, no. 20, p. 205117, 2010.

[91] J. Grant, Y. Ma, S. Saha, L. Lok, A. Khalid, and D. Cumming, "Polarization insensitive terahertz metamaterial absorber," *Optics letters*, vol. 36, no. 8, pp. 1524–1526, 2011.

[92] X. Shen, Y. Yang, Y. Zang, J. Gu, J. Han, W. Zhang, and T. Jun Cui, "Triple-band terahertz metamaterial absorber: Design, experiment, and physical interpretation," *Applied Physics Letters*, vol. 101, no. 15, 2012.

[93] W. Qin, J. Wu, M. Yu, and S. Pan, "Dual-band terahertz metamaterial absorbers using two types of conventional frequency selective surface elements,"," *Terahertz Science and Technology*, vol. 5, pp. 169–174, 2012.

[94] H. Tao, C. Bingham, A. Strikwerda, D. Pilon, D. Shrekenhamer, N. Landy, K. Fan, X. Zhang, W. Padilla, and R. Averitt, "Highly flexible wide angle of incidence terahertz metamaterial absorber: Design, fabrication, and characterization," *physical review B*, vol. 78, no. 24, p. 241103, 2008.

[95] M. Diem, T. Koschny, and C. M. Soukoulis, "Wide-angle perfect absorber/thermal emitter in the terahertz regime," *Physical Review B*, vol. 79, no. 3, p. 033101, 2009.

[96] B. A. Munk, *Frequency selective surfaces: theory and design*. John Wiley & Sons, 2005.

[97] J. Hao, J. Wang, X. Liu, W. J. Padilla, L. Zhou, and M. Qiu, "High performance optical absorber based on a plasmonic metamaterial," *Applied Physics Letters*, vol. 96, no. 25, 2010.

[98] L. Luo, I. Chatzakis, J. Wang, F. B. Niesler, M. Wegener, T. Koschny, and C. M. Soukoulis, "Broadband terahertz generation from metamaterials," *Nature communications*, vol. 5, no. 1, p. 3055, 2014.

[99] B. Reinhard, K. M. Schmitt, V. Wollrab, J. Neu, R. Beigang, and M. Rahm, "Metamaterial near-field sensor for deep-subwavelength thickness measurements and sensitive refractometry in the terahertz frequency range," *Applied Physics Letters*, vol. 100, no. 22, 2012.

[100] Z. Yong, S. Zhang, C. Gong, and S. He, "Narrow band perfect absorber for maximum localized magnetic and electric field enhancement and sensing applications," *Scientific reports*, vol. 6, no. 1, p. 24063, 2016.

[101] C. Wu, B. Neuner III, J. John, A. Milder, B. Zollars, S. Savoy, and G. Shvets, "Metamaterial-based integrated plasmonic absorber/emitter for solar thermo-photovoltaic systems," *Journal of Optics*, vol. 14, no. 2, p. 024005, 2012.

[102] P. Bermel, M. Ghebrebrhan, M. Harradon, Y. X. Yeng, I. Celanovic, J. D. Joannopoulos, and M. Soljacic, "Tailoring photonic metamaterial resonances for thermal radiation," *Nanoscale research letters*, vol. 6, pp. 1–5, 2011.

[103] A. Paulish, P. Zagubisalo, and S. Kuznetsov, "38th int. conf. infrared, millimeter, and terahertz waves (irmmw-thz)," 2013.

[104] B. Casse, W. Lu, Y. Huang, E. Gultepe, L. Menon, and S. Sridhar, "Super-resolution imaging using a three-dimensional metamaterials nanolens," *Applied Physics Letters*, vol. 96, no. 2, 2010.

[105] M. Gil, J. Bonache, and F. Martin, "Metamaterial filters: A review," *Metamaterials*, vol. 2, no. 4, pp. 186–197, 2008.

[106] R. Zhang, F. Ding, X. Yuan, and M. Chen, "Influence of spatial correlation function on characteristics of wideband electromagnetic wave absorbers with chaotic surface," *Chinese Physics Letters*, vol. 39, no. 9, p. 094101, 2022.

[107] Y. Lee, P. Tuong, H. Zheng, J. Rhee, and W. Jang, "An application of metamaterials: Perfect absorbers," *Journal of the Korean Physical Society*, vol. 60, pp. 1203–1206, 2012.

[108] P. Yu, L. V. Besteiro, J. Wu, Y. Huang, Y. Wang, A. O. Govorov, and Z. Wang, "Metamaterial perfect absorber with unabated size-independent absorption," *Optics Express*, vol. 26, no. 16, pp. 20 471–20 480, 2018.

[109] P. Yu, J. Wu, E. Ashalley, A. Govorov, and Z. Wang, "Dual-band absorber for multispectral plasmon-enhanced infrared photodetection," *Journal of Physics D: Applied Physics*, vol. 49, no. 36, p. 365101, 2016.

[110] P. Pitchappa, C. P. Ho, P. Kropelnicki, N. Singh, D.-L. Kwong, and C. Lee, "Dual band complementary metamaterial absorber in near infrared region," *Journal of Applied Physics*, vol. 115, no. 19, 2014.

[111] S. Bhattacharyya, S. Ghosh, and K. Vaibhav Srivastava, "Triple band polarization-independent metamaterial absorber with bandwidth enhancement at x-band," *Journal of Applied Physics*, vol. 114, no. 9, 2013.

[112] J. Chen, X. Huang, G. Zerihun, Z. Hu, S. Wang, G. Wang, X. Hu, and M. Liu, "Polarization-independent, thin, broadband metamaterial absorber using double-circle rings loaded with lumped resistances," *Journal of Electronic Materials*, vol. 44, pp. 4269–4274, 2015.

[113] G. Dayal and S. A. Ramakrishna, "Design of multi-band metamaterial perfect absorbers with stacked metal–dielectric disks," *Journal of Optics*, vol. 15, no. 5, p. 055106, 2013.

[114] Y. Q. Ye, Y. Jin, and S. He, "Omnidirectional, polarization-insensitive and broadband thin absorber in the terahertz regime," *JOSA B*, vol. 27, no. 3, pp. 498–504, 2010.

[115] S. Gu, J. Barrett, T. Hand, B.-I. Popa, and S. Cummer, "A broadband low-reflection metamaterial absorber," *Journal of Applied Physics*, vol. 108, no. 6, 2010.

[116] H. Wang, V. P. Sivan, A. Mitchell, G. Rosengarten, P. Phelan, and L. Wang, "Highly efficient selective metamaterial absorber for high-temperature solar

thermal energy harvesting," *Solar Energy Materials and Solar Cells*, vol. 137, pp. 235–242, 2015.

[117] A. E. Culhaoglu, A. V. Osipov, and P. Russer, "Mono-and bistatic scattering reduction by a metamaterial low reflection coating," *IEEE transactions on antennas and propagation*, vol. 61, no. 1, pp. 462–466, 2012.

[118] S. Guddala, R. Kumar, and S. A. Ramakrishna, "Thermally induced nonlinear optical absorption in metamaterial perfect absorbers," *Applied Physics Letters*, vol. 106, no. 11, 2015.

[119] C. M. Watts, X. Liu, and W. J. Padilla, "Metamaterial electromagnetic wave absorbers," *Advanced materials*, vol. 24, no. 23, pp. OP98–OP120, 2012.

[120] W. Zhu, X. Zhao, B. Gong, L. Liu, and B. Su, "Optical metamaterial absorber based on leaf-shaped cells," *Applied Physics A*, vol. 102, pp. 147–151, 2011.

[121] O. Gordon, Y.-J. Huang, G.-J. Wen, J. Li, J.-P. Zhong, P. Wang, Y.-H. Sun, and W.-R. Zhu, "Metamaterial absorbers realized in an x-band rectangular waveguide," *Chinese Physics B*, vol. 21, no. 11, p. 117801, 2012.

[122] W. Zhu, I. D. Rukhlenko, and M. Premaratne, "Graphene metamaterial for optical reflection modulation," *Applied Physics Letters*, vol. 102, no. 24, 2013.

[123] Y. Ra'di, C. R. Simovski, and S. A. Tretyakov, "Thin perfect absorbers for electromagnetic waves: theory, design, and realizations," *Physical Review Applied*, vol. 3, no. 3, p. 037001, 2015.

[124] Y. Ji, C. Tang, N. Xie, J. Chen, P. Gu, C. Peng, and B. Liu, "High-performance metamaterial sensors based on strong coupling between surface

plasmon polaritons and magnetic plasmon resonances," *Results in Physics*, vol. 14, p. 102397, 2019.

[125] C. Cen, Z. Chen, D. Xu, L. Jiang, X. Chen, Z. Yi, P. Wu, G. Li, and Y. Yi, "High quality factor, high sensitivity metamaterial graphene—perfect absorber based on critical coupling theory and impedance matching," *Nanomaterials*, vol. 10, no. 1, p. 95, 2020.

[126] N. P. Sergeant, O. Pincon, M. Agrawal, and P. Peumans, "Design of wide-angle solar-selective absorbers using aperiodic metal-dielectric stacks," *Optics express*, vol. 17, no. 25, pp. 22 800–22 812, 2009.

[127] J. Li, X. Chen, Z. Yi, H. Yang, Y. Tang, Y. Yi, W. Yao, J. Wang, and Y. Yi, "Broadband solar energy absorber based on monolayer molybdenum disulfide using tungsten elliptical arrays," *Materials Today Energy*, vol. 16, p. 100390, 2020.

[128] J. Li, Z. Chen, H. Yang, Z. Yi, X. Chen, W. Yao, T. Duan, P. Wu, G. Li, and Y. Yi, "Tunable broadband solar energy absorber based on monolayer transition metal dichalcogenides materials using au nanocubes," *Nanomaterials*, vol. 10, no. 2, p. 257, 2020.

[129] L. Cai, Q. Li, J. Yu, H. Luo, K. Du, and M. Qiu, "Simultaneous single-peak and narrowband thermal emission enabled by hybrid metal-polar dielectric structures," *Applied Physics Letters*, vol. 115, no. 9, 2019.

[130] D. Wu, C. Liu, Z. Xu, Y. Liu, Z. Yu, L. Yu, L. Chen, R. Li, R. Ma, and H. Ye, "The design of ultra-broadband selective near-perfect absorber based on photonic structures to achieve near-ideal daytime radiative cooling," *Materials & Design*, vol. 139, pp. 104–111, 2018.

[131] J. Wang, C. Fan, P. Ding, J. He, Y. Cheng, W. Hu, G. Cai, E. Liang, and Q. Xue, "Tunable broad-band perfect absorber by exciting of multiple plasmon resonances at optical frequency," *Optics express*, vol. 20, no. 14, pp. 14 871–14 878, 2012.

[132] Y.-L. Liao and Y. Zhao, "A wide-angle broadband polarization-dependent absorber with stacked metal-dielectric grating," *Optics Communications*, vol. 370, pp. 245–249, 2016.

[133] ——, "Absorption manipulation in a narrowband infrared absorber based on the hybridization of gap plasmon and fabry-perot resonance," *Plasmonics*, vol. 10, pp. 1219–1223, 2015.

[134] Y. Wang, Z. Chen, D. Xu, Z. Yi, X. Chen, J. Chen, Y. Tang, P. Wu, G. Li, and Y. Yi, "Triple-band perfect metamaterial absorber with good operating angle polarization tolerance based on split ring arrays," *Results in Physics*, vol. 16, p. 102951, 2020.

[135] F. Qin, Z. Chen, X. Chen, Z. Yi, W. Yao, T. Duan, P. Wu, H. Yang, G. Li, and Y. Yi, "A tunable triple-band near-infrared metamaterial absorber based on au nano-cuboids array," *Nanomaterials*, vol. 10, no. 2, p. 207, 2020.

[136] P. Wu, Z. Chen, H. Jile, C. Zhang, D. Xu, and L. Lv, "An infrared perfect absorber based on metal-dielectric-metal multi-layer films with nanocircle holes arrays," *Results in Physics*, vol. 16, p. 102952, 2020.

[137] B. Zhu, C. Huang, Y. Feng, J. Zhao, and T. Jiang, "Dual band switchable metamaterial electromagnetic absorber," *Progress In Electromagnetics Research B*, vol. 24, pp. 121–129, 2010.

[138] B. Zhu, Y. Feng, J. Zhao, C. Huang, Z. Wang, and T. Jiang, "Polarization modulation by tunable electromagnetic metamaterial reflector/absorber," *Optics express*, vol. 18, no. 22, pp. 23 196–23 203, 2010.

[139] A. S. Mayorov, R. V. Gorbachev, S. V. Morozov, L. Britnell, R. Jalil, L. A. Ponomarenko, P. Blake, K. S. Novoselov, K. Watanabe, T. Taniguchi *et al.*, "Micrometer-scale ballistic transport in encapsulated graphene at room temperature," *Nano letters*, vol. 11, no. 6, pp. 2396–2399, 2011.

[140] C. Lee, X. Wei, J. W. Kysar, and J. Hone, "Measurement of the elastic properties and intrinsic strength of monolayer graphene," *science*, vol. 321, no. 5887, pp. 385–388, 2008.

[141] F. Liu, P. Ming, and J. Li, "Ab initio calculation of ideal strength and phonon instability of graphene under tension," *Physical Review B*, vol. 76, no. 6, p. 064120, 2007.

[142] A. A. Balandin, "Thermal properties of graphene and nanostructured carbon materials," *Nature materials*, vol. 10, no. 8, pp. 569–581, 2011.

[143] J. S. Bunch, S. S. Verbridge, J. S. Alden, A. M. Van Der Zande, J. M. Parpia, H. G. Craighead, and P. L. McEuen, "Impermeable atomic membranes from graphene sheets," *Nano letters*, vol. 8, no. 8, pp. 2458–2462, 2008.

[144] J. Moser, A. Barreiro, and A. Bachtold, "Current-induced cleaning of graphene," *Applied Physics Letters*, vol. 91, no. 16, 2007.

[145] D. C. Elias, R. R. Nair, T. Mohiuddin, S. Morozov, P. Blake, M. Halsall, A. C. Ferrari, D. Boukhvalov, M. Katsnelson, A. Geim *et al.*, "Control of graphene's properties by reversible hydrogenation: evidence for graphane," *Science*, vol. 323, no. 5914, pp. 610–613, 2009.

[146] K. P. Loh, Q. Bao, P. K. Ang, and J. Yang, "The chemistry of graphene," *Journal of Materials Chemistry*, vol. 20, no. 12, pp. 2277–2289, 2010.

[147] R. R. Nair, W. Ren, R. Jalil, I. Riaz, V. G. Kravets, L. Britnell, P. Blake, F. Schedin, A. S. Mayorov, S. Yuan *et al.*, "Fluorographene: a two-dimensional counterpart of teflon," *small*, vol. 6, no. 24, pp. 2877–2884, 2010.

[148] K. S. Novoselov, A. K. Geim, S. V. Morozov, D.-e. Jiang, Y. Zhang, S. V. Dubonos, I. V. Grigorieva, and A. A. Firsov, "Electric field effect in atomically thin carbon films," *science*, vol. 306, no. 5696, pp. 666–669, 2004.

[149] C. R. Dean, A. F. Young, I. Meric, C. Lee, L. Wang, S. Sorgenfrei, K. Watanabe, T. Taniguchi, P. Kim, K. L. Shepard *et al.*, "Boron nitride substrates for high-quality graphene electronics," *Nature nanotechnology*, vol. 5, no. 10, pp. 722–726, 2010.

[150] K. S. Novoselov, D. Jiang, F. Schedin, T. Booth, V. Khotkevich, S. Morozov, and A. K. Geim, "Two-dimensional atomic crystals," *Proceedings of the National Academy of Sciences*, vol. 102, no. 30, pp. 10 451–10 453, 2005.

[151] A. K. Geim, "Nobel lecture: Random walk to graphene," *Reviews of Modern Physics*, vol. 83, no. 3, p. 851, 2011.

[152] K. S. Novoselov, "Graphene: materials in the flatland (nobel lecture)," *Angewandte Chemie International Edition*, vol. 50, no. 31, pp. 6986–7002, 2011.

[153] P. Blake, P. D. Brimicombe, R. R. Nair, T. J. Booth, D. Jiang, F. Schedin, L. A. Ponomarenko, S. V. Morozov, H. F. Gleeson, E. W. Hill *et al.*, "Graphene-based liquid crystal device," *Nano letters*, vol. 8, no. 6, pp. 1704–1708, 2008.

[154] Y. Hernandez, V. Nicolosi, M. Lotya, F. M. Blighe, Z. Sun, S. De, I. T. McGovern, B. Holland, M. Byrne, Y. K. Gun'Ko *et al.*, "High-yield production of graphene by liquid-phase exfoliation of graphite," *Nature nanotechnology*, vol. 3, no. 9, pp. 563–568, 2008.

[155] D. R. Dreyer, R. S. Ruoff, and C. W. Bielawski, "From conception to realization: an historial account of graphene and some perspectives for its future," *Angewandte Chemie International Edition*, vol. 49, no. 49, pp. 9336–9344, 2010.

[156] H. C. Schniepp, J.-L. Li, M. J. McAllister, H. Sai, M. Herrera-Alonso, D. H. Adamson, R. K. Prud'homme, R. Car, D. A. Saville, and I. A. Aksay, "Functionalized single graphene sheets derived from splitting graphite oxide," *The journal of physical chemistry B*, vol. 110, no. 17, pp. 8535–8539, 2006.

[157] L. Jiao, L. Zhang, X. Wang, G. Diankov, and H. Dai, "Narrow graphene nanoribbons from carbon nanotubes," *Nature*, vol. 458, no. 7240, pp. 877–880, 2009.

[158] D. V. Kosynkin, A. L. Higginbotham, A. Sinitskii, J. R. Lomeda, A. Dimiev, B. K. Price, and J. M. Tour, "Longitudinal unzipping of carbon nanotubes to form graphene nanoribbons," *Nature*, vol. 458, no. 7240, pp. 872–876, 2009.

[159] M. Segal, "Selling graphene by the ton," *Nature nanotechnology*, vol. 4, no. 10, pp. 612–614, 2009.

[160] X. Li, W. Cai, J. An, S. Kim, J. Nah, D. Yang, R. Piner, A. Velamakanni, I. Jung, E. Tutuc *et al.*, "Large-area synthesis of high-quality and uniform graphene films on copper foils," *science*, vol. 324, no. 5932, pp. 1312–1314, 2009.

[161] S. Bae, H. Kim, Y. Lee, X. Xu, J.-S. Park, Y. Zheng, J. Balakrishnan, T. Lei, H. Ri Kim, Y. I. Song *et al.*, "Roll-to-roll production of 30-inch graphene films for transparent electrodes," *Nature nanotechnology*, vol. 5, no. 8, pp. 574–578, 2010.

[162] I. Forbeaux, J.-M. Themlin, and J.-M. Debever, "Heteroepitaxial graphite on 6 h- sic (0001): Interface formation through conduction-band electronic structure," *Physical Review B*, vol. 58, no. 24, p. 16396, 1998.

[163] C. Berger, Z. Song, T. Li, X. Li, A. Y. Ogbazghi, R. Feng, Z. Dai, A. N. Marchenkov, E. H. Conrad, P. N. First *et al.*, "Ultrathin epitaxial graphite: 2d electron gas properties and a route toward graphene-based nanoelectronics," *The Journal of Physical Chemistry B*, vol. 108, no. 52, pp. 19 912–19 916, 2004.

[164] T. Ohta, A. Bostwick, T. Seyller, K. Horn, and E. Rotenberg, "Controlling the electronic structure of bilayer graphene," *Science*, vol. 313, no. 5789, pp. 951–954, 2006.

[165] C. Virojanadara, M. Syväjarvi, R. Yakimova, L. Johansson, A. Zakharov, and T. Balasubramanian, "Homogeneous large-area graphene layer growth on 6 h-sic (0001)," *Physical Review B*, vol. 78, no. 24, p. 245403, 2008.

[166] Y.-M. Lin, C. Dimitrakopoulos, K. A. Jenkins, D. B. Farmer, H.-Y. Chiu, A. Grill, and P. Avouris, "100-ghz transistors from wafer-scale epitaxial graphene," *Science*, vol. 327, no. 5966, pp. 662–662, 2010.

[167] A. Tzalenchuk, S. Lara-Avila, A. Kalaboukhov, S. Paolillo, M. Syväjärvi, R. Yakimova, O. Kazakova, T. Janssen, V. Fal'Ko, and S. Kubatkin, "Towards a quantum resistance standard based on epitaxial graphene," *Nature nanotechnology*, vol. 5, no. 3, pp. 186–189, 2010.

[168] J. Cai, P. Ruffieux, R. Jaafar, M. Bieri, T. Braun, S. Blankenburg, M. Muoth, A. P. Seitsonen, M. Saleh, X. Feng *et al.*, "Atomically precise bottom-up fabrication of graphene nanoribbons," *Nature*, vol. 466, no. 7305, pp. 470–473, 2010.

[169] J. Hackley, D. Ali, J. DiPasquale, J. Demaree, and C. Richardson, "Graphitic carbon growth on si (111) using solid source molecular beam epitaxy," *Applied Physics Letters*, vol. 95, no. 13, 2009.

[170] S. Dhar, A. R. Barman, G. Ni, X. Wang, X. Xu, Y. Zheng, S. Tripathy, A. Ariando, A. Rusydi, K. Loh *et al.*, "A new route to graphene layers by selective laser ablation," *Aip Advances*, vol. 1, no. 2, 2011.

[171] K. Novoselov and V. Fal, "Ko, l. colombo, pr gellert, mg schwab and k. kim," *Nature*, vol. 490, no. 7419, pp. 192–200, 2012.

[172] L. Liao, Y.-C. Lin, M. Bao, R. Cheng, J. Bai, Y. Liu, Y. Qu, K. L. Wang, Y. Huang, and X. Duan, "High-speed graphene transistors with a self-aligned nanowire gate," *Nature*, vol. 467, no. 7313, pp. 305–308, 2010.

[173] L. Liao, J. Bai, R. Cheng, Y.-C. Lin, S. Jiang, Y. Qu, Y. Huang, and X. Duan, "Sub-100 nm channel length graphene transistors," *Nano letters*, vol. 10, no. 10, pp. 3952–3956, 2010.

[174] M. Y. Han, B. Özyilmaz, Y. Zhang, and P. Kim, "Energy band-gap engineering of graphene nanoribbons," *Physical review letters*, vol. 98, no. 20, p. 206805, 2007.

[175] L. A. Ponomarenko, F. Schedin, M. I. Katsnelson, R. Yang, E. W. Hill, K. S. Novoselov, and A. K. Geim, "Chaotic dirac billiard in graphene quantum dots," *Science*, vol. 320, no. 5874, pp. 356–358, 2008.

[176] C. Stampfer, E. Schurtenberger, F. Molitor, J. Guttinger, T. Ihn, and K. Ensslin, "Tunable graphene single electron transistor," *Nano letters*, vol. 8, no. 8, pp. 2378–2383, 2008.

[177] J. B. Oostinga, H. B. Heersche, X. Liu, A. F. Morpurgo, and L. M. Vandersypen, "Gate-induced insulating state in bilayer graphene devices," *Nature materials*, vol. 7, no. 2, pp. 151–157, 2008.

[178] Z. Li, E. A. Henriksen, Z. Jiang, Z. Hao, M. C. Martin, P. Kim, H. L. Stormer, and D. N. Basov, "Dirac charge dynamics in graphene by infrared spectroscopy," *Nature physics*, vol. 4, no. 7, pp. 532–535, 2008.

[179] X. Liu, D. Du, and G. Mourou, "Laser ablation and micromachining with ultrashort laser pulses," *IEEE journal of quantum electronics*, vol. 33, no. 10, pp. 1706–1716, 1997.

[180] W. Drexler, U. Morgner, F. Kärtner, C. Pitris, S. Boppart, X. Li, E. Ippen, and J. Fujimoto, "In vivo ultrahigh-resolution optical coherence tomography," *Optics letters*, vol. 24, no. 17, pp. 1221–1223, 1999.

[181] W. Tan, C. Su, R. Knize, G. Xie, L. Li, and D. Tang, "Mode locking of ceramic nd: yttrium aluminum garnet with graphene as a saturable absorber," *Applied Physics Letters*, vol. 96, no. 3, 2010.

[182] E. De Souza, M. Nuss, W. Knox, and D. Miller, "Wavelength-division multiplexing with femtosecond pulses," *Optics letters*, vol. 20, no. 10, pp. 1166–1168, 1995.

[183] V. Gusynin, S. Sharapov, and J. Carbotte, "Magneto-optical conductivity in graphene," *Journal of Physics: Condensed Matter*, vol. 19, no. 2, p. 026222, 2006.

[184] ——, "Sum rules for the optical and hall conductivity in graphene," *Physical Review B*, vol. 75, no. 16, p. 165407, 2007.

[185] ——, "On the universal ac optical background in graphene," *New Journal of Physics*, vol. 11, no. 9, p. 095013, 2009.

[186] G. W. Hanson, "Dyadic green's functions and guided surface waves for a surface conductivity model of graphene," *Journal of Applied Physics*, vol. 103, no. 6, 2008.

[187] K. S. Novoselov, A. K. Geim, S. V. Morozov, D. Jiang, M. I. Katsnelson, I. V. Grigorieva, S. Dubonos, and Firsov, "Two-dimensional gas of massless dirac fermions in graphene," *nature*, vol. 438, no. 7065, pp. 197–200, 2005.

[188] J.-S. Gómez-Díaz and J. Perruisseau-Carrier, "Graphene-based plasmonic switches at near infrared frequencies," *Optics express*, vol. 21, no. 13, pp. 15 490–15 504, 2013.

[189] B. Ferguson and X.-C. Zhang, "Materials for terahertz science and technology," *Nature materials*, vol. 1, no. 1, pp. 26–33, 2002.

[190] H. Tao, W. J. Padilla, X. Zhang, and R. D. Averitt, "Recent progress in electromagnetic metamaterial devices for terahertz applications," *IEEE Journal of Selected Topics in Quantum Electronics*, vol. 17, no. 1, pp. 92–101, 2010.

[191] T. Kleine-Ostmann, P. Dawson, K. Pierz, G. Hein, and M. Koch, "Room-temperature operation of an electrically driven terahertz modulator," *Applied physics letters*, vol. 84, no. 18, pp. 3555–3557, 2004.

[192] E. B. Song, B. Lian, S. Min Kim, S. Lee, T.-K. Chung, M. Wang, C. Zeng, G. Xu, K. Wong, Y. Zhou *et al.*, "Robust bi-stable memory operation

in single-layer graphene ferroelectric memory," *Applied Physics Letters*, vol. 99, no. 4, 2011.

[193] H.-T. Chen, W. J. Padilla, M. J. Cich, A. K. Azad, R. D. Averitt, and A. J. Taylor, "A metamaterial solid-state terahertz phase modulator," *Nature photonics*, vol. 3, no. 3, pp. 148–151, 2009.

[194] D. Shrekenhamer, S. Rout, A. C. Strikwerda, C. Bingham, R. D. Averitt, S. Sonkusale, and W. J. Padilla, "High speed terahertz modulation from metamaterials with embedded high electron mobility transistors," *Optics express*, vol. 19, no. 10, pp. 9968–9975, 2011.

[195] L. Ju, B. Geng, J. Horng, C. Girit, M. Martin, Z. Hao, H. A. Bechtel, X. Liang, A. Zettl, Y. R. Shen *et al.*, "Graphene plasmonics for tunable terahertz metamaterials," *Nature nanotechnology*, vol. 6, no. 10, pp. 630–634, 2011.

[196] A. Das, S. Pisana, B. Chakraborty, S. Piscanec, S. K. Saha, U. V. Waghmare, K. S. Novoselov, H. R. Krishnamurthy, A. K. Geim, A. C. Ferrari *et al.*, "Monitoring dopants by raman scattering in an electrochemically top-gated graphene transistor," *Nature nanotechnology*, vol. 3, no. 4, pp. 210–215, 2008.

[197] D. K. Efetov and P. Kim, "Controlling electron-phonon interactions in graphene at ultrahigh carrier densities," *Physical review letters*, vol. 105, no. 25, p. 256805, 2010.

[198] H. Wang, Y. Wu, C. Cong, J. Shang, and T. Yu, "Hysteresis of electronic transport in graphene transistors," *ACS nano*, vol. 4, no. 12, pp. 7221–7228, 2010.

[199] T. J. Echtermeyer, M. C. Lemme, M. Baus, B. N. Szafranek, A. K. Geim, and H. Kurz, "Nonvolatile switching in graphene field-effect devices," *IEEE Electron Device Letters*, vol. 29, no. 8, pp. 952–954, 2008.

[200] H. Y. Jeong, J. Y. Kim, J. W. Kim, J. O. Hwang, J.-E. Kim, J. Y. Lee, T. H. Yoon, B. J. Cho, S. O. Kim, R. S. Ruoff *et al.*, "Graphene oxide thin films for flexible nonvolatile memory applications," *Nano letters*, vol. 10, no. 11, pp. 4381–4386, 2010.

[201] T. Driscoll, H. Kim, B. Chae, B. Kim, Y. Lee, J. Marie, S. Palit, and D. Smith, "Dv m, and dn basov,"," *Memory Metamaterials," Science*, vol. 325, pp. 1518–1521, 2009.

[202] B.-z. Xu, C.-q. Gu, Z. Li, and Z.-y. Niu, "A novel structure for tunable terahertz absorber based on graphene," *Optics express*, vol. 21, no. 20, pp. 23 803–23 811, 2013.

[203] S. H. Lee, M. Choi, T.-T. Kim, S. Lee, M. Liu, X. Yin, H. K. Choi, S. S. Lee, C.-G. Choi, S.-Y. Choi *et al.*, "Switching terahertz waves with gate-controlled active graphene metamaterials," *Nature materials*, vol. 11, no. 11, pp. 936–941, 2012.

[204] N. Rouhi, S. Capdevila, D. Jain, K. Zand, Y. Y. Wang, E. Brown, L. Jofre, and P. Burke, "Terahertz graphene optics," *Nano Research*, vol. 5, pp. 667–678, 2012.

[205] B. Sensale-Rodriguez, T. Fang, R. Yan, M. M. Kelly, D. Jena, L. Liu *et al.*, "Unique prospects for graphene-based terahertz modulators," *Applied Physics Letters*, vol. 99, no. 11, 2011.

[206] H. Liu, Y. Liu, and D. Zhu, "Chemical doping of graphene," *Journal of materials chemistry*, vol. 21, no. 10, pp. 3335–3345, 2011.

[207] A. Kasry, M. A. Kuroda, G. J. Martyna, G. S. Tulevski, and A. A. Bol, "Chemical doping of large-area stacked graphene films for use as transparent, conducting electrodes," *ACS nano*, vol. 4, no. 7, pp. 3839–3844, 2010.

[208] J. Min Woo, M.-S. Kim, H. Woong Kim, and J.-H. Jang, "Graphene based salisbury screen for terahertz absorber," *Applied Physics Letters*, vol. 104, no. 8, 2014.

[209] Y. Zhang, Y. Feng, B. Zhu, J. Zhao, and T. Jiang, "Graphene based tunable metamaterial absorber and polarization modulation in terahertz frequency," *Optics express*, vol. 22, no. 19, pp. 22 743–22 752, 2014.

[210] H.-T. Chen, "Interference theory of metamaterial perfect absorbers," *Optics express*, vol. 20, no. 7, pp. 7165–7172, 2012.

[211] J. Bai, S. Zhang, F. Fan, S. Wang, X. Sun, Y. Miao, and S. Chang, "Tunable broadband thz absorber using vanadium dioxide metamaterials," *Optics Communications*, vol. 452, pp. 292–295, 2019.

[212] N. Mou, S. Sun, H. Dong, S. Dong, Q. He, L. Zhou, and L. Zhang, "Hybridization-induced broadband terahertz wave absorption with graphene metasurfaces," *Optics express*, vol. 26, no. 9, pp. 11 728–11 736, 2018.

[213] F. Gao, Z. Zhu, W. Xu, J. Zhang, C. Guo, K. Liu, X. Yuan, and S. Qin, "Broadband wave absorption in single-layered and nonstructured graphene based on far-field interaction effect," *Optics Express*, vol. 25, no. 9, pp. 9579–9586, 2017.

[214] S. H. Raad, Z. Atlasbaf, M. Shahabadi, and J. Rashed-Mohassel, "Dyadic green's function for the tensor surface conductivity boundary condition," *IEEE Transactions on Magnetics*, vol. 55, no. 11, pp. 1–7, 2019.

[215] G. W. Hanson, "Erratum:"dyadic green's functions and guided surface waves for a surface conductivity model of graphene"[j. appl. phys. 103, 064302 (2008)]," *Journal of Applied Physics*, vol. 113, no. 2, p. 029902, 2013.

[216] V. S. Yadav, B. K. Kaushik, and A. Patnaik, "Broadband thz absorber for large inclination angle te and tm waves," *IEEE Photonics Journal*, vol. 13, no. 5, pp. 1–7, 2021.

[217] V. G. Veselago, "Electrodynamics of substances with simultaneously negative values of ϵ and μ," *Usp. fiz. nauk*, vol. 92, no. 7, p. 517, 1967.

[218] Z. Jacob, L. V. Alekseyev, and E. Narimanov, "Optical hyperlens: far-field imaging beyond the diffraction limit," *Optics express*, vol. 14, no. 18, pp. 8247–8256, 2006.

[219] Z. Liu, H. Lee, Y. Xiong, C. Sun, and X. Zhang, "Far-field optical hyperlens magnifying sub-diffraction-limited objects," *science*, vol. 315, no. 5819, pp. 1686–1686, 2007.

[220] I. I. Smolyaninov, Y.-J. Hung, and C. C. Davis, "Magnifying superlens in the visible frequency range," *science*, vol. 315, no. 5819, pp. 1699–1701, 2007.

[221] J. B. Pendry, D. Schurig, and D. R. Smith, "Controlling electromagnetic fields," *science*, vol. 312, no. 5781, pp. 1780–1782, 2006.

[222] W. Cai, U. K. Chettiar, A. V. Kildishev, and V. M. Shalaev, "Optical cloaking with metamaterials," *Nature photonics*, vol. 1, no. 4, pp. 224–227, 2007.

[223] J. Pendry, "Metamaterials in the sunshine," *Nature Materials*, vol. 5, no. 8, pp. 599–600, 2006.

[224] N. Fang, H. Lee, C. Sun, and X. Zhang, "Sub-diffraction-limited optical imaging with a silver superlens," *science*, vol. 308, no. 5721, pp. 534–537, 2005.

[225] Q. Bai, C. Liu, J. Chen, C. Cheng, M. Kang, and H.-T. Wang, "Tunable slow light in semiconductor metamaterial in a broad terahertz regime," *Journal of Applied Physics*, vol. 107, no. 9, 2010.

[226] R. Singh, C. Rockstuhl, F. Lederer, and W. Zhang, "Coupling between a dark and a bright eigenmode in a terahertz metamaterial," *Physical Review B*, vol. 79, no. 8, p. 085111, 2009.

[227] S.-Y. Chiam, R. Singh, C. Rockstuhl, F. Lederer, W. Zhang, and A. A. Bettiol, "Analogue of electromagnetically induced transparency in a terahertz metamaterial," *Physical Review B*, vol. 80, no. 15, p. 153103, 2009.

[228] M. Wuttig and N. Yamada, "Phase-change materials for rewriteable data storage," *Nature materials*, vol. 6, no. 11, pp. 824–832, 2007.

[229] H. Kind, H. Yan, B. Messer, M. Law, and P. Yang, "Nanowire ultraviolet photodetectors and optical switches," *Advanced materials*, vol. 14, no. 2, pp. 158–160, 2002.

[230] W. M. Zhu, A. Q. Liu, X. M. Zhang, D. P. Tsai, T. Bourouina, J. H. Teng, X. H. Zhang, H. C. Guo, H. Tanoto, T. Mei *et al.*, "Switchable magnetic metamaterials using micromachining processes," *Advanced materials*, vol. 23, no. 15, pp. 1792–1796, 2011.

[231] J. Valentine, S. Zhang, T. Zentgraf, E. Ulin-Avila, D. A. Genov, G. Bartal, and X. Zhang, "Three-dimensional optical metamaterial with a negative refractive index," *nature*, vol. 455, no. 7211, pp. 376–379, 2008.

[232] Z. Jakšić, S. Vuković, J. Matovic, and D. Tanasković, "Negative refractive index metasurfaces for enhanced biosensing," *Materials*, vol. 4, no. 1, pp. 1–36, 2010.

[233] A. Ishimaru, S. Jaruwatanadilok, and Y. Kuga, "Generalized surface plasmon resonance sensors using metamaterials and negative index materials," *Progress In Electromagnetics Research*, vol. 51, pp. 139–152, 2005.

[234] S. He, Y. Jin, Z. Ruan, and J. Kuang, "On subwavelength and open resonators involving metamaterials of negative refraction index," *New Journal of Physics*, vol. 7, no. 1, p. 210, 2005.

[235] A. Alù and N. Engheta, "Dielectric sensing in ϵ-near-zero narrow waveguide channels," *Physical Review B*, vol. 78, no. 4, p. 045102, 2008.

[236] D. Shreiber, M. Gupta, and R. Cravey, "Comparative study of 1-d and 2-d metamaterial lens for microwave nondestructive evaluation of dielectric materials," *Sensors and Actuators A: Physical*, vol. 165, no. 2, pp. 256–260, 2011.

[237] N. I. Zheludev, "The road ahead for metamaterials," *Science*, vol. 328, no. 5978, pp. 582–583, 2010.

[238] M. Huang, J. Yang, and A. Petrin, "Microwave sensor using metamaterials," *Wave Propagation*, vol. 13, p. 36, 2011.

[239] A. V. Zayats and S. Maier, *Active plasmonics and tuneable plasmonic metamaterials*. John Wiley & Sons, 2013.

[240] W. Xu, L. Xie, and Y. Ying, "Mechanisms and applications of terahertz metamaterial sensing: a review," *Nanoscale*, vol. 9, no. 37, pp. 13 864–13 878, 2017.

[241] W. Xu, L. Xie, J. Zhu, W. Wang, Z. Ye, Y. Ma, C.-Y. Tsai, S. Chen, and Y. Ying, "Terahertz sensing of chlorpyrifos-methyl using metamaterials," *Food chemistry*, vol. 218, pp. 330–334, 2017.

[242] L. Cong, S. Tan, R. Yahiaoui, F. Yan, W. Zhang, and R. Singh, "Experimental demonstration of ultrasensitive sensing with terahertz metamaterial absorbers: A comparison with the metasurfaces," *Applied Physics Letters*, vol. 106, no. 3, 2015.

[243] R. Yahiaoui, S. Tan, L. Cong, R. Singh, F. Yan, and W. Zhang, "Multispectral terahertz sensing with highly flexible ultrathin metamaterial absorber," *Journal of Applied Physics*, vol. 118, no. 8, 2015.

[244] B.-X. Wang, G.-Z. Wang, and T. Sang, "Simple design of novel triple-band terahertz metamaterial absorber for sensing application," *Journal of Physics D: Applied Physics*, vol. 49, no. 16, p. 165307, 2016.

[245] F. J. Garcia-Vidal, L. Martin-Moreno, T. Ebbesen, and L. Kuipers, "Light passing through subwavelength apertures," *Reviews of Modern Physics*, vol. 82, no. 1, p. 729, 2010.

[246] S. Yoshida, K. Suizu, E. Kato, Y. Nakagomi, Y. Ogawa, and K. Kawase, "A high-sensitivity terahertz sensing method using a metallic mesh with unique transmission properties," *Journal of Molecular Spectroscopy*, vol. 256, no. 1, pp. 146–151, 2009.

[247] F. Miyamaru, S. Hayashi, C. Otani, K. Kawase, Y. Ogawa, H. Yoshida, and E. Kato, "Terahertz surface-wave resonant sensor with a metal hole array," *Optics letters*, vol. 31, no. 8, pp. 1118–1120, 2006.

[248] T. Kondo, S. Kamba, K. Takigawa, T. Suzuki, Y. Ogawa, and N. Kondo, "Highly sensitive metal mesh sensors," *Procedia Engineering*, vol. 25, pp. 916–919, 2011.

[249] H. Seto, S. Kamba, T. Kondo, M. Hasegawa, S. Nashima, Y. Ehara, Y. Ogawa, Y. Hoshino, and Y. Miura, "Metal mesh device sensor immobilized with a trimethoxysilane-containing glycopolymer for label-free detection of proteins and bacteria," *ACS Applied Materials & Interfaces*, vol. 6, no. 15, pp. 13 234–13 241, 2014.

[250] H. Seto, C. Yamashita, S. Kamba, T. Kondo, M. Hasegawa, M. Matsuno, Y. Ogawa, Y. Hoshino, and Y. Miura, "Biotinylation of silicon and nickel surfaces and detection of streptavidin as biosensor," *Langmuir*, vol. 29, no. 30, pp. 9457–9463, 2013.

[251] J. F. O'Hara, R. Singh, I. Brener, E. Smirnova, J. Han, A. J. Taylor, and W. Zhang, "Thin-film sensing with planar terahertz metamaterials: sensitivity and limitations," *Optics Express*, vol. 16, no. 3, pp. 1786–1795, 2008.

[252] C. Debus and P. H. Bolivar, "Frequency selective surfaces for high sensitivity terahertz sensing," *Applied Physics Letters*, vol. 91, no. 18, 2007.

[253] C. Ding, L. Jiang, L. Wu, R. Gao, D. Xu, G. Zhang, and J. Yao, "Dual-band ultrasensitive thz sensing utilizing high quality fano and quadrupole resonances in metamaterials," *Optics Communications*, vol. 350, pp. 103–107, 2015.

[254] R. Singh, W. Cao, I. Al-Naib, L. Cong, W. Withayachumnankul, and W. Zhang, "Ultrasensitive terahertz sensing with high-q fano resonances in metasurfaces," *Applied Physics Letters*, vol. 105, no. 17, 2014.

[255] S. Wang, L. Xia, H. Mao, X. Jiang, S. Yan, H. Wang, D. Wei, H.-L. Cui, and C. Du, "Terahertz biosensing based on a polarization-insensitive metamaterial," *IEEE Photonics Technology Letters*, vol. 28, no. 9, pp. 986–989, 2016.

[256] F. Miyamaru, Y. Sasagawa, and M. W. Takeda, "Effect of dielectric thin films on reflection properties of metal hole arrays," *Applied Physics Letters*, vol. 96, no. 2, 2010.

[257] R. Yahiaoui, A. C. Strikwerda, and P. U. Jepsen, "Terahertz plasmonic structure with enhanced sensing capabilities," *IEEE Sensors Journal*, vol. 16, no. 8, pp. 2484–2488, 2016.

[258] M. Tanaka, F. Miyamaru, M. Hangyo, T. Tanaka, M. Akazawa, and E. Sano, "Effect of a thin dielectric layer on terahertz transmission characteristics for metal hole arrays," *Optics letters*, vol. 30, no. 10, pp. 1210–1212, 2005.

[259] S. Yoshida, E. Kato, K. Suizu, Y. Nakagomi, Y. Ogawa, and K. Kawase, "Terahertz sensing of thin poly (ethylene terephthalate) film thickness using a metallic mesh," *Applied physics express*, vol. 2, no. 1, p. 012301, 2009.

[260] T. Suzuki, T. Kondo, Y. Ogawa, S. Kamba, and N. Kondo, "Detection of sio_2 thin layer by using a metallic mesh sensor," *IEEE Sensors Journal*, vol. 13, no. 12, pp. 4972–4976, 2013.

[261] B. Reinhard, K. M. Schmitt, V. Wollrab, J. Neu, R. Beigang, and M. Rahm, "Metamaterial near-field sensor for deep-subwavelength thickness measurements and sensitive refractometry in the terahertz frequency range," *Applied Physics Letters*, vol. 100, no. 22, p. 221101, 05 2012. [Online]. Available: https://doi.org/10.1063/1.4722801

[262] W. Withayachumnankul, H. Lin, K. Serita, C. M. Shah, S. Sriram, M. Bhaskaran, M. Tonouchi, C. Fumeaux, and D. Abbott, "Sub-diffraction thin-film sensing with planar terahertz metamaterials," *Opt. Express*, vol. 20, no. 3, pp. 3345–3352, Jan 2012. [Online]. Available: https://opg.optica.org/oe/abstract.cfm?URI=oe-20-3-3345

[263] H.-R. Park, X. Chen, N.-C. Nguyen, J. Peraire, and S.-H. Oh, "Nanogap-enhanced terahertz sensing of 1 nm thick (λ/106) dielectric films," *Acs Photonics*, vol. 2, no. 3, pp. 417–424, 2015.

[264] B. You, C.-C. Peng, J.-S. Jhang, H.-H. Chen, C.-P. Yu, W.-C. Lai, T.-A. Liu, J.-L. Peng, and J.-Y. Lu, "Terahertz plasmonic waveguide based on metal rod arrays for nanofilm sensing," *Optics Express*, vol. 22, no. 9, pp. 11 340–11 350, 2014.

[265] H. Tao, L. R. Chieffo, M. A. Brenckle, S. M. Siebert, M. Liu, A. C. Strikwerda, K. Fan, D. L. Kaplan, X. Zhang, R. D. Averitt *et al.*, "Metamaterials on paper as a sensing platform," *Advanced Materials*, vol. 23, no. 28, pp. 3197–3201, 2011.

[266] H.-R. Park, K. J. Ahn, S. Han, Y.-M. Bahk, N. Park, and D.-S. Kim, "Colossal absorption of molecules inside single terahertz nanoantennas," *Nano letters*, vol. 13, no. 4, pp. 1782–1786, 2013.

[267] D.-K. Lee, J.-H. Kang, J.-S. Lee, H.-S. Kim, C. Kim, J. Hun Kim, T. Lee, J.-H. Son, Q.-H. Park, and M. Seo, "Highly sensitive and selective sugar detection by terahertz nano-antennas," *Scientific reports*, vol. 5, no. 1, p. 15459, 2015.

[268] H.-M. Lam, J. Remais, M.-C. Fung, L. Xu, and S. S.-M. Sun, "Food supply and food safety issues in china," *The Lancet*, vol. 381, no. 9882, pp. 2044–2053, 2013.

[269] C. R. Kagan, "At the nexus of food security and safety: opportunities for nanoscience and nanotechnology," pp. 2985–2986, 2016.

[270] Y.-Z. Feng and D.-W. Sun, "Application of hyperspectral imaging in food safety inspection and control: a review," *Critical reviews in food science and nutrition*, vol. 52, no. 11, pp. 1039–1058, 2012.

[271] L. Xie, W. Gao, J. Shu, Y. Ying, and J. Kono, "Extraordinary sensitivity enhancement by metasurfaces in terahertz detection of antibiotics," *Scientific reports*, vol. 5, no. 1, p. 8671, 2015.

[272] J. Qin, L. Xie, and Y. Ying, "A high-sensitivity terahertz spectroscopy technology for tetracycline hydrochloride detection using metamaterials," *Food Chemistry*, vol. 211, pp. 300–305, 2016.

[273] S.-Y. Chiam, R. Singh, J. Gu, J. Han, W. Zhang, and A. A. Bettiol, "Increased frequency shifts in high aspect ratio terahertz split ring resonators," *Applied Physics Letters*, vol. 94, no. 6, 2009.

[274] S.-Y. Chiam, R. Singh, W. Zhang, and A. A. Bettiol, "Controlling metamaterial resonances via dielectric and aspect ratio effects," *Applied Physics Letters*, vol. 97, no. 19, 2010.

[275] M. Gupta, Y. K. Srivastava, M. Manjappa, and R. Singh, "Sensing with toroidal metamaterial," *Applied Physics Letters*, vol. 110, no. 12, 2017.

[276] G. Dayal, X. Y. Chin, C. Soci, and R. Singh, "High-q plasmonic fano resonance for multiband surface-enhanced infrared absorption of molecular vibrational sensing," *Advanced Optical Materials*, vol. 5, no. 2, p. 1600559, 2017.

[277] M. Theuer, R. Beigang, and D. Grischkowsky, "Highly sensitive terahertz measurement of layer thickness using a two-cylinder waveguide sensor," *Applied Physics Letters*, vol. 97, no. 7, 2010.

[278] B. You, C.-C. Peng, J.-S. Jhang, H.-H. Chen, C.-P. Yu, W.-C. Lai, T.-A. Liu, J.-L. Peng, and J.-Y. Lu, "Terahertz plasmonic waveguide based on metal rod arrays for nanofilm sensing," *Optics Express*, vol. 22, no. 9, pp. 11 340–11 350, 2014.

[279] S.-Z. A. Lo, G. Kumar, T. E. Murphy, and E. J. Heilweil, "Application of nanoporous silicon substrates for terahertz spectroscopy," *Optical Materials Express*, vol. 3, no. 1, pp. 114–125, 2013.

[280] W. Xu, L. Xie, J. Zhu, X. Xu, Z. Ye, C. Wang, Y. Ma, and Y. Ying, "Gold nanoparticle-based terahertz metamaterial sensors: mechanisms and applications," *Acs Photonics*, vol. 3, no. 12, pp. 2308–2314, 2016.

[281] M. R. Islam, M. T. Islam, B. Bais, S. H. Almalki, H. Alsaif, and M. S. Islam, "Metamaterial sensor based on rectangular enclosed adjacent triple circle split ring resonator with good quality factor for microwave sensing application," *Scientific Reports*, vol. 12, no. 1, p. 6792, 2022.

[282] P. A. George, W. Hui, F. Rana, B. G. Hawkins, A. E. Smith, and B. J. Kirby, "Microfluidic devices for terahertz spectroscopy of biomolecules," *Optics Express*, vol. 16, no. 3, pp. 1577–1582, 2008.

[283] M. Islam, S. J. M. Rao, G. Kumar, B. P. Pal, and D. Roy Chowdhury, "Role of resonance modes on terahertz metamaterials based thin film sensors," *Scientific reports*, vol. 7, no. 1, p. 7355, 2017.

[284] X. Yan, L.-J. Liang, X. Ding, and J.-Q. Yao, "Solid analyte and aqueous solutions sensing based on a flexible terahertz dual-band metamaterial absorber," *Optical Engineering*, vol. 56, no. 2, pp. 027 104–027 104, 2017.

[285] Y. Zhang, P. Lin, and Y.-S. Lin, "Tunable split-disk metamaterial absorber for sensing application," *Nanomaterials*, vol. 11, no. 3, p. 598, 2021.

[286] A. Mohanty, O. P. Acharya, B. Appasani, S. Mohapatra, and M. S. Khan, "Design of a novel terahertz metamaterial absorber for sensing applications," *IEEE Sensors Journal*, vol. 21, no. 20, pp. 22 688–22 694, 2021.

[287] J. Bai, W. Shen, S. Wang, M. Ge, T. Chen, P. Shen, and S. Chang, "An ultra-thin multiband terahertz metamaterial absorber and sensing applications," *Optical and Quantum Electronics*, vol. 53, no. 9, p. 506, 2021.

[288] S. Banerjee, U. Nath, A. V. Jha, S. Pahadsingh, B. Appasani, N. Bizon, A. Srinivasulu *et al.*, "A terahertz metamaterial absorber based refractive index sensor with high quality factor," in *2021 13th International Conference on Electronics, Computers and Artificial Intelligence (ECAI)*. IEEE, 2021, pp. 1–4.

[289] G. H. Sanders and A. Manz, "Chip-based microsystems for genomic and proteomic analysis," *TrAC Trends in Analytical Chemistry*, vol. 19, no. 6, pp. 364–378, 2000.

[290] S. Solinas-Toldo, S. Lampel, S. Stilgenbauer, J. Nickolenko, A. Benner, H. Döhner, T. Cremer, and P. Lichter, "Matrix-based comparative genomic hybridization: biochips to screen for genomic imbalances," *Genes, chromosomes and cancer*, vol. 20, no. 4, pp. 399–407, 1997.

[291] R. Liu, A. Degiron, J. J. Mock, and D. R. Smith, "Negative index material composed of electric and magnetic resonators," *Applied Physics Letters*, vol. 90, no. 26, 2007.

[292] F. Martin, F. Falcone, J. Bonache, R. Marqués, and M. Sorolla, "Miniaturized coplanar waveguide stop band filters based on multiple tuned split ring resonators," *IEEE microwave and wireless components letters*, vol. 13, no. 12, pp. 511–513, 2003.

[293] J. Garcia-Garcia, F. Martín, F. Falcone, J. Bonache, J. D. Baena, I. Gil, E. Amat, T. Lopetegi, M. A. Laso, J. A. M. Iturmendi *et al.*, "Microwave filters with improved stopband based on sub-wavelength resonators," *IEEE Transactions on Microwave theory and techniques*, vol. 53, no. 6, pp. 1997–2006, 2005.

[294] J. Bonache, I. Gil, J. Garcia-Garcia, and F. Martin, "Novel microstrip bandpass filters based on complementary split-ring resonators," *IEEE Transactions on Microwave Theory and Techniques*, vol. 54, no. 1, pp. 265–271, 2006.

[295] I. Bulu, H. Caglayan, K. Aydin, and E. Ozbay, "Compact size highly directive antennas based on the srr metamaterial medium," *New Journal of Physics*, vol. 7, no. 1, p. 223, 2005.

[296] B. Li, P.-Y. Zhu, L. Liang, and C.-H. Liang, "Study on high gain waveguide array antenna with srr structure," *Journal of Electromagnetic Waves and Applications*, vol. 21, no. 5, pp. 615–627, 2007.

[297] L.-W. Li, Y.-N. Li, T. S. Yeo, J. R. Mosig, and O. J. Martin, "A broadband and high-gain metamaterial microstrip antenna," *Applied Physics Letters*, vol. 96, no. 16, 2010.

[298] H.-J. Lee and J.-G. Yook, "Biosensing using split-ring resonators at microwave regime," *Applied Physics Letters*, vol. 92, no. 25, 2008.

[299] H.-J. Lee, H.-S. Lee, K.-H. Yoo, and J.-G. Yook, "Dna sensing using split-ring resonator alone at microwave regime," *Journal of Applied Physics*, vol. 108, no. 1, 2010.

[300] S. P. Mickan, A. Menikh, H. Liu, C. A. Mannella, R. MacColl, D. Abbott, J. Munch, and X. Zhang, "Label-free bioaffinity detection using terahertz technology," *Physics in Medicine & Biology*, vol. 47, no. 21, p. 3789, 2002.

[301] B. Fischer, M. Hoffmann, H. Helm, G. Modjesch, and P. U. Jepsen, "Chemical recognition in terahertz time-domain spectroscopy and imaging," *Semiconductor Science and Technology*, vol. 20, no. 7, p. S246, 2005.

[302] J. F. Federici, B. Schulkin, F. Huang, D. Gary, R. Barat, F. Oliveira, and D. Zimdars, "Thz imaging and sensing for security applications—explosives, weapons and drugs," *Semiconductor science and technology*, vol. 20, no. 7, p. S266, 2005.

[303] H. Yoshida, Y. Ogawa, Y. Kawai, S. Hayashi, A. Hayashi, C. Otani, E. Kato, F. Miyamaru, and K. Kawase, "Terahertz sensing method for protein detection using a thin metallic mesh," *Applied physics letters*, vol. 91, no. 25, 2007.

[304] F. Miyamaru, S. Hayashi, C. Otani, K. Kawase, Y. Ogawa, H. Yoshida, and E. Kato, "Terahertz surface-wave resonant sensor with a metal hole array," *Optics letters*, vol. 31, no. 8, pp. 1118–1120, 2006.

[305] C. Debus and P. H. Bolivar, "Frequency selective surfaces for high sensitivity terahertz sensing," *Applied Physics Letters*, vol. 91, no. 18, 2007.

[306] H. Tao, L. R. Chieffo, M. A. Brenckle, S. M. Siebert, M. Liu, A. C. Strikwerda, K. Fan, D. L. Kaplan, X. Zhang, R. D. Averitt *et al.*, "Metamaterials on paper as a sensing platform," *Advanced Materials*, vol. 23, no. 28, pp. 3197–3201, 2011.

[307] X. Shen, Y. Yang, Y. Zang, J. Gu, J. Han, W. Zhang, and T. Jun Cui, "Triple-band terahertz metamaterial absorber: Design, experiment, and physical interpretation," *Applied Physics Letters*, vol. 101, no. 15, 2012.

[308] B.-X. Wang, X. Zhai, G.-Z. Wang, W.-Q. Huang, and L.-L. Wang, "A novel dual-band terahertz metamaterial absorber for a sensor application," *Journal of Applied Physics*, vol. 117, no. 1, 2015.

[309] A. Forouzmand, H. M. Bernety, and A. B. Yakovlev, "Graphene-loaded wire medium for tunable broadband subwavelength imaging," *Physical Review B*, vol. 92, no. 8, p. 085402, 2015.

[310] W. Su, Z. Geng, J. Qi, and H. Wu, "Multi-fano resonances in graphene coated all-dielectric metasurface for refractive index sensing with high figure of merits," *IEEE Journal of Selected Topics in Quantum Electronics*, vol. 27, no. 1, pp. 1–6, 2020.

[311] Y.-L. Liao and Y. Zhao, "Ultra-narrowband dielectric metamaterial absorber with ultra-sparse nanowire grids for sensing applications," *Scientific reports*, vol. 10, no. 1, p. 1480, 2020.

[312] X. Liu, K. Fan, I. V. Shadrivov, and W. J. Padilla, "Experimental realization of a terahertz all-dielectric metasurface absorber," *Optics express*, vol. 25, no. 1, pp. 191–201, 2017.

[313] F. Lan, F. Luo, P. Mazumder, Z. Yang, L. Meng, Z. Bao, J. Zhou, Y. Zhang, S. Liang, Z. Shi *et al.*, "Dual-band refractometric terahertz biosensing with

intense wave-matter-overlap microfluidic channel," *Biomedical Optics Express*, vol. 10, no. 8, pp. 3789–3799, 2019.

[314] A. S. Saadeldin, M. F. O. Hameed, E. M. Elkaramany, and S. S. Obayya, "Highly sensitive terahertz metamaterial sensor," *IEEE Sensors Journal*, vol. 19, no. 18, pp. 7993–7999, 2019.

[315] P. Upender and A. Kumar, "Ultrathin, ultra narrow band dmma for biosensing applications," *IEEE Transactions on NanoBioscience*, 2022.

[316] W. Zhang, J.-Y. Li, and J. Xie, "High sensitivity refractive index sensor based on metamaterial absorber," *Progress In Electromagnetics Research M*, vol. 71, pp. 107–115, 2018.

[317] B.-X. Wang, C. Xu, H. Zhou, and G. Duan, "Realization of broadband terahertz metamaterial absorber using an anti-symmetric resonator consisting of two mutually perpendicular metallic strips," *Apl Materials*, vol. 10, no. 5, 2022.

[318] B.-X. Wang, G. Duan, C. Xu, J. Jiang, W. Xu, and F. Pi, "Design of multiple-frequency-band terahertz metamaterial absorbers with adjustable absorption peaks using toothed resonator," *Materials & Design*, vol. 225, p. 111586, 2023.

[319] B.-X. Wang, W. Xu, Y. Wu, Z. Yang, S. Lai, and L. Lu, "Realization of a multi-band terahertz metamaterial absorber using two identical split rings having opposite opening directions connected by a rectangular patch," *Nanoscale Advances*, vol. 4, no. 5, pp. 1359–1367, 2022.

[320] B.-X. Wang, Y. He, P. Lou, and H. Zhu, "Multi-band terahertz superabsorbers based on perforated square-patch metamaterials," *Nanoscale Advances*, vol. 3, no. 2, pp. 455–462, 2021.

[321] B.-X. Wang, C. Xu, G. Duan, W. Xu, and F. Pi, "Review of broadband metamaterial absorbers: from principles, design strategies, and tunable properties to functional applications," *Advanced Functional Materials*, vol. 33, no. 14, p. 2213818, 2023.

[322] M. S. Khan, G. Varshney, and P. Giri, "Altering the multimodal resonance in ultrathin silicon ring for tunable thz biosensing," *IEEE Transactions on NanoBioscience*, vol. 20, no. 4, pp. 488–496, 2021.